



저작자표시-비영리-변경금지 2.0 대한민국

이용자는 아래의 조건을 따르는 경우에 한하여 자유롭게

- 이 저작물을 복제, 배포, 전송, 전시, 공연 및 방송할 수 있습니다.

다음과 같은 조건을 따라야 합니다:



저작자표시. 귀하는 원저작자를 표시하여야 합니다.



비영리. 귀하는 이 저작물을 영리 목적으로 이용할 수 없습니다.



변경금지. 귀하는 이 저작물을 개작, 변형 또는 가공할 수 없습니다.

- 귀하는, 이 저작물의 재이용이나 배포의 경우, 이 저작물에 적용된 이용허락조건을 명확하게 나타내어야 합니다.
- 저작권자로부터 별도의 허가를 받으면 이러한 조건들은 적용되지 않습니다.

저작권법에 따른 이용자의 권리는 위의 내용에 의하여 영향을 받지 않습니다.

이것은 [이용허락규약\(Legal Code\)](#)을 이해하기 쉽게 요약한 것입니다.

[Disclaimer](#)

공학박사학위논문

**Assessment of rock cutting efficiency of pick cutters
for the optimal design of a mechanical excavator**

기계굴착장비의 최적 설계를 위한
픽 커터의 암석 절삭효율 평가

2017년 8월

서울대학교 대학원
에너지시스템공학부
정 호 영

Abstract

Assessment of rock cutting efficiency of pick cutters for the optimal design of a mechanical excavator

Hoyoung Jeong

Department of Energy Systems Engineering

The Graduate School

Seoul National University

The application of mechanical excavation method has been used in many civil and mining projects, and its demand has been rapidly increased due to the numerous advantages regarding safety, stability, high advance rate, less environmental impact and construction practice compared with the drill and blasting method. Especially, the mechanical excavation is sometimes essential for the urban, subsea tunneling and subsea trenching.

There are many types of mechanical excavators including TBM, roadheader, trencher, and auger, which use pick cutters. Because it is difficult to change the design of the mechanical excavators, it is important to design the machine considering the characteristics of the given geological conditions and to determine the operational conditions in advance. The

design parameters of the mechanical excavators are mainly cutter arrangement, thrust, torque, and rotational speed of the cutterhead. These design parameters should be carefully estimated with consideration of the effect of the cutting conditions (i.e., penetration depth, cut spacing, and cutting angle) on the cutting force, cutting efficiency, and mechanical stability of a machine.

In this study, a small linear cutting test equipment was manufactured, and a series of tests were performed under various cutting conditions to investigate the effect of various cutting parameters on the cutting performance and the cutting efficiency. This study quantitatively analyzed the relationship between cutting conditions (penetration depth, cut spacing, skew angle and attack angle) and various design parameters of the pick cutter. Then the optimal cutting conditions considering both the cutting efficiency and the stability of the mechanical excavators were suggested.

The size and distribution of the rock chip generated during the rock cutting process were quantitatively analyzed using sieve testing and image processing techniques. The size distribution of the rock chips was highly correlated with the rock cutting efficiency. The larger the chip size and the smaller the ratio of rock powder, the higher the cutting efficiency was.

The rock cutting process by a pick cutter was numerically simulated using AUTODYN-3D, and the cutting efficiency was evaluated using the developed numerical model. To overcome the limitations of existing grid based FEM in rock cutting simulation, the applicability of SPH (Smooth Particle Hydrodynamics) technique was evaluated, and the numerical model was proposed to simulate the rock cutting process by pick cutters. The SPH

method could successfully simulate the rock cutting process that matches with the LCM test result. Therefore, the applicability of the SPH method was validated.

The design process of a trenching machine installed with pick cutters was proposed. The operation condition and cutter arrangement were optimally determined based on the results of the linear cutting test and the numerical analysis obtained in this study. As a result of this study, it is expected that the experimental results, numerical model and design process can be used for the design of trenching cutter and the other mechanical excavators using pick cutters

Keywords: Pick cutter, small scaled LCM, cutting efficiency, design parameters, mechanical excavator, SPH, size distribution

Student ID: 2010-31017

Contents

1. Introduction	1
1.1 Background	1
1.2 Motivation	10
1.3 Objectives and the structure of the dissertation	12
2. Literature review	14
2.1 Rock cutting mechanism and its parameters	14
2.2 Theoretical studies	21
2.3 Experimental studies	23
2.4 Numerical studies	31
2.5 Chip size distribution	40
3. Methodology	44
3.1 Scaled linear cutting machine system	44
3.2 Experiment design	47
3.3 Experimental set-up	49
3.4 Measurement of chip size distribution	57
4. Results of LCM test	64
4.1 Linyi-sandstone	64
4.2 Concrete	75
4.3 Effect of skew angle	86
4.4 Effect of attack angle	112

4.5 Relieved versus Unrelieved cut	126
5. Chip size analysis	128
5.1 Chip size distribution	128
5.2 Size distribution parameters	132
6. Numerical modelling of rock cutting	151
6.1 Limitation of FEM in rock cutting simulation	151
6.2 Smooth particle hydrodynamics	155
6.3 Numerical Model	162
6.4 Numerical simulation	176
7. Discussion	212
7.1 Analysis of the LCM result	212
7.2 Numerical simulation	221
7.3 Design case of trench cutter	225
8. Conclusions	239
References	244
Abstract (Korean)	253

List of Figures

Figure 1.1 Typical types of TBMs (Herrenknecht, 2017)	2
Figure 1.2 Typical roadheaders (Sandvik, 2017; Shijiazhuang zhogmei, 2017)	3
Figure 1.3 Typical trenching cutters (Vermeer, 2017)	3
Figure 1.4 Different types of pick cutters (Copur et al., 2012)	4
Figure 1.5 The diagram of typical linear cutting machine system (after Jeong et al., 2016)	7
Figure 2.1 The rock cutting patterns by pick cutter according to the different cut spacings (modified from Balci and Bilgin, 2007) ·	15
Figure 2.2 Three orthogonal forces acting on a pick cutter	16
Figure 2.3 concept of the optimum cutting conditions (After Cho et al., 2010)	17
Figure 2.4 Definition of the parameters between rock and pick cutter (modified from Bilgin et al., 2014)	20
Figure 2.5 The results from small and full scale LCM test: (a) relationship between specific energy obtained from two LCM tests, (b) the relationship between the uniaxial compressive strength and specific energy (Bilgin et al., 2007)	25
Figure 2.6 The effect of saturation of the rock on the cutting performance and size distribution of rock chip (a) the relationship between the CI and absolute constant size and (b) the relationship between the specific energy and CI (Barkar and Gertsch, 2013)	27

Figure 2.7 The concept of the rotary type of rock cutting tester (Liu et al., 2009)	29
Figure 2.8 The numerical simulation of rock fragmentation by TBM disc cutter using AUTODYN (Cho et al., 2010)	32
Figure 2.9 The numerical simulation of rock cutting by chisel type pick cutter using LS-DYNA (Menezes et al., 2014)	33
Figure 2.10 The numerical simulation of rock cutting process by a TBM disc cutter using ABAQUS (Geng et al., 2016)	33
Figure 2.11 The partial modeling of rocks for rock crushing simulation in finite element method (Geng et al., 2017)	35
Figure 2.12 Rock cutting simulation of conical pick cutter using discrete element method, DEMPack (Rojek et al., 2011)	36
Figure 2.13 Rock cutting simulation of conical pick cutter using PFC-3D (Su and Akcin, 2011)	37
Figure 2.14 Rock cutting simulation of TBM disc cutter using SPH code (Jeong et al., 2013)	38
Figure 2.15 Rock cutting simulation of pick cutter in saturated rock using DEM/SPH coupled code (Helmons et al., 2016)	39
Figure 2.16 Rock cutting simulation of the disc cutter using FEM/SPH coupled code (Xiao et al., 2017)	40
Figure 2.17 Typical specific energy archived by different mechanical excavation machines (Ozdemir, 1995)	42
Figure 3.1 The small scaled linear cutting machine system in this study	45
Figure 3.2 The load-cell to measure the three directional cutter forces	45
Figure 3.3 The control panel and data acquisition in LCM system	45

Figure 3.4 The cutter plate to set the different skew angles	46
Figure 3.5 The cutter holders to set the different attacks	46
Figure 3.6 The definition of the testing variables in LCM test	48
Figure 3.7 SEM images of Linyi sandstone at the different magnifications: (a) 100× and (b) 500× (Kim, 2017)	52
Figure 3.8 A schematic diagram and photo of pick cutter used in this study	53
Figure 3.9 A photogrammetric system for measurement of rock volume in rock cutting by different cutting tools	54
Figure 3.10 The rock specimen (a) before and (b) after preconditioning ..	55
Figure 3.11 The process of Split-desktop for size distribution analysis	61
Figure 3.12 Rock chip images before and after image processing: (a) and (b) are for $p = 5$ mm and $s/p = 1$, and (c) and (d) are for $p =$ 9 mm and $s/p = 1$	62
Figure 3.13 The direct sieving tester used in this study	63
Figure 4.1 The representative cutter forces obtained from LCM test	66
Figure 4.2 Effect of s/p ratio on the mean cutting force (Linyi sandstone, α $= 45^\circ$ and $\theta = 0^\circ$)	67
Figure 4.3 Effect of the s/p ratio on the mean normal force (Linyi sandstone, $\alpha = 45^\circ$ and $\theta = 0^\circ$)	68
Figure 4.4 Effect of the s/p ratio on the force index (Linyi sandstone, $\alpha =$ 45° and $\theta = 0^\circ$)	69
Figure 4.5 The relationship between the peak cutter force and mean cutter force (Linyi sandstone, $\alpha = 45^\circ$ and $\theta = 0^\circ$)	70
Figure 4.6 The cutting coefficients for the mean and peak forces (Linyi	

sandstone, $\alpha = 45^\circ$ and $\theta = 0^\circ$)	71
Figure 4.7 The relationship between s/p ratio and specific energy (Linyi sandstone, $\alpha = 45^\circ$ and $\theta = 0^\circ$)	72
Figure 4.8 The relationship between penetration depth and specific energy at the optimum cutting condition (Linyi sandstone, $\alpha = 45^\circ$ and $\theta = 0^\circ$)	73
Figure 4.9 The relationship between penetration depth and specific energy at the optimum cutting condition (Linyi sandstone, $\alpha = 45^\circ$ and $\theta = 0^\circ$ at $p = 5$ mm)	74
Figure 4.10 The concrete specimens used in this study: (a) concrete blocks and (b) cut surface	75
Figure 4.11 The effect of the penetration depth and the cut spacing on the mean normal force (Concrete, $\alpha = 45^\circ$ and $\theta = 0^\circ$)	77
Figure 4.12 The effect of the penetration depth and the cut spacing on the mean normal force (Concrete, $\alpha = 45^\circ$ and $\theta = 0^\circ$)	78
Figure 4.13 Effect of the cut spacing on the force index (Concrete, $\alpha = 45^\circ$ and $\theta = 0^\circ$)	79
Figure 4.14 The relationship between the peak cutter force and mean cutter force (Linyi sandstone, $\alpha = 45^\circ$ and $\theta = 0^\circ$)	80
Figure 4.15 The relationship between the cutting force and normal force (Concrete, $\alpha = 45^\circ$ and $\theta = 0^\circ$)	82
Figure 4.16 The bending force according to the skew angle and direction of resultant force	83
Figure 4.17 The effect of cut spacing on the specific energy and optimum cut spacing at the different penetration depth (Concrete, $\alpha = 45^\circ$	

and $\theta = 0^\circ$)	84
Figure 4.18 The effect of the penetration on the specific energy at different cut spacing (Concrete, $\alpha = 45^\circ$ and $\theta = 0^\circ$)	85
Figure 4.19 The effect of the skew angle on the mean cutting force at the different penetration depths	91
Figure 4.20 The normalized mean cutting force at the different penetration depths and skew angles	92
Figure 4.21 The effect of the skew angle on the mean normal force at the different penetration depths (Linyi sandstone, $\alpha = 45^\circ$)	93
Figure 4.22 The normalized mean normal force at the different penetration depths and skew angles (Linyi sandstone, $\alpha = 45^\circ$)	94
Figure 4.23 The effect of the skew angle on the mean side force at the different penetration depths (Linyi sandstone, $\alpha = 45^\circ$)	95
Figure 4.24 The normalized mean side force at the different penetration depths and the skew angles (Linyi sandstone, $\alpha = 45^\circ$)	96
Figure 4.25 The variation of the ratio of side to cutting force according to skew angle	97
Figure 4.26 The direction of the resultant force on the cutting surface according to the skew angle	98
Figure 4.27 The bending force according to the skew angle and direction of resultant force	101
Figure 4.28 The difference between the direction of the resultant force and the cutter axis according to the skew angle	102
Figure 4.29 The cutting coefficients depending on the skew angle (Linyi sandstone, $\alpha = 45^\circ$)	103

Figure 4.30 The ratio of the peak to mean cutter forces depending on the skew angle (Linyi sandstone, $\alpha = 45^\circ$)	103
Figure 4.31 The effect of the penetration and the skew angles on the specific energy	105
Figure 4.32 The comparison of the effect of the skew angle on the side force in the Linyi sandstone and concrete	106
Figure 4.33 The specific energy according to the skew angle in different penetration depths	107
Figure 4.34 The normalized specific energy according to the skew angle in different penetration depths	109
Figure 4.35 The comparison of the effect of skew angle on the specific energy in the Linyi sandstone and concrete	111
Figure 4.36 The effect of the attack angle on the cutting force at the different cut spacings and penetration depths: (a) $p = 5$ mm and (b) $p = 7$ mm	116
Figure 4.37 The effect of the attack angle on the normal force at the different cut spacings and penetration depths: (a) $p = 5$ mm and (b) $p = 7$ mm	118
Figure 4.38 The ratio of the cutting force to the normal force at the different attack angles and penetration depths	119
Figure 4.39 The ratio of the peak to the mean of cutting and normal forces at the different attack angles	122
Figure 4.40 The relationship between the specific energy and cut spacing at different attack angles	124
Figure 4.41 The relationship between the specific energy and the attack	

angle at the different cut spacings	125
Figure 4.42 The comparison of the cutter forces in relieved cut and unrelieved cut (Linyi sandstone)	127
Figure 4.43 The comparison of the cutter forces in relieved cut and unrelieved cut (Concrete)	127
Figure 5.1 The representative rock chips in different penetration depth at optimum cut spacing	129
Figure 5.2 The relationship between the mean particle size (D_{50}) and the different particle size parameters (Linyi sandstone)	135
Figure 5.3 The effect of the cut spacing on the coarseness index (Linyi sandstone)	136
Figure 5.4 The relationship between the mean particle size and the cutter forces (Linyi sandstone)	137
Figure 5.5 The relationship between the specific energy and coarseness index (Linyi sandstone)	138
Figure 5.6 The relationships between the penetration depth, absolute size constant, uniformity index, and coarseness index (Linyi sandstone)	139
Figure 5.7 The rock particles sieved by the 20, 40 and 100 meshes of sieves	141
Figure 5.8 The distribution of the sieved rock particles according to the s/p ratio	143
Figure 5.9 The percentage of rock powder according to th penetration depth (Linyi sandstone)	144
Figure 5.10 The effect of the skew angle on the rock powder producing	

(Linyi sandstone)	148
Figure 5.11 The relationship between the proportion of rock powder and the specific energy (Linyi sandstone)	150
Figure 6.1 Kernel function for the interpolation of SPH (Century Dynamics, 2005)	157
Figure 6.2 Computational cycle for SPH code (Century Danymics, 2005)	161
Figure 6.3 The modeled pick cutter used in numerical simulation in this study	163
Figure 6.4 Description of the Drucker-Prager model with Stassi-hardening function (After Cho et al. 2010)	165
Figure 6.5 Cumulative damage as a function of effective plastic strain (After Century Dynamics, 2005)	168
Figure 6.6 The yield stress as a function of cumulative damage model (Modified from Century Dynamics, 2005)	169
Figure 6.7 Bulk and shear modulus as functions of cumulative damage model (Modified from Century Dynamics, 2005)	170
Figure 6.8 The rock cutting model used in this study	175
Figure 6.9 The fragmentation patterns in Linyi sandstone at the different cut spacing ($p = 5$ mm)	180
Figure 6.10 The fragmentation patterns in Linyi sandstone at the different cut spacing ($p = 7$ mm)	181
Figure 6.11 The fragmentation patterns in Linyi sandstone at the different cut spacing ($p = 9$ mm)	182
Figure 6.12 The fragmentation patterns in Linyi sandstone at the different cut spacing ($p = 11$ mm)	183

Figure 6.13 The fragmentation patterns in Linyi sandstone at the different cut spacing ($p = 13$ mm)	184
Figure 6.14 The fragmentation patterns in concrete at the different cut spacing ($p = 5$ mm)	185
Figure 6.15 The crack generation due to interaction of adjacent cutters	186
Figure 6.16 The interaction between the adjacent cutters in numerical simulation at the different cut spacing condition	187
Figure 6.17 The damage contour at the different height of the rock model (cutting condition : $p = 5$ mm, $s = 20$ mm)	189
Figure 6.18 The distribution of (a) maximum principal stress and (b) stress in vertical direction (cutting condition : $p = 5$ mm, $s = 20$ mm)	190
Figure 6.19 The representative cutter force obtained from the numerical simulation	192
Figure 6.20 the comparison of the cutter force between the LCM and the numerical simulation (Linyi sandstone, $p = 5$ mm)	194
Figure 6.21 the comparison of the cutter force between the LCM and the numerical simulation (Linyi sandstone, $p = 7$ mm)	196
Figure 6.22 the comparison of the cutter force between the LCM and the numerical simulation (Linyi sandstone, $p = 9$ mm)	198
Figure 6.23 the comparison of the cutter force between the LCM and the numerical simulation (Linyi sandstone, $p = 11$ mm)	200
Figure 6.24 the comparison of the cutter force between the LCM and the numerical simulation (Concrete, $p = 5$ mm)	202

Figure 6.25	The comparison of the specific energy between the LCM and the numerical simulation (Linyi sandstone, $p = 5$ mm)	203
Figure 6.26	The comparison of the specific energy between the LCM and the numerical simulation (Linyi sandstone, $p = 7$ mm)	204
Figure 6.27	The comparison of the specific energy between the LCM and the numerical simulation (Linyi sandstone, $p = 9$ mm)	205
Figure 6.28	The comparison of the specific energy between the LCM and the numerical simulation (Linyi sandstone, $p = 11$ mm)	206
Figure 6.29	The result of the optimum cut spacing at 13 mm of penetration depth in numerical simulation (Linyi sandstone)	207
Figure 6.30	The comparison of the specific energy between the LCM and the numerical simulation (Concrete, $p = 5$ mm)	208
Figure 6.31	The comparison of the effect of attack angle on the mean cutting force in the LCM and the numerical simulation	210
Figure 6.32	The comparison of the effect of attack angle on the mean normal force in the LCM and the numerical simulation	210
Figure 6.33	The comparison of the effect of attack angle on the specific energy in the LCM and the numerical simulation	211
Figure 7.1	The comparison of the mean cutter force between Linyi sandstone (L) and concrete (C)	214
Figure 7.2	The comparison of the peak cutter force between Linyi sandstone (L) and concrete (C)	215
Figure 7.3	The difference of specific energy between Linyi sandstone and concrete	216
Figure 7.5	The concept of the Lagrange-SPH coupling	224

Figure 7.6 An example of rock cutting simulation using Lagrange-SPH coupled code in AUTODYN	224
Figure 7.7 General flow chart of design for trenching cutter	225
Figure 7.8 The schematic drawing and variables of trenching cutter	226
Figure 7.9 The spread sheet program for the design of trench cutter	227
Figure 7.10 The concept of cutter spacings and cutter arrangement	228
Figure 7.11 The pick arrangement on the trenching cutter (4 sequential arrangement)	229
Figure 7.12 The schematic drawing of the designed trenching cutter	230
Figure 7.13 Torque requirement of the trench cutter according to different operational conditions	234
Figure 7.14 Power requirement of the trench cutter according to different operational conditions	234
Figure 7.15 The numerical model of the rock excavation by multiple cutters (a): side view and (b) isometric view	236
Figure 7.16 The simulation results of the rock surfaces after the cutting by the trenching cutter	238

List of Tables

Table 2.1	The definition of the design parameters of pick cutter	19
Table 2.2	The prediction models for estimation of the cutter forces	30
Table 3.1	Mechanical properties of Linyi-sandstone	50
Table 3.2	Mechanical properties of Concrete	50
Table 3.3	Mixing ratio of the concrete	51
Table 3.4	The example of the calculation of coarseness index (<i>CI</i>) for Linyi sandstone at $p = 9$ mm and $s = 18$ mm	58
Table 4.1	The testing conditions and the results for the Linyi sandstone	75
Table 4.2	The testing conditions and the results for the concrete specimen	76
Table 4.3	LCM test conditions to analyze the effect of the skew angle on the optimum cutting conditions	87
Table 4.4	The testing conditions and the results of the linear cutting test with different skew angles	88
Table 4.5	The direction of resultant force according to the skew angle ..	98
Table 4.6	The testing conditions and the results of the linear cutting test with different attack angles	113
Table 4.7	The direction of resultant force according to the attack angle ..	121
Table 5.1	The results of LCM test and chip size distribution (Linyi sandstone)	134
Table 5.2	The spearman correlation matrix of the parameters	134
Table 5.3	Soil particle size classification	140

Table 5.4	The results of the analysis for the rock powder generation (Linyi sandstone, $\alpha = 45$, $\theta = 0$)	142
Table 5.5	The results of the analysis for the rock powder generation with different skew angles	146
Table 6.1	The different erosion criteria and value used for the rock cutting simulation in previous studies	153
Table 6.2	Input parameters of tungsten carbide for modelling of pick cutter	163
Table 6.3	Input parameters and their factor levels for sensitivity analysis	170
Table 6.4	Design matrix for the full factorial design	171
Table 6.5	The results of numerical simulation for sensitivity analysis	172
Table 6.6	The Spearman correlation matrix of the input parameters and results of numerical simulation	172
Table 6.7	The Pearson correlation matrix of the input parameters and results of numerical simulation	172
Table 6.8	Input parameters of Linyi sandstone and concrete for rock model	173
Table 6.9	The cutting conditions and results of numerical simulation	177
Table 6.10	The numerical and LCM results in different attack angles	209
Table 7.1	The variables of trenching cutter used in this design	226
Table 7.2	The correction factors for calculation of the three directional cutter forces	231
Table 7.3	The preferable operation condition of the trenching cutter	233
Table 7.4	The information of cutter arrangement in the simulation	235

1. Introduction

1.1 Background

The demand and application of mechanized excavation have been steadily increasing in many civil and mining projects, and its key technologies have been rapidly grown (Jeong et al., 2014). There are many types of mechanical excavation machines according to their shapes and purposes. Among them, TBM (tunnel boring machine), road-header, long-wall shearer, and trencher are widely used in civil and mining projects.

The mechanized excavation method is preferred over drill and blast method for numerous advantages, such as safety, providing continuous and remarkably high advance rate, less environmental impact and ground disturbance.

Especially, in recent years, there has been an increasing demand for civil projects to develop the urban, subsea, and sub-river region worldwide. In mining industry, as the application of automated mining system increases, the performance and stability of the machine are important for the productivity. Therefore, the design of a machine should be optimized in consideration of the ground conditions and the working environment so as to satisfy this requirement and demand.

The TBM is a full-face tunnelling machine excavating the entire section of a tunnel at once, and all cutters are in contact with the excavation face. It is the most widely adopted machine, and it is categorized into several types based on the target ground condition (soil, rock and mixed ground),

use of the shield, face supporting method, and working mode.

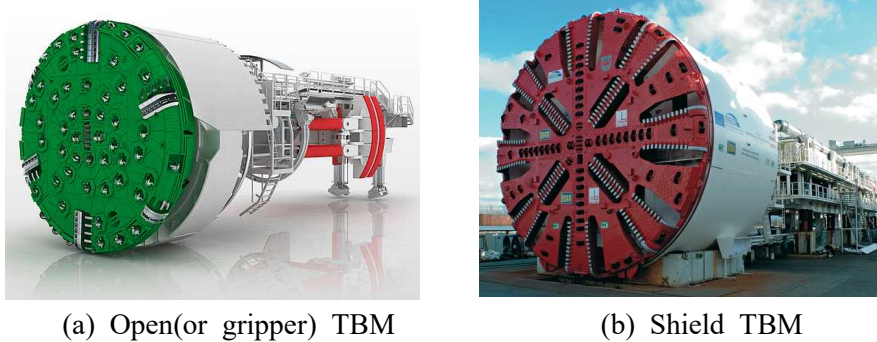


Figure 1.1 The typical types of TBMs (Herrenknecht, 2017)

On the other hand, the road-header is a partial-face machine that excavates the target face sequentially and stepwise. It is generally divided into axial and transverse types depending on the cutting-head type (Figure 1.2). As the characteristics of the partial-face machine, separate excavation of hard and soft part of a mixed face is available (Bilgin et al., 2014). The basic advantages of road-headers over the other underground excavation machines are their mobility, flexibility, and selective mining ability (Ozdemir, 1997). They also have general advantages of mechanical excavators, and it can be widely used in underground mining, surface operation, and tunnel construction.



(a) Transverse type



(b) Axial type

Figure 1.2 Typical roadheaders (Sandvik, 2017; Shijiazhuang zhongmei, 2017)

The trencher is usually used to construct a trench for pipes and cables. The demand for trenching is increasing at construction sites on not only ground but also on subbed ground. However, the related technology has been based on the simple theoretical approaches in the design of machine and prediction of cutting performance rather than that of geomechanical based theories (based on the literature survey by the author). The trencher is categorized into wheel (often called by rock wheel), drum and chain cutter types.



(a) Wheel cutter



(b) Chain cutter

Figure 1.3 Typical trenching cutters (Vermeer, 2017)

On the other hand, there are different types of rock cutting tools using mechanical excavation machine, and they are generally categorized into disc cutter and pick cutter. The main fragmentation mechanism is different for the different tools; a disc cutter breaks the rock in indenting process. The main force of disc cutter related with rock breakage is the normal force. On the other hand, the main force of a pick cutter is the cutting force (the same term with the rolling force of a disc cutter) that acts in the direction parallel to the rock surface. Thus, the main mechanism of rock breakage of a pick cutter is dragging. It is reported that pick cutters can be used for rocks with a uniaxial compressive strength up to 120 MPa. (Copur et al., 2012)

Disc cutters are mainly used in TBMs and partially used in road-headers. On the other hand, pick cutters are used in roadheaders, long-wall shearers, trenchers, and continuous miners. Pick cutters are categorized into several types depending on the shape and the direction of rotation of cutter; there are radial, scraper, chisel, and conical picks. (Figure 1.4)

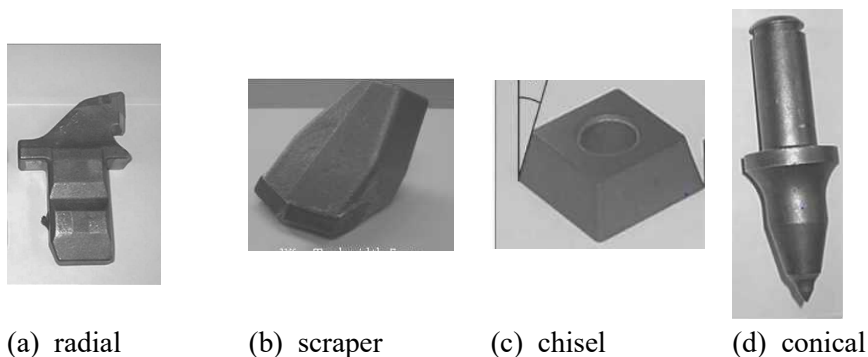


Figure 1.4 Different types of pick cutters (Copur et al., 2012)

Although the mechanical excavation machines are categorized into several types depending on the purpose of the excavation and their shapes, their design process is similar to each other. In the design stage of the machine, it is important to determine the cutter arrangement and operational parameters as well as to evaluate the performance of the machine.

There are many parameters to design a mechanized excavation machine and to determine the machine operation condition. They include cutter type, cutter dimension, cutter tip angle and shape, number of cutters, cutter (cut) spacing, penetration depth per revolution, installation angle of cutter, cutting speed, thrust, torque, and RPM.

Of the parameters, it is important to estimate the forces that act on the cutting tool (i.e., normal, cutting or rolling, and side force) when cutting a particular type of rock to determine operational parameter. The cutting forces are used to predict the penetration rate and to determine the optimum operational parameters of the machine for the given ground condition. The normal force that acts on the cutting tool determines the thrust, and the cutting (rolling) force determines the torque and power of the machine during operation, which are important factors in cutter-head design and machine operation (Jeong et al., 2016).

The cutters on the cutting head have specific spacing each other called as cutter spacing (or cut spacing). The cutters also have angles; a disc cutter has tilt angle on the gauge area, and a pick cutter has the attack angle and the skew angle. Since the excavation efficiency of a machine and its performance are influenced by the spacing and angles of these excavation tools, it is necessary to determine the optimum spacing and angles for the

given geological condition. The cut spacing is an important parameter to determine cutter arrangement and number of cutters on a cutter head.

The LCM (Linear Cutting Machine) test has been proved to be an accurate and reliable method to evaluate design parameters of a mechanical excavator because of the following advantages; a realistic range of cutting loads to be applied and no scaling effect involved during testing (Figure 1.5). Although, the full-scale LCM test is the most reliable method to determine the design parameters of the machine and has been applied to various cases of machine design (Roxborough and Philips, 1975; Snowdon and Ryley, 1982; Sanio, 1985; Uga et al., 1986; Nilsen and Ozdemir, 1993; Bilgin et al., 2005; Bilgin et al., 2006; Chang et al., 2006; Gertsch et al., 2007, Jeong et al., 2010; Cho et al., 2010; Choi et al., 2014a; Choi et al., 2014b; Park et al., 2016). Full scale LCM test usually requires full size rock specimens (1000 mm x 1000 mm x 300 mm) which are difficult to obtain (Balci and Bilgin, 2007; Cho et al., 2013). Portable linear rock cutting test (Bilgin et al., 2010) is also available to predict the cutting performance of cutting tool with rock cores or small specimens, but it is difficult to observe the interaction between adjacent cutting grooves with small specimens.

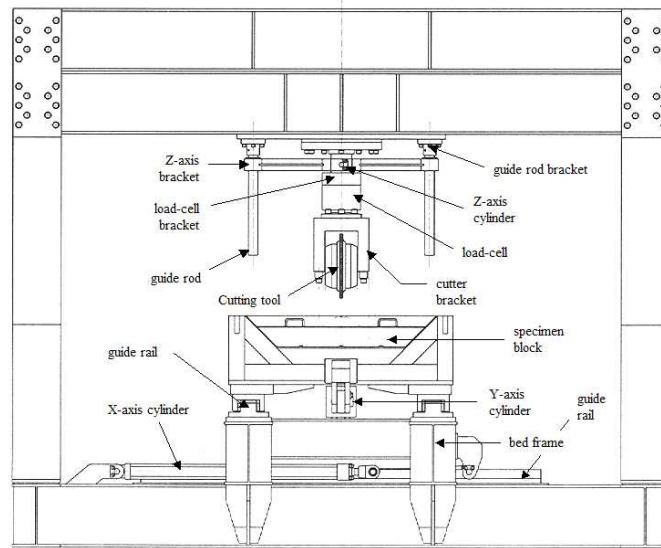


Figure 1.5 The diagram of typical linear cutting machine system
(after Jeong et al., 2016)

The previous studies related to the estimation of cutting performance have been mostly focused on effect of the basic conditions (i.e., mechanical properties of the rock, penetration depth, and cut spacing), it is insufficient to investigate the effect of the attack and skew angles, one of the important design variables of the pick cutter, on the cutting performance of a pick cutter. Recently, several studies have been carried out to investigate the effect of the angles on the cutting performance of a pick cutter (Choi et al., 2014(a); Choi et al., 2014(b); Kim et al., 2012; Park et al., 2016; Wen, 2017). However, the published results and the discussions still do not conclude the effect of the angles on the cutting performance, and the results are insufficient to be applied in the actual design of the machine, and the reliability of the results is not enough due to the lack of the experimental

database until now.

Not only various rock cutting tests (including full- and small-scale LCM test) but also analytical (theoretical), empirical and numerical approaches have been studied to understand rock fragmentation process and to estimate rock cutting performance of a pick cutter (they are explained more detailed in chapter 2). Experimental approaches, especially full-scale LCM test has advantages that the results are intuitive and reliable. However, it is difficult to simulate the various test condition in that large size of the specimen is required, and is time and cost consuming.

Therefore, analytical (theoretical), empirical, numerical and small scale cutting test approaches can be considered as the alternative to the full-scale LCM test. However, analytic/theoretical studies assume simple conditions rather than the real condition, and there are limitations to be used in the practical design, and most of the empirical models are limited because of they are not open to access in public. The numerical approach which simulates the LCM rock cutting or real excavation process) can be the best alternative way to the full-scale LCM test. Comparing with the LCM test, it has the advantage in observing the fragmentation process of the rock and also can estimate the cutting performance of a pick cutter without time and cost problem. Moreover, it has no limitation to set the cutting condition and the rock properties.

It is essential to develop the reliable numerical model, and it should be verified by the experimental results under various cutting conditions and the rock properties. Over the years, various numerical studies which use the different numerical methods have been studied to simulate the rock cutting

process. However, the numerical methods introduced until now does not accurately simulate the rock cutting process of a pick and its cutting performance, and the numerical techniques should be improved to substitute the LCM test.

On the other hand, the particle size distribution of rock chip produced by rock excavation provides useful information to estimate the cutting efficiency indirectly, and for reusing the rock chip as the construction material (like aggregates). In addition to, it is also important to determine the optimum particle size for efficient processing of mineral resources in mining engineering application. However, it is not sufficient to quantitatively analyze the size distribution of the rock chip produced by rock cutting.

Finally, in Korea, several R&D projects related to TBM design and estimating of its performance have been carried out, and the results have been applied to the practical design of TBM, and some projects are still in progress. However, in recent years, it is insufficient that the study on the road-header, trencher and continuous miner which use a pick cutter as cutting tools and are expected to be applied in various civil and mining engineering projects.

1.2 Motivation

1) Although the several studies have carried out to investigate the effect of the skew and attack angles of the pick on the rock cutting performance, however, the published results and the available discussions still do not conclude the effect of the angles of the pick on the rock cutting performance. Therefore, the results are insufficient to be applied in the actual design of the machine, and the reliability of the results is not enough. In this study, a series of linear cutting machine test was carried out to investigate the effect of the angles of the pick cutter on its cutting performance.

2) Although the full-scale LCM test is the most reliable method to determine the design parameters of the machine and has been applied to machine's design, full-scale LCM test is time- and cost- consuming in that it requires large size rock specimens (1000 mm x 1000 mm x 300 mm) which are difficult to obtain. In this study, a series of LCM test was carried out using the small-scale LCM test system which uses the smaller size of the specimen than full-scale LCM test.

3) The various studies have been studied focus on the cutter forces and corresponded specific energy of the pick cutter cut under different cutting condition. It is not sufficient to investigate the size distribution of the rock chip produced by rock cutting and to quantitatively analyze the size distribution of the rock chip produced by rock cutting. This study quantitatively analyzed the size distribution of the rock chip produced by rock cutting, and evaluated the cutting efficiency by comparing the size

distribution of the rock chip after the LCM test according to different cutting conditions.

4) Over the years, various numerical studies using the different numerical methods have been studied to simulate the rock cutting process. However, the numerical methods introduced until now does not accurately simulate the rock cutting process of a pick and its cutting performance, and the numerical techniques should be improved to substitute the LCM test. This study employed the SPH (Smooth Particle Hydrodynamics) technique to more accurately simulate the rock cutting process than finite element method (FEM).

1.3 Objectives and the structure of the dissertation

The objectives of this study are to:

- 1) Find the optimum cutting conditions under different cutting conditions, the cutter spacing, the penetration depth, the skew angle, the attack angle and different rock types.
- 2) Investigate the effect of the cutting parameters on the cutter force and the specific energy and other design parameters.
- 3) Identify the effect of the cutting conditions on the size of rock chip, its distribution and the proportion of rock powder.
- 4) Develop the numerical model to simulate the rock cutting process and rock fragmentation in the linear cutting machine test.
- 5) Suggest the design process of the trenching cutter based on the LCM tests

To achieve the objectives above, the thesis is structured as follows:

- 1) Chapter 2 is the literature review of the previous study including rock cutting mechanism, the design process of mechanical excavators, basic parameters of rock cutting and rock fragmentation.
- 2) Chapter 3 introduces the methodologies used in this study; it includes equipment and techniques for the experimental and numerical work.
- 3) Chapter 4 presents the experimental results using Scaled LCM (Linear Cutting Machine) tests. The cutter forces, specific energy, the ratios of the

cutter forces are analyzed with the cutting conditions and rock properties.

4) Chapter 5 covers the chip size distribution of rock chip produced by the rock cutting. The size distribution and rock powder generation were analyzed with the cutting conditions.

5) Chapter 6 presents the numerical simulation for the rock cutting with disc cutter and pick cutter. This study uses explicit FEM/SPH coupled model to simulate rock cutting process. The numerical results are compared with experimental results.

6) Chapter 7 is discussion part for the main results of this study. The limitations of this study, application to the trench cutter design, and the further research topic.

7) Chapter 8 summarizes the main conclusion in this study.

2. Literature review

2.1 Rock cutting mechanism and its parameters

The rock cutting mechanism by the cutting tools including a pick cutter has been introduced by several previous studies (Potts and Shuttleworth, 1958; Evans, 1962; Reichmuth 1963; Mishnaevsky 1995; Ozdemir, 1995 and 1997). In all of the cases, the mechanisms are similar in all of the cutting tools (Bilgin et al., 2014). The theoretical, experimental, and numerical studies indicate that the crushed zone is generated within the rock beneath the pick cutter due to the high compressive stress region which is induced by the penetration of a pick cutter. The compressive stress induces the tensile stress and tangential cracks based on the Hoop stress theory.

The tensile fractures propagate to the free surface (direction of propagation is determined by minimizing of the fracture energy) or developed until it is connected to an adjacent tensile fracture. This interaction of the tensile fractures generates the rock chip, and this process is the general principle that the rock is cut by the cutting tool.

The cut spacing significantly influences to the efficiency of rock cutting. If the spacing between adjacent picks is too small, the adjacent picks cannot make significant rock chips. If the spacing is too large, they do not make the rock chip at all. Depending on the interaction between the adjacent cutter, the cutting mode is divided into relieved mode and unrelieved mode. The relieved mode means a cutting case where the interaction occurs between the cutters (the cut spacing is small or optimum), while the

unrelieved cut means that there is no interaction between the cutters (the cut spacing is large).

It is also important to determine the optimum cut spacing for the efficient excavation, and because the cut spacing determines the number of the cutter on cutting head, the cut spacing and corresponded the number of the cutter cannot be modified after the cutter-head is manufactured.

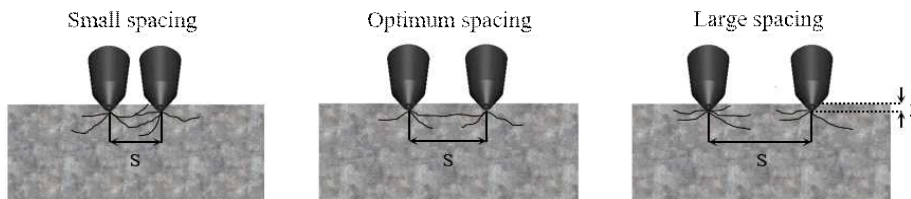


Figure 2.1 The rock cutting patterns by pick cutter according to the different cut spacings (modified from Balci and Bilgin, 2007)

When the cutting tools break the rock, the three orthogonal directional cutter forces act on the cutting tools. (Figure 2.2) The forces are the normal, cutting, and side forces, and they are important parameters to estimate the cutting performance and to design of the machine capacity. The normal force acts in a direction orthogonal to the cutting direction, which determines the thrust of the machine. The cutting force acts in a direction parallel to the cutting direction, which determines the torque of the machine. The side force, which acts in a direction orthogonal to the normal force and cutting force is the smaller than the other forces in general cutting condition. The side force affects to the balancing of the machine. These cutter forces are dependent on not only the cutting condition but also the

mechanical properties of the rock.

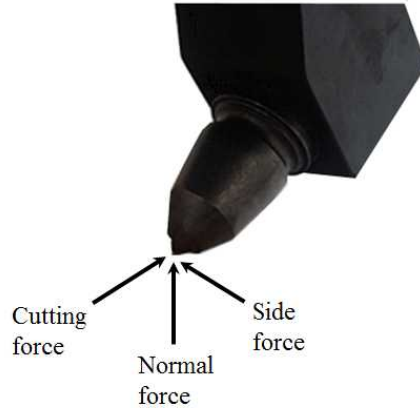


Figure 2.2 Three orthogonal forces acting on a pick cutter

The specific energy is a representative index to estimate the cutting efficiency for the mechanical cutting tool. It is defined by the required work to cut the unit volume of rock, and it is calculated by Equation 2.1.

$$SE = \frac{F_{c_mean} \times l}{V} \quad (2.1)$$

where, SE is the specific energy (unit: MJ/m³), F_{c_mean} is the mean cutting force of a pick cutter (unit: kN), l is the cutting distance (unit: mm), and V is the excavated rock volume (unit: m³). The specific energy is influenced by the cut spacing, and it is minimized at the specific cut spacing. The optimum cut spacing (or s/p ratio) is defined where the specific energy is minimized (Figure 2.3).

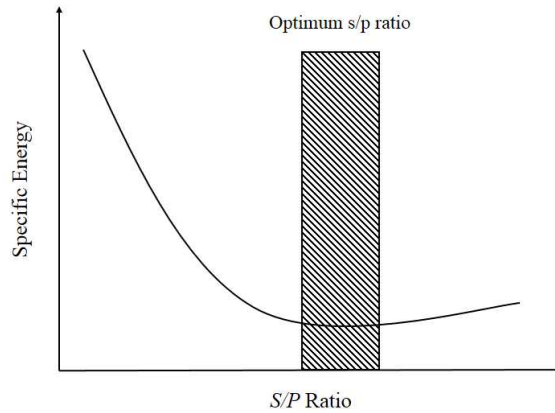


Figure 2.3 concept of the optimum cutting conditions (After Cho et al., 2010)

It is reported that the specific energy is increasing with the strength of rock and it is affected by the cutting condition (i.e., cut spacing and penetration depth). The specific energy is considered as the very important parameter which indicates the cutting efficiency and penetration rate of the machine as well.

The *ICR* (Instantaneous Cutting Rate) which was suggested to predict the performance of the mechanical excavation machine simply. There are different prediction model for *ICR* using various input parameters. Of the models, Rostami et al. (1994) suggested the prediction model using the specific energy. In the model, the penetration rate of the machine can be directly calculated by the specific energy. So the specific energy is an important parameter to estimate both the cutting efficiency and the machine's performance.

As explained in Chapter 1.1, RPM and cutting speed are also important design parameters for machine's operation and cutter-head design. Particularly in pick cutter, the attack angle and the skew angle (Figure 2.4) are special parameters which significantly affect to its performance and the cutting efficiency. It is physically natural that each component of the cutter force is dominantly influenced by the attack angle and the skew angle because the cutter force is decomposed according to the direction between the rock surface and the pick cutter. Therefore, it is necessary to consider these angle in the design of the machine using pick cutter because the cutting performance of pick is dominantly affected by these angles. The attack angle is defined as the angle of cutter axis from the rock surface, and the skew angle is defined as the minimum angle between the cutting direction and the projection of pick axis on the rock surface. The tilt angle is dependent on the skew angle and the attack angle, and it is defined as the angle between the normal direction of the rock surface and the pick axis. The parameters of a pick cutter described above are summarized in Table 2.1.

Table 2.1 The definition of the design parameters of pick cutter

Parameters	Unit	Definition
Peak cutting force (F_{c_peak})	kN	Peak force in the direction parallel to cutting direction
Mean cutting force (F_{c_mean})	kN	Mean force in the direction parallel to cutting direction
Peak normal force (F_{n_peak})	kN	Peak force in the direction perpendicular to cutting direction
Mean normal force (F_{n_mean})	kN	Mean force in the direction perpendicular to cutting direction
Specific energy (SE)	MJ/m ³	Work done by a pick cutter to break a unit volume of rock
Penetration depth (p)	mm	Cutting depth per 1 rev of cutter-head
Cut spacing (s)	mm	Spacing between the adjacent cutters
cutting speed (v)	m/s	Linear speed of the pick in cutting direction
Attack angle (a)	degree	Angle of pick axis from the rock surface
Skew angle (θ)	degree	The minimum angle between the cutting direction and projection of pick axis on the rock surface
Tilt angle (ϕ)	degree	The angle between the normal direction of rock surface and the pick axis

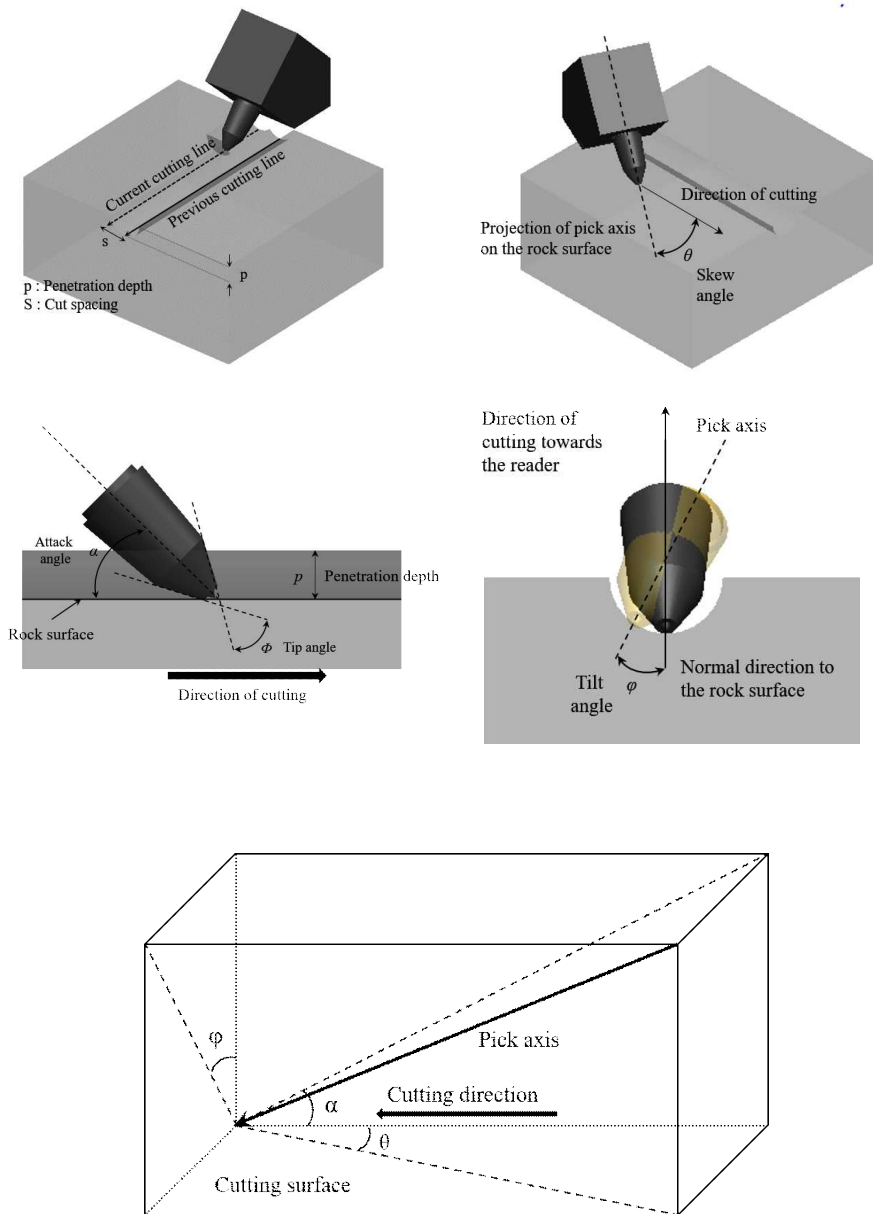


Figure 2.4 Definition of the parameters between rock and pick cutter (modified from Bilgin et al., 2014)

2.2 Theoretical studies

Many theoretical studies have been introduced to explain the rock-cutting mechanism induced by different types of cutting tools. Experimental and numerical studies also carried out to support the theories, the theories have been modified using their results.

Some of these theories are based on the tensile cracking and some of them on the shear cracking. Evans (1962; 1972a; 1972b; 1982; 1984a; 1984b) suggested the basic rock-cutting theoretical model for the chisel type pick cutter. The model has good agreement with experimental results, and it is reported that the model has been used to design the mechanical excavation machine until now. He indicated the tensile strength of rock is a predominant parameter in rock cutting process of chisel type pick cutter. The peak cutting force can be estimated by following equations (Equations 2.1 - 2.2);

For chisel pick,

$$F_{c_peak} = \frac{2\sigma_t d w \sin \frac{1}{2} \left(\frac{\pi}{2} - \alpha \right)}{1 - \sin \frac{1}{2} \left(\frac{\pi}{2} - \alpha \right)} \quad (2.1)$$

For conical pick,

$$F_{c_peak} = \frac{16\pi\sigma_t^2 d^2}{\cos^2 \left(\frac{\phi}{2} \right) \sigma_c} \quad (2.2)$$

where σ_t is tensile strength of rock, σ_c is uniaxial compressive strength of rock, d is penetration depth, w is cutter width, and the ϕ is angle of cutter tip.

On the other hand, Nishimatsu (1972) suggested the rock cutting theory was based on the shear failure mechanism, and he proposed a formula for calculation of the peak cutting force as shown in Equation 2.3. Based on the experimental results, he also reported the friction coefficient between the rock and the excavation tool, varies from 0.2 to 0.9 depending on the rock and material of cutting tool.

For chisel pick,

$$F_{c_peak} = \frac{2\sigma_s dw \cos \frac{1}{2}(\psi - \alpha) \cos(i)}{(13 - \alpha)[1 - \sin(i + \psi - \alpha)]} \quad (2.3)$$

where σ_s is the shear strength of rock, ψ is friction coefficient between rock and cutting tool, n is stress factor where $n = 12 - (\alpha/5)$, and i is internal friction angle of rock.

After Evan's theory was suggested, the model has been modified and verified by numerous experimental and numerical studies (Roxborough, 1973, 1985; Roxborough and Rispin 1973a, b; Bilgin, 1997). Evan's model has good agreement with the experimental results in the case of chisel type of pick cutter. However, the studies indicated the model should be improved in the case of a conical type of pick cutter. Goktan(1990), Roxborough and Liu(1995) suggested the modified Evan's model given as below;

For chisel pick,

$$F_{c_peak} = \frac{4\pi d^2 \sigma_t \sin^2\left(\frac{\phi}{2} + \gamma\right)}{\cos\left(\frac{\phi}{2} + \gamma\right)} \quad (2.4)$$

For conical pick,

$$F_{c_peak} = \frac{16\pi d^2 \sigma_t^2 \sigma_c}{\left[2\sigma_t \left(\sigma_c \cos\left(\frac{\phi}{2}\right)\right) \left(\frac{1 + \tan\gamma}{\tan\left(\frac{\gamma}{2}\right)}\right)\right]^2} \quad (2.5)$$

The theoretical and analytic prediction models have the advantage that the peak cutting force can be easily estimated using few input parameters, however, it is limited because the several important parameters (especially cut spacing) is excluded in the calculation. Moreover, only the peak cutting force can be estimated by the theoretical model in unrelieved cutting mode.

2.3 Experimental studies

Over the years, numerous experimental studies using different rock cutting test have been carried out to investigate the effect of influencing parameter on the cutting performance of a pick cutter. Bilgin et al. (2006) conducted a series of LCM test with a conical pick cutter on 22 rock types and experimentally analyzed the correlation between cutting performance, cutting conditions, and mechanical properties of the rocks. As the results, the uniaxial compressive and Brazilian tensile strengths of the rocks showed good correlations with the cutter forces. Also, the study indicated that the

theoretical model prediction differs from the result of the experiment, and suggested the correction coefficient of the theoretical prediction model through the experimental results. The study also reported that the skew angle up to 30 degrees, does not affect to the cutter force, and the skew angle has the positive effect on that cutter damage is reduced and rotation of cutter to generate a uniform wear, which is useful in increasing the cutter life.

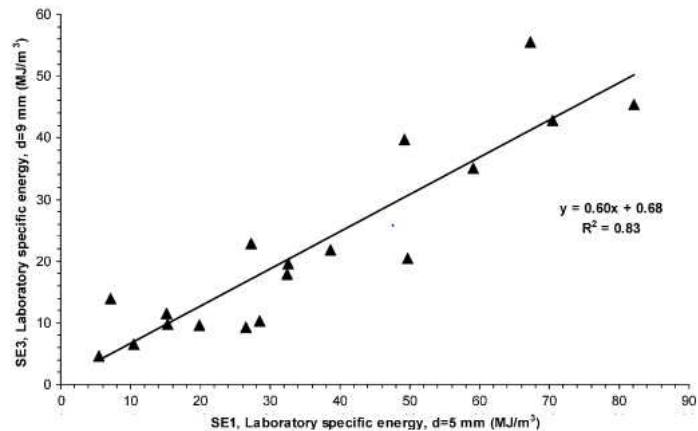
Tiryaki and Dikmen (2006) conducted a linear cutting test using a pick cutter on the various types of sandstones. From the results, they analyzed the correlation between specific energy and mechanical, petrological, and mineralogical properties of rocks.

Balci and Bilgin (2007) performed a series of full-scale and small-scale LCM test on 18 rock types, and they reported the relationship between the mechanical properties of rock and the specific energy. Also, the specific energy obtained from the small-scale LCM test and the full-scale LCM test have a good correlation with each other.

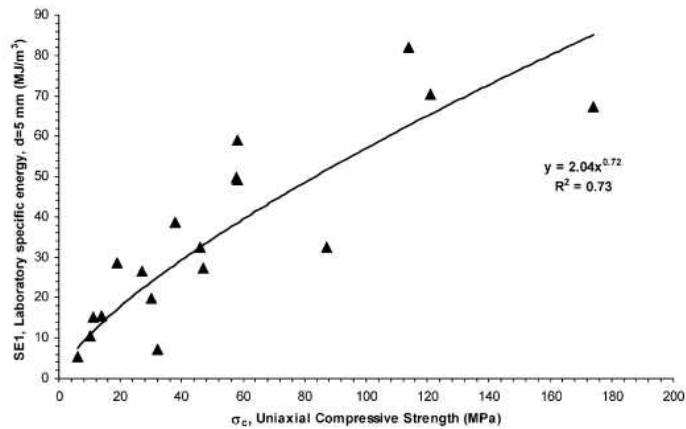
Copur (2010) analyzed the cutting efficiency of the chain-saw machine using the LCM test with chisel type cutters having different cutter tip angles. The optimal cutting conditions of the chain-saw machine were proposed through a series of linear cutting experiments with different parameters and cutting conditions (i.e., attack angle, cutter spacing, and penetration depth).

Choi et al. (2014a, 2014b) investigated that the effect of attack angle and skew angle on the cutting performance using the full-scale LCM test on the mortar specimen. The results indicated the 50° of attack angle is more

efficient cutting condition than 45° of attack angle, and 6° of the skew angle is more efficient condition than 0° of the skew angle. It is not enough to investigate the effect on attack angle and skew angle since it was performed under limited conditions.



(a)



(b)

Figure 2.5 The results from small and full scale LCM test: (a) relationship between specific energy obtained from two LCM tests, (b) the relationship between the uniaxial compressive strength and specific energy (Bilgin et al., 2007)

Bakar and Gertsch (2013) conducted a linear cutting test using a Chisel type cutter for saturated rock and dry rock and evaluated the cutting performance of the cutter according to the saturation of the rock. In saturated rocks, the cutter force is increased by about 10%, and the specific energy is increased by 30% more than the dry rock. It was also shown that there is a power series relationship between the Coarseness Index (CI) estimated from the size distribution of the rock chips and the specific energy.

Dogruoz et al. (2016) performed a linear cutting test on certain rocks using an artificially worn chisel pick cutter and observed the effect of the degree of wear of the pick cutter on the cutting performance. The study reported that as the wear of the cutter progresses, the cutter forces increase and the cutting efficiency decreases. The specific energy estimation equation is proposed through the relationship between the linear cutting test and the mechanical properties of the rock.

Park et al. (2016) conducted a series of small-scaled LCM tests using mortar specimens which have different uniaxial compressive strengths and investigated the effect of skew angle and attack angle on the cutting performance of the pick cutter. Especially, the skew angle is divided into positive and negative signs depending on the direction of pick cutter to rock surface and reported that the positive skew angle is more efficient cutting condition than the negative skew angle.

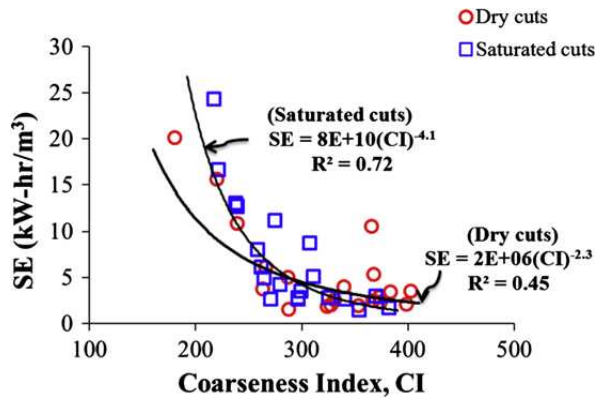
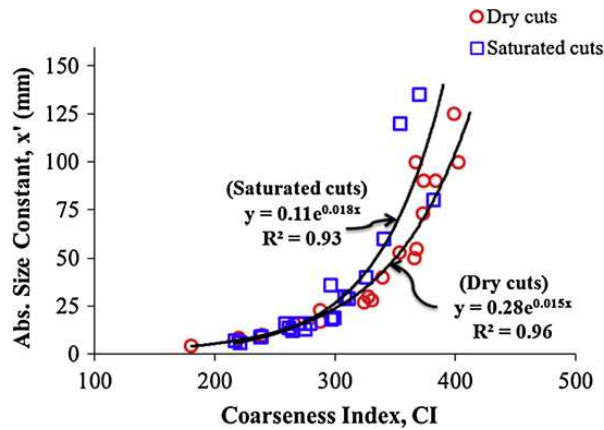


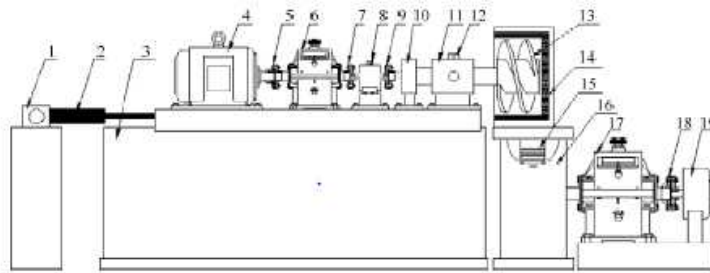
Figure 2.6 The effect of saturation of the rock on the cutting performance and size distribution of rock chip (a) the relationship between the CI and absolute constant size and (b) the relationship between the specific energy and CI (Barkar and Gertsch, 2013)

Shao et al. (2017) analyzed the effect of penetration depth, cut spacing, cutting speed, and attack angle on the cutting performance of pick cutter using linear cutting test using ANOVA technique. It is reported that the penetration depth has the most dominant influence on the mean cutting

force, attack angle, and cut spacing, and the mean normal force is influenced by the attack angle, penetration depth, and cut spacing. Based on the test results, the cutter force prediction model was proposed using multiple linear regression and artificial neural network. It is also reported that both the mean cutting force and the mean normal force are minimized where the attack angle is 60 degrees.

In addition to the linear cutting test, the rotary cutting machine test (Takaoka et al., 1974; Ozdemir et al., 1984; Liu et al., 2009) have been used to analyze the excavation efficiency of mechanical excavation machine. The advantage of the rotary cutting test (Figure 2.7) is that a large number of cutters are installed to simulate the cutting process with multiple cutting lines, and the reliability can be improved by acquiring data in a condition close to the actual cutting condition. However, it is known that the difference of experimental results between the rotary cutting test and the linear cutting test is not significant (less than 5%). Therefore, the linear cutting test which is relatively easy to test is preferred rather than the rotary type cutting test.

Liu et al. (2009) conducted a rotary cutting test using a drum type head equipped with a conical type pick cutter and found that the cutting force of the pick cutter has a linear relationship with the uniaxial compressive strength of the rock. Besides, the relationship between the cutting force and the cutter tip width was investigated, showing that there is an exponential relationship between the cutting force, the tip width, and the penetration depth of the cutter.



1, Hydraulic cylinder bracket; 2, Horizontal translation cylinder; 3, Horizontal translation guideway; 4, Electric motor; 5, Shaft joint 1st; 6, Reducer 1st; 7, Shaft joint 2nd; 8, Torque transducer; 9, Shaft joint 3rd; 10, Shaft block; 11, Force-measuring bracket; 12, Pressure transducer; 13, Test drum; 14, Test coal wall; 15, Pinion and rack; 16, Vertical translation guideway; 17, Reducer 2nd; 18, Shaft joint 4th; 19, Hydraulic motor

Figure 2.7 The concept of the rotary type of rock cutting tester (Liu et al., 2009)

As described above, the different rock cutting tests have been provided meaningful results for preliminary evaluation of the cutting performance of the machine in the field of mechanical excavation and designing the machine because the data deviation is not too large and the experimental condition can be examined in a variety of ways compared to the field data.

The theoretical models for estimating the peak cutting force acting on the pick cutter was introduced in Chapter 2.3, and the prediction models for estimating the cutter forces of the pick cutter were proposed based on the experimental results by various researchers. Table 2.2 summarizes the cutting force estimation models proposed in various papers. Of the prediction models, the most models proposed the prediction model for calculation of the cutting force (especially peak cutting force), and only the model of Bilgin et al. (2006) proposed a separated models for the normal force and the cutting force.

Table 2.2 The prediction models to estimate the cutter forces

Researcher	Normal force (N)	Cutting force (N)	Remarks
Evans(1962; 1972a; 1972b; 1982; 1984a; 1984b)	-	$FC = \frac{2\sigma_t d w \sin \frac{1}{2} \left(\frac{\pi}{2} - \alpha \right)}{1 - \sin \frac{1}{2} \left(\frac{\pi}{2} - \alpha \right)}$	chisel
	-	$FC = \frac{16\pi\sigma_t^2 d^2}{\cos^2 \left(\frac{\phi}{2} \right) \sigma_c}$	conical
Nishimastu (1972)	-	$FC = \frac{2\sigma_s d w \cos \frac{1}{2} (\psi - \alpha) \cos(i)}{(13 - \alpha)[1 - \sin(i + \psi - \alpha)]}$	chisel
Ernst-Merc hant (1941)	-	$FC = 2wd\sigma_s \tan^{1/2}(90 - \alpha - \psi)$	chisel
Goktan (1990)	-	$FC = \frac{4\pi d^2 \sigma_t \sin^2 \left(\frac{\phi}{2} + \gamma \right)}{\sin \left(\frac{\phi}{2} + \gamma \right)}$	conical
Roxboroug h and Liu (1995)	-	$FC = \frac{16\pi d^2 \sigma_t^2 \sigma_c}{\left[2\sigma_t \left(\sigma_c \cos \left(\frac{\phi}{2} \right) \right) \left(\frac{1 + \tan \psi}{\tan(\psi/2)} \right) \right]^2}$	conical
Bilgin et al. (2006)	$FN = 1.217\sigma_c^{1.104} \times d$	$FC = 0.826\sigma_c + 21.76$	conical
Yilmaz et al. (2007)	-	$FC = -24.504 + 0.513\sigma_s + 1.873d + 0.249f + 0.227W - 0.154\alpha - 0.047\sigma_c$	chisel

On the other hand, the machine performance is defined by field penetration index (*FPI*) which indicates the required cutter force according to penetration depth. The *FPI* can be expressed as follow (Klein et al., 1995; Barton, 2000; Gong et al., 2007; Hassanpour et al., 2009, 2010, 2011)

$$FPI = \frac{F_n}{PR} \quad (2.6)$$

where F_n is the thrust force per cutter (kN) and PR is the penetration rate (mm/rev). The *FPI* is commonly used to represent the boreability of the rock. Using this approach, the three directional cutter forces of a pick can be quantified with force index (*FI*) which means the required cutter force per unit the penetration depth as follows:

$$FI_{n,c,s} (kN/mm) = \frac{F_{n,c,s}}{p} \quad (2.7)$$

where FI_n , FI_c , FI_s are force indices for the normal, cutting and side force, respectively. F_n , F_c , F_s (unit: kN) are the normal force, cutting force and side force, respectively, p is penetration depth in mm.

2.4 Numerical studies

Numerous numerical studies have been carried out to simulate the rock cutting process by the different cutting tools; Finite element method, discrete element method (particle flow code), finite differential method, smooth particle hydrodynamics, etc. Of the numerical methods, the finite element method is the most common method in rock mechanics field.

Cho et al. (2010, 2013) introduced the numerical method to simulate the rock cutting process by the TBM disc cutter. The rock chipping phenomenon was simulated by using the erosion technique for the eight different rock types, and the applicability of the numerical model was evaluated by comparing the specific energy results obtained from the numerical simulation and the LCM test.

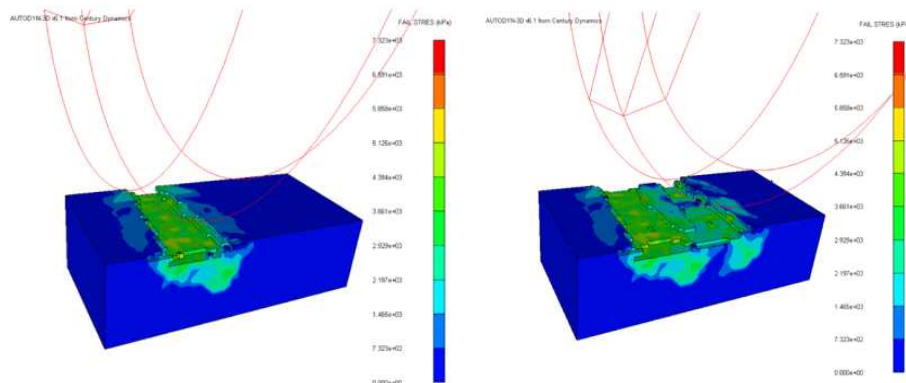


Figure 2.8 The numerical simulation of rock fragmentation by TBM disc cutter using AUTODYN (Cho et al., 2010)

Menezes et al. (2014) simulated the rock cutting process of chisel type pick cutter using LS-DYNA, a commercial program based on the finite element method. He studied on the cutting force and the rock cutting efficiency for various cutter shape conditions.

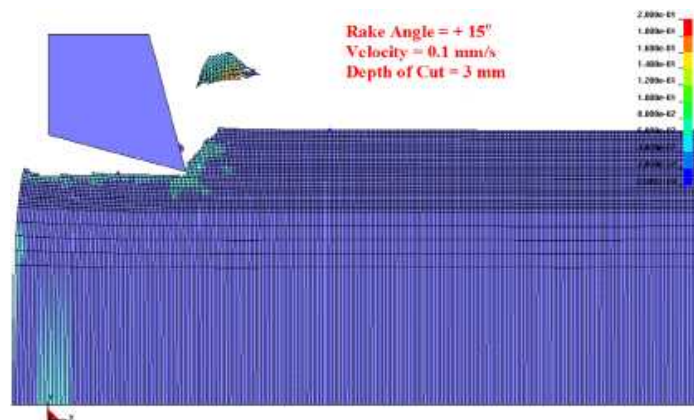


Figure 2.9 The numerical simulation of rock cutting by chisel type pick cutter using LS-DYNA (Menezes et al., 2014)

Geng et al. (2016) simulated the fragmentation process of rock in the rotary cutting test using ABAQUS based on finite element method. The modified Drucker-Prager (DP) model was used to distinguish the stress-strain relationship in the tensile and compression region. The optimum cutter spacing was derived from a series of numerical simulation, and the results were compared with the results of the rotary cutting test.

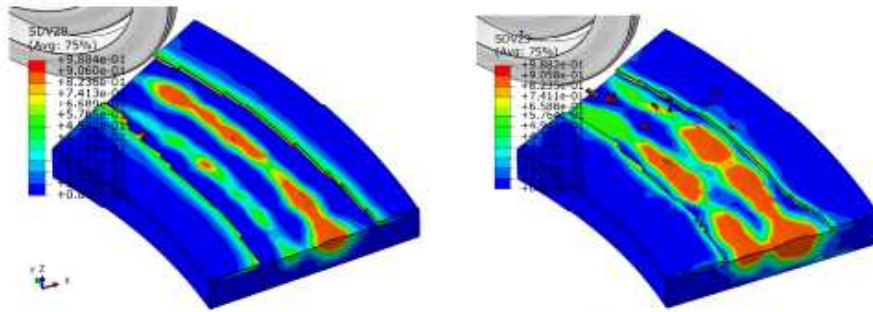


Figure 2.10 The numerical simulation of rock cutting process by a TBM disc cutter using ABAQUS (Geng et al., 2016)

Geng et al. (2017) reported that traditional FEM simulations on the rock cutting process by TBM disc cutters might be improved considering the following shortcomings; 1) the troughs of the numerical forces are usually much lower than those of the field or experimental forces; and (2) the rocks beneath the cutter tip are usually cut off excessively, while the chipping of the rocks between the cutting kerfs is usually less than real. Also they discussed the reason is as follows; (1) the plastic hardening and failure behaviors are assigned the same for different rock parts, which is different from the real rock breaking principle; and (2) directly using the element deletion strategy to simulate the rock chipping cannot consider the crushing process between the cutter tip and rock specimen.

In order to solve the problem that the crushing process under the cutter is not well simulated in the finite element method, the cutter beneath part and the bottom part of the rock were modeled by the different failure model, the tensile failure of the rock does not occur in those parts so that the cracking by the tensile stress does not occur (Figure 2.11). Therefore,

tensile cracking only occurs in the area which located between the adjacent cutters.

As a result, the crushing process under the cutter was reflected, and the cutter force, especially the normal force of a disc cutter could be obtained similarly to the RCM test results. Also, they indicated that in the rock cutting process, it is important to simulate the crushed zone which represents the high compressive stress region.

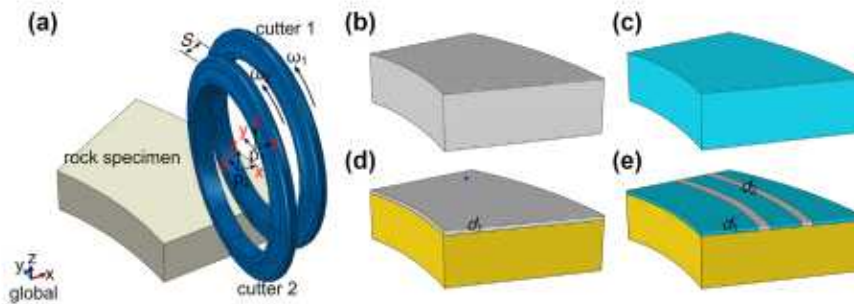


Figure 2.11 The partial modeling of rocks for rock crushing simulation in finite element method (Geng et al., 2017)

On the other hand, Rojek et al. (2011) used the DEMPack program based on the discrete element method to simulate the fragmentation process of the rock by a conical type pick cutter with a two-dimensional and three-dimensional model, and the results were compared with each other. The study tried to estimate the size distribution of rock chips by measuring the frequency of cutter force by numerical analysis. A series of results show that the DEM technique is suitable for simulating the crushing process of rocks.

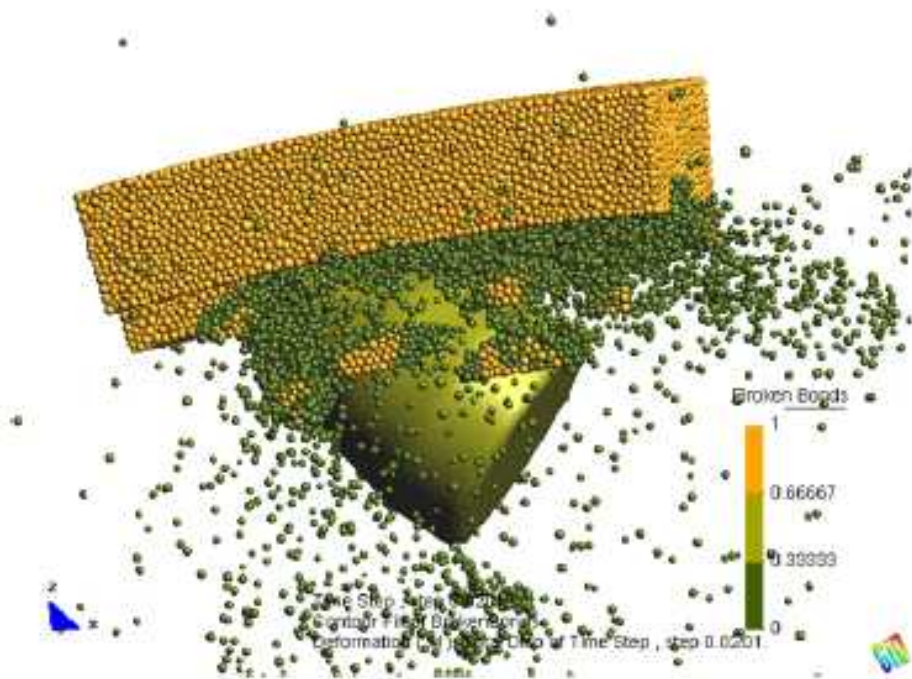


Figure 2.12 Rock cutting simulation of conical pick cutter using discrete element method, DEMPack (Rojek et al., 2011)

Also, Su and Akcin (2011) used the PFC3D, a discrete element method program, to simulate the cutting process of a rock by a conical type pick cutter and analyzed the result of the cutter forces measured in numerical simulation. The study proposed the equation for the relationship between the cutter forces obtained from the linear cutting test and those from the PFC3D.

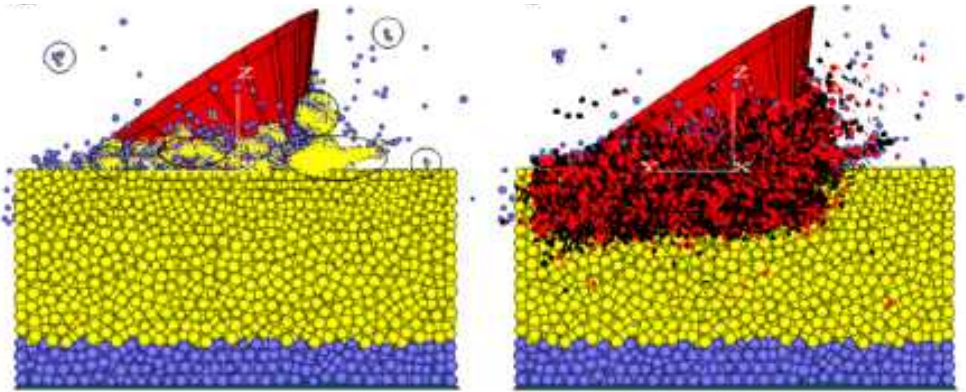


Figure 2.13 Rock cutting simulation of conical pick cutter using PFC-3D (Su and Akcin, 2011)

Lee and Choi (2013) also carried out the numerical simulation of rock cutting using the PFC3D, which simulates the rock cutting process of a rock by TBM disc cutter. They reported that the PFC could simulate the cutting process of rock by comparing the cutter force obtained from PFC and linear cutting test.

In the particle flow code (PFC), the crack propagation process and the fragmentation of the rock are simulated in reality as compared with the FEM as explained above. However, in order to determine the mechanical properties of rocks, it is necessary to find the micro parameters of the particle through repetitive preliminary analysis.

On the other hand, SPH (Smooth Particle Hydrodynamics) technique has been recently applied to the rock cutting simulation. In the SPH code, since the input parameters were determined by the laboratory test, and it is the same with the finite element method program. Thus, it is unnecessary to determine the micro parameters.

Jeong et al. (2013) introduced and employed the SPH code to simulate the rock cutting process by the TBM disc cutter. The cutter forces from numerical simulation and the LCM test have good agreement with each other, and the propagation pattern of the cracks and the fragmentation pattern of the rocks were also similar. Besides, the measured optimum cutter spacing was consistent with the LCM test results. The results showed the applicability of numerical simulation using SPH codes in rock cutting simulation.

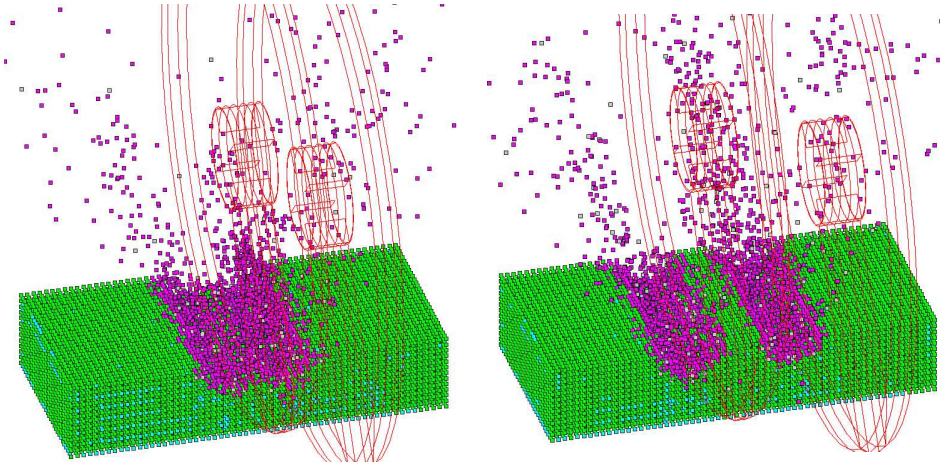


Figure 2.14 Rock cutting simulation of TBM disc cutter using SPH code
(Jeong et al., 2013)

Helmons et al. (2016) used the particle bonded model and SPH to investigate the effect of the pore pressure on the rock and the cutting speed of the cutter on the cutting performance when the pick cutter cuts the saturated rock in water. As a result, it was reported that the cutter force increases with the ambient pressure and is affected by the pore pressure and permeability coefficient.

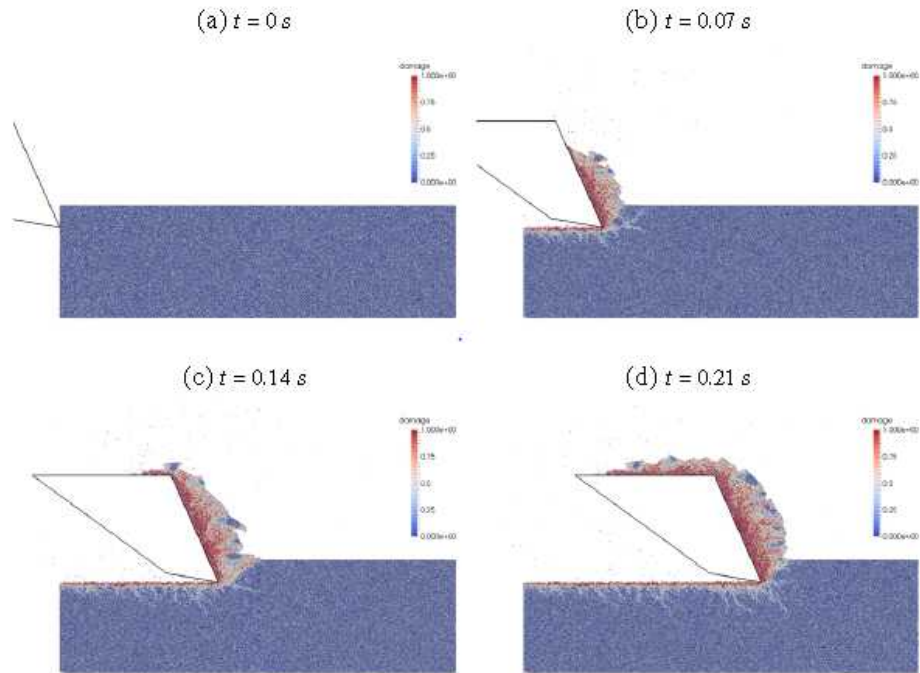


Figure 2.15 Rock cutting simulation of pick cutter in saturated rock using DEM/SPH coupled code (Helmons et al., 2016)

Xiao et al. (2017) simulated the fracture process of rock by penetration of a disk cutter into the rock using finite element method and SPH coupled method. The stepwise fracture zone formed by the penetration of the cutter was compared with the experimental results, and the applicability of the numerical model was evaluated. However, there is a limitation in that it does not observe the effect of the cutter spacing because the model simulated the rock fragmentation of the single cutter.

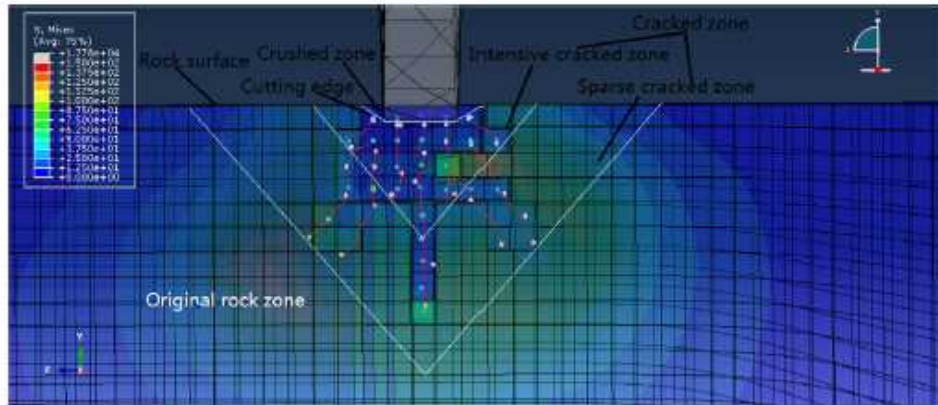


Figure 2.16 Rock cutting simulation of the disc cutter using FEM/SPH coupled code (Xiao et al., 2017)

Although the above numerical studies attempted to simulate the rock cutting process by the different cutting tools using various numerical techniques and software, their common aim is 1) to simulate the fragmentation process of the rock by the cutting tool, 2) accurately predict the cutter force of the cutting tool, 3) Finally, it can be judged that the cutting performance and efficiency of the rock are evaluated accurately, so that the numerical modelling can be substituted the rock cutting test and applied to the actual design of the mechanical excavation machine.

2.5 Chip size distribution

As explained in Chapter 1.1, the particle size distribution of rock chip produced by rock excavation provides useful information to estimate the cutting efficiency indirectly, and for reusing the rock chip as the

construction material.

Firstly, the size of rock fragments produced in mechanical excavation is well studied both in the laboratory scale and in the field and is related to parameters such as specific energy, and applied cutter load among other parameters (Farrokh and Rostami, 2008)

Pfleider and Blake (1953) concluded that a rough correlation exists between penetration rate and production of cutting, and Ersoy and Waller (1997) found that the wear rate of bits depends upon the particle size produced during drilling. Since then, it has been reported that there is a high correlation between particle size and specific energy, which represents excavation efficiency.

Ozdemir (1995) reported that the specific energy reduces drastically as the chip size increase (Figure 2.17) and that the bigger mean chip size, the lower SE and the more efficient the mechanical excavation process becomes (Tiraky et al., 2010).

Rostami et al. (2002) studied on the chip sizes and the frequency of the signal generated by rock fragmentation under a disc cutter. Bruland (1998) also carried out the chip size analysis for the muck produced by TBM excavation and reported the relationship between the chip size and cutter force, specific energy.

Farrokh and Rostami (2008) quantitatively analyzed the size of muck excavated by TBM in fractured rock and compared the results with thrust and torque of TBM.

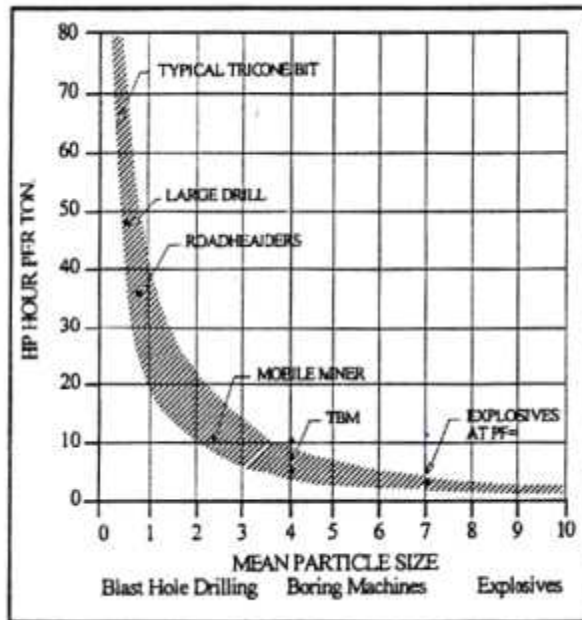


Figure 2.17 Typical specific energy archived by different mechanical excavation machines (Ozdemir, 1995)

Roxborough (1973) found in rock cutting experiments that CI values followed a reverse trend to the specific energy. The higher CI values coincided in all cases with lower specific energy values for different operational parameters, i.e., depth of cut in both cutting rocks with disc cutters and chisel picks.

Altindag (2003) analyzed the relationship between the size distribution parameters of rocks (i.e., coarseness index, mean particle size and specific surface area) and performance of percussive drilling. As a result, it was reported that the penetration rate of percussive drilling is highly correlated to the parameters indicating the size distribution of rock.

Kahraman (2004, 2005) reported that the relationship between the coarseness index of rock chip produced by top hammers and down the hole drills and its penetration rate, the results indicated that penetration rate and CI decreased with drilling depth in top hammer drills.

Tuncdemir et al. (2008) performed LCM test using conical pick cutters for 17 rocks and analyzed the correlation between cutting conditions, specific energy and coarseness index. As a result, the specific energy decreased as the CI increases, and the CI has the maximum value at the optimum cut spacing. Also, CI increased with increasing penetration depth.

3. Methodology

3.1 Scaled linear cutting machine system

This study used the small-scale linear cutting machine (SLCM) for the experimental work (Figure 3.1). The system has a 20 tons loading capacity and can sustain sufficient stiffness during the linear cutting test. The system consists of the main frame, an electronic motor unit, and a control panel. The main frame features a large stiff frame on which the conical pick is mounted. The cutter forces in three directions (normal, cutting, and side force) were measured in real time during the test with a load cell installed between the head of the main frame and the conical pick (Figure 3.2). The rock sample is within a steel box to provide efficient confinement during testing. The positions of the rock specimen and the pick cutter were controlled using the control panel, especially, the movement (cutting direction) of the rock specimen was servo-controlled to maintain a constant cutting speed. The cutting distance was also automatically controlled using the control panel to prevent the end effect of the specimen. The cut spacing was manually controlled, and the position of the specimen is displayed in the control panel (Figure 3.3).

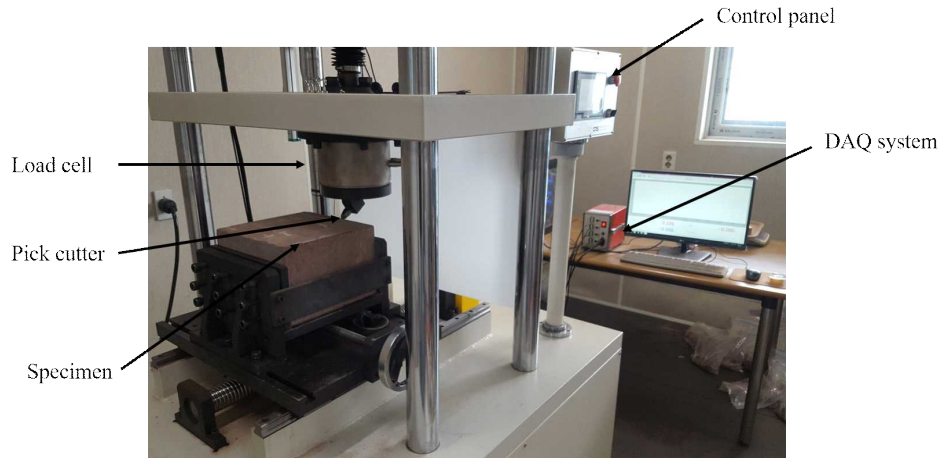


Figure 3.1 The small scaled linear cutting machine system in this study



Figure 3.2 The load-cell to measure the three directional cutter forces

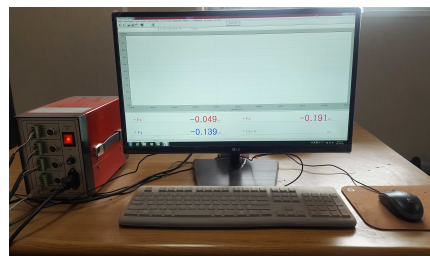


Figure 3.3 The control panel and data acquisition in LCM system

The skew angle was applied by manually rotating the cutter plate located between the pick cutter and the load cell. Figure 3.4 shows the cutter plate to make the skew angles. By mechanically combining the bolts in the load cell with the specific combination of the holes in the plate, the skew angle can be applied.



Figure 3.4 The cutter plate to set the different skew angles

The attack angle can be set with a cutter holder that connects the cutter and the plate (Figure 3.5). The cutter holders were made to be having 30° to 60° at 5° intervals.



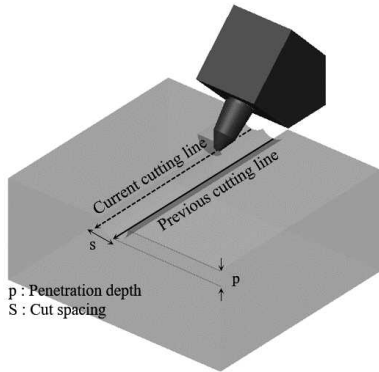
Figure 3.5 The cutter holders to set the different attacks

3.2 Experiment design

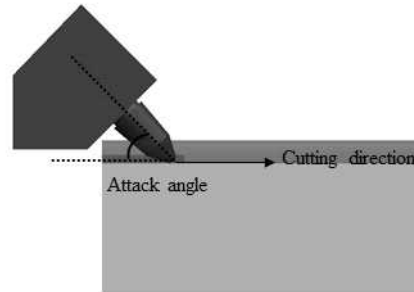
The test conditions considered in this study are as follows and they are described in figure 3.6:

- Testing variables are:
 - Rock type : Linyi sandstone, concrete (Conglomerate-like)
 - Penetration depth (p) : 5, 7, 9, 11 mm
 - Cut spacing (s) is varied with penetration depth, it is determined by the s/p ratio.
 - Attack angle (α) : 35, 45 and 55 degrees
 - Skew angle (θ) : 0, ± 5 , 10, 15 and 20 degrees

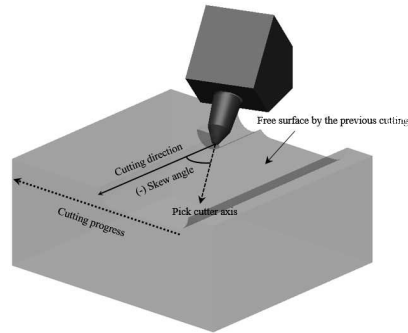
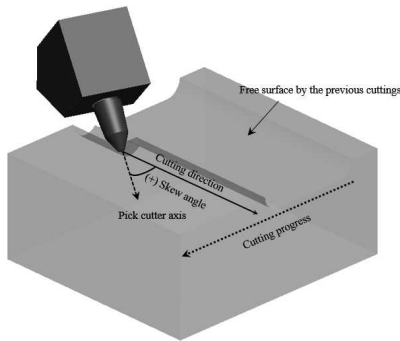
- Main observations are:
 - Cutter forces : peak normal force (F_{n_peak}), peak cutting force (F_{c_peak}), peak side force (F_{s_peak}), mean normal force (F_{n_mean}), mean cutting force (F_{c_mean}), and mean side force (F_{s_mean})
 - Specific energy (SE)
 - Force ratio : peak to mean forces, cutting to normal forces, cutting to side forces
 - Chip size distribution : Uniformity (N) and absolute size constant (D) are from Rosin-Rammler distribution and coefficients of uniformity (C_u) and curvature (C_c) are based on the soil mechanics theory.
 - Optimum cutting condition under different cutting condition
 - Force Index (FI)



(a) penetration depth and cut spacing



(b) attack angle



(c) positive and negative skew angles

Figure 3.6 The definition of the testing variables in LCM test

Testing procedure of in this study is as follows;

First of all, the optimum cutting conditions were determined for each penetration depth with 45° of attack angle and 0° of skew angle, and the effect of the penetration depth and cut spacing on the dependent variables. The testing conditions are considered as the basic cutting condition in this study.

After the procedure, the effect of the attack angle and skew angle on the dependent variables under the optimum cutting conditions. The attack angle

varies from 35° to 55° in three levels, and the skew angle varies from -20° to $+20^\circ$ in nine levels.

The effect of the attack angle on the cutting performance of the pick cutter was investigated with three the attack angle at the different penetration depth and cut spacing where the fixed skew angle as 0° .

3.3 Experimental set-up

3.3.1 Specimens

The rock specimen were the Linyi sandstone from China and were cut to 300 mm x 300 mm x 200 mm for testing purpose, and the concrete specimen was made in the same size of Linyi sandstone specimen. The mechanical properties of the Linyi-sandstone and concrete are presented in Table 3.1 and 3.2, respectively. The mixing ratio of the concrete was presented in Table 3.3. The size of maximum coarse aggregate is 25 mm. The admixture ① is a solid material and used for the target mechanical properties, and admixture ② is liquid material and used to control curing time considering the temperature.

Table 3.1 Mechanical properties of Linyi-sandstone

Properties	Unit	Value
Density	g/cm ³	2.4
Porosity	%	8.2
Uniaxial compressive strength	MPa	64.0
Brazilian tensile strength	MPa	4.7
Young`s modulus	GPa	10.2
Poisson`s ratio		0.2
Schmidt hammer rebound hardness*		57.3
Shore hardness*		43.5
P-wave velocity	m/s	2317
S-wave velocity	m/s	1531

**Schmidt hammer rebound and Shore hardness values were obtained by averaging the upper 10 values from 20 tests performed.*

Table 3.2 Mechanical properties of Concrete

Properties	Unit	Value
Density	g/cm ³	2.3
Uniaxial compressive strength	MPa	21.0
Brazilian tensile strength	MPa	2.1
Young`s modulus	GPa	21.9
Poisson`s ratio		0.17
Slump	mm	150
Maximum size of coarse aggregate	mm	25

Table 3.3 Mixing ratio of the concrete

Materials	unit	value
Cement		11.99
Water		7.31
Fine aggregate ①		18.85
Fine aggregate ②		18.85
Coarse aggregate ②		40.86
admixture ①	%	2.10
admixture ②		0.04
Total		100.0
The ratio of water to binder		51.8
The proportion of fine aggregate		48.2
Total		100.0

Two rock specimens were considered as the isotropic rock in this study, Linyi sandstone was a homogeneous rock and concrete was a heterogeneous rock. It is known that some of the sandstone has an anisotropy depending on the origin of the rock, the degree of anisotropy of rock also depends on the characteristic of rock. However, it is supported that the degree of anisotropy of Linyi sandstone is not remarkable or be negligible from the previous studies (Yang and Jing, 2011; Kim 2017). Figure 3.7 shows SEM (scanning electron microscope) images of the Linyi sandstone (Kim, 2017) at different magnifications, and the anisotropy of the Linyi sandstone was not observed in the SEM images. Referred the previous studies, in this study, it is assumed that Linyi sandstone does not affect the test results.

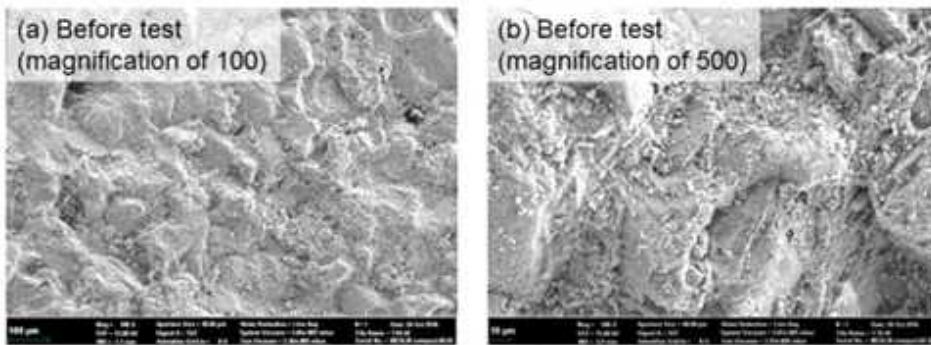


Figure 3.7 SEM images of Linyi sandstone at the different magnifications:

(a) 100× and (b) 500× (Kim, 2017)

3.3.2 Cutting tool

The conical pick (Model: PN 735MB) used in this study was manufactured by Vermeer Corporation. There are different types of a pick cutter for the trencher. The pick cutter is suitable for the soft - to the medium strength of rock considered the dimension, shape, and insert of a pick. The information is referred by the catalog provided by the Vermeer (2017). It is shown in Figure 3.8 with a schematic diagram. The cutter geometry has the gauge of 40 mm, primary tip angle of 70° , tip diameter of 12 mm, the flange diameter of 30 mm, and the shank diameter of 18.5 mm.

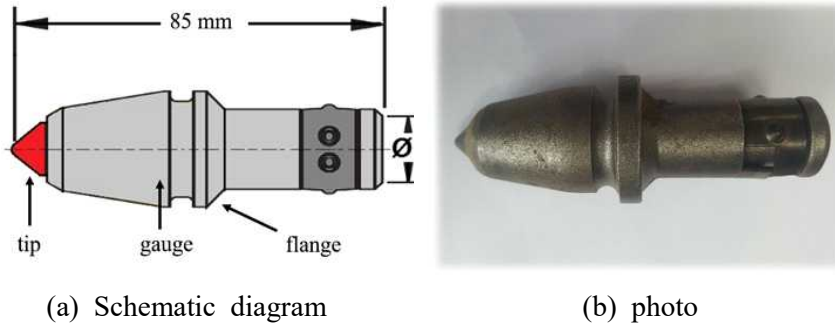


Figure 3.8 A schematic diagram and photo of pick cutter used in this study

3.3.3 Measurement of cut rock volume

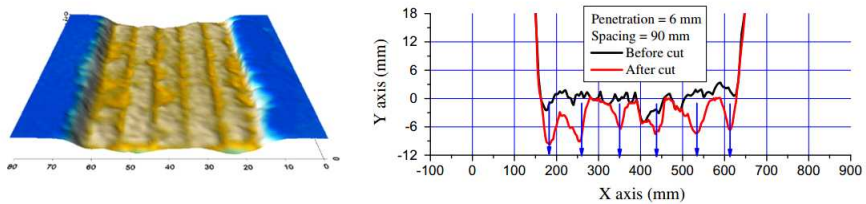
Many approaches have been introduced for measuring excavated rock volume in the linear cutting test procedure. In the approximation method (Sanio, 1985; Chang et al., 2006; Gerthsch et al., 2007), the excavated rock volume is calculated from the cutting geometries (i.e., cut spacing, penetration depth, and cutting distance) with the assumption that rock chips between two adjacent cutting grooves are completely removed from equation 3.1 (Cho et al., 2013).

$$V_{cut} = l \times p \times S \quad (3.1)$$

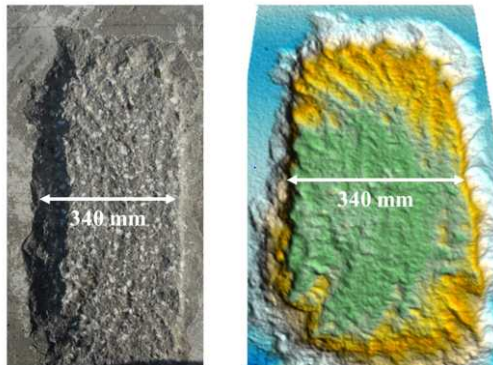
where the V_{cut} is cut rock volume, l is the cutting distance, p is penetration depth, and S is cut spacing. However, it is far from reality and cutting efficiency is overestimated where the cut spacing is larger than optimum cut spacing. To improve an accuracy of measuring excavated rock

volume, weighing method (Roxborough and Phillips, 1975; Snowdon et al., 1982; Balci and Bilgin, 2007; Tuncdemir et al., 2008).

Also, photogrammetric (or image processing) measurement (Cho et al., 2013; Ryu, 2016) have been used to measure cut volume in linear cutting test procedure (Figure 3.9) Compared the weighing method, the photogrammetric measurement provides advantages in terms of the loss of small portions of rock debris and rock powder that escape from LCMs during testing (Cho et al., 2013).



(a) TBM disc cutter (Cho et al., 2013)



(b) Hammer bit (Ryu, 2016)

Figure 3.9 A photogrammetric system for measurement of rock volume in rock cutting by different cutting tools

In this study, the rock debris was collected after each cutting test to measure the cut rock volume and to analyze the size distribution of the rock chip. To prevent the loss of small rock particles, a vinyl fence was installed around rock specimen during the test, and the rock debris was carefully collected using a designated vacuum cleaner.

3.3.4 Cutting test procedure

Before the cutting tests, the specimens were preconditioned by preliminary cutting to make the damaged rock surface which is the same condition with the actual excavated surface (Figure 3.10, $p = 3$ mm and $s = 10$ mm), and then the experiment was performed according to the given cutting conditions.

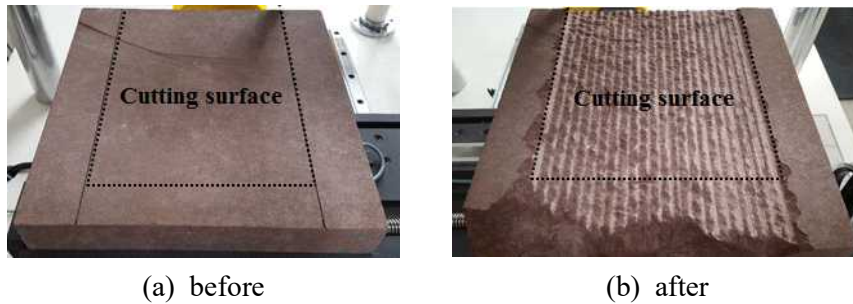


Figure 3.10 The rock specimen (a) before and (b) after preconditioning

The constant variables in the testing are the cutting sequence (single-start), the cutting speed (10 mm/s). The cutter forces in three directions (normal, cutting and side force) were measured with the three-directional load cell, and data sampling rate of 20 s⁻¹. The cutting distances were 220 - 270

mm for all cutting conditions, and the number of cutting line was at least five for each case. It is reported that cutting speed does not affect the cutter forces and the specific energy (Roxborough and Phillips 1975; Sanio, 1985; Hood et al., 1989). However, it can significantly affect to cutter wear due to high heat generation. (Bilgin et al., 2014) In this study, it was assumed that the cutting speed does not affect the cutting performance of pick cutter.

Regarding the small size of the specimen in the small scaled LCM test, there are important considerations as followings:

1) Although the rock specimen is smaller than that of the full-scaled LCM test, the cutting tool can be used for the LCM test. If the small scaled cutting tool was used, then the test condition is index cutting test such as core cutting test.

2) Cutting distance: The full-scaled LCM test is also used to simulate the rock excavation process with small scale condition regarding cutting distance. Therefore, the reduced cutting distance in small scaled LCM test is reasonable compared with the full-scaled LCM test.

3) Edge effect: In full scaled LCM test, sufficiently large specimen (i.e., 1000 mm x 1000 mm x 300 mm) is used to prevent the breakage in the edge of the specimen (in cutting direction) due to the repetitive cutting tests. Nevertheless, the use of that size of the specimen, the breakage in edge should occur. The part of the rock broken by the edge effect should be excluded from the result analysis

4) Cutting lines: It is the main difference between the small scaled and full scaled LCM tests. Bilgin et al. (2014) reported that each testing should

be repeated at least three times. To minimize the effect of a number of the cutting lines, it is suggested that the number of cutting line constantly keep for all testing conditions.

3.4 Measurement of chip size distribution

3.4.1 Size distribution

This study investigated the size distribution of rock chip produced by the LCM test. The fragment size can provide useful information for evaluating the cutting efficiency. Measurement of fragment size of the rock is important to assess the efficiency of the cutting process of the mechanical excavation machine and the production mining operation. The degree of rock fragmentation plays an important role in order to control and minimize the overall production cost. It is known well that the specific energy decreases drastically as the chip size increase.

Several studies have introduced and adopted the coarseness index (*CI*) to quantify the size distribution of rock debris (Roxborough and Rispin, 1973; McFear-Smith and Fowell, 1977; Altindag, 2003; Tuncdemir et al., 2008; Abu Bakar and Gerstch, 2013). The *CI* is a dimensionless value and is calculated by the sum of the cumulative weight percentages retained on each sieve used. However, the *CI* is dependent on the sieve size, so it changes according to the sieve size. Thus, the coarseness index can be used to compare the relative characteristics of rock particle sieved by the same set of sieves. In this study, the maximum and minimum sieve size were 19.1 mm and 1.64 mm in diameter, respectively, and Table 3.4 shows the

representative results of the *CI*.

Table 3.4 The example of the calculation of coarseness index (CI) for Linyi sandstone at $p = 9$ mm and $s = 18$ mm

Size fraction (mm)	Retained mass (g)	Cumulative mass (%)
+19.1	73.86	16.72
-19.1 +13.2	134.07	47.06
-13.2 +9.28	76.32	64.33
-9.28 +6.56	34.02	72.03
-6.56 +4.64	32.39	79.37
-4.64 +3.28	15.84	82.95
-3.28 +2.32	9.34	85.06
-2.32 +1.64	6.62	86.56
-1.64	47.3	97.27
Total mass	429.76	<i>CI</i> = 631.35

The other size distribution parameters can be obtained from the Rosin-Rammler distribution (Rosin and Rammler, 1933) also represents the mass (volume) distribution as:

$$R = 100e^{-\left(\frac{x}{D}\right)^N} \quad (3.1)$$

Rearranging and taking the logarithm twice of both sides of equation 3.1 then the equation can be expressed as:

$$\log \left[\log \left(\frac{100}{R} \right) \right] = N \times \log(x) + D \quad (3.2)$$

The parameters of the Rosin-Rammler distribution, N and D are obtained from the slope of the straight line and the intercept at the $R = 36.79$ %,

respectively (substitution $x = N$ in equation 3.1 produces a constant of about 36.79 % material retained). Together N and D describe the size distribution for a given specimen of rock fragments subject to sieve analysis. The small value of N means that spread over a wide size range, whereas larger values of b indicate that the curve is steeper and the material is spread over a narrower range of sizes (Gupta and Yan 2006; Brezani and Zelenak, 2010; Abu Bakar et al., 2014). The SPLIT-DESKTOP automatically provide the parameters based on the image processing results and the equations described above.

On the other hand, the coefficients of uniformity (C_u) and curvature (C_c) are generally used to represent the distribution of soil particles. The two coefficients can be calculated by equations 3.3 and 3.4.

$$C_u = \frac{D_{60}}{D_{10}} \quad (3.3)$$

$$C_c = \frac{(D_{30})^2}{D_{60} \times D_{10}} \quad (3.4)$$

where effective sizes D_{10} , D_{30} and D_{60} are the diameters in the particle-size distribution curve corresponding to 10%, 30%, and 60% finer, respectively.

3.4.2 Spilt desktop

There are several software programs to analyze the size distribution of rock fragmentation using an image processing; namely SPLIT-DESKTOP, Wipfrag, Goldsize, Fragscan, TUCIPS, CIAS, PowerSieve, etc. This study used the SPLIT-DESKTOP system for the chip size analysis.

The flow of image processing is as following (Figure 3.11):

- 1) Crop the acquired image by separating the parts of the rock debris and the unnecessary parts.
- 2) Set the scale using the ruler in the image.
- 3) Use the auto-delineation provided by the Split desktop to delineate each rock chip.
- 4) After confirming the auto-delineation results, manually correct any abnormally separated or non-separated rock fragments. Small particles that are difficult to delineate are set as fine material. (fine factor = 5)
- 5) Determine the size of sieve set for size distribution analysis. The sieve size should be set so that all of the rock fragments can be analyzed (at least larger than the biggest rock fragments)
- 6) Report the result of size distribution

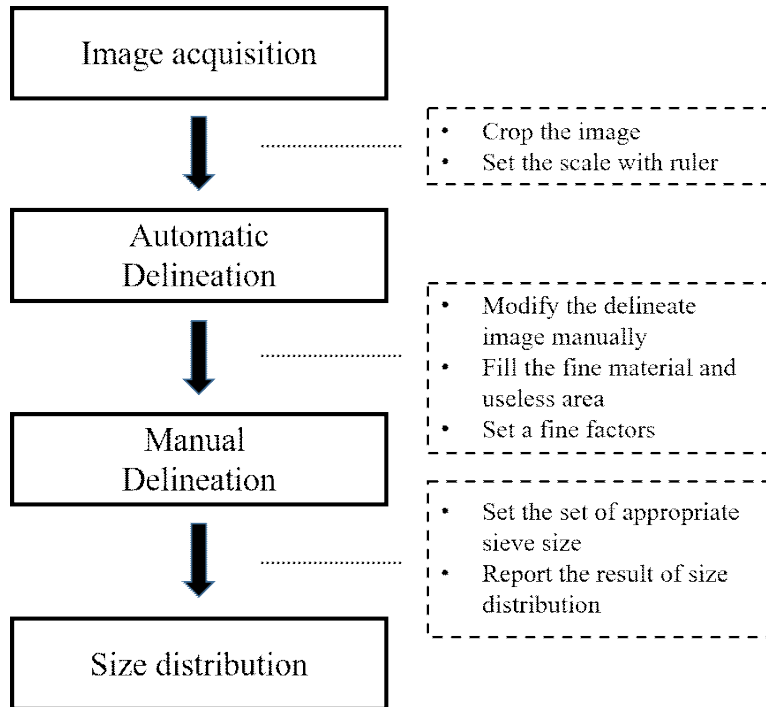
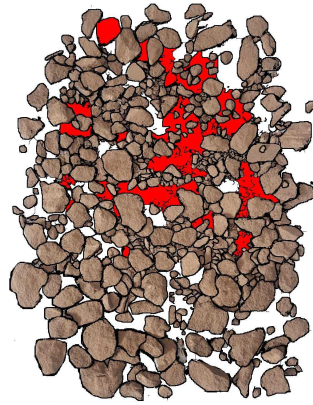


Figure 3.11 The process of Split-desktop for size distribution analysis

Figure 3.12 shows the typical images ($p = 5$ mm and $p = 9$ mm at the $s/p = 1$) before and after images processing in SPLIT-DESKTOP.



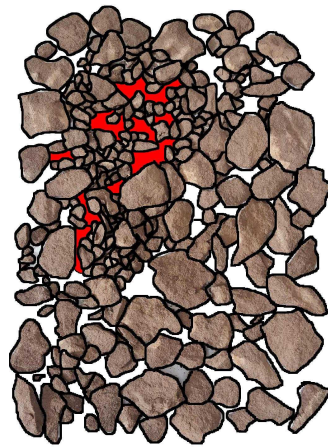
(a) Before



(b) After



(c) Before



(d) After

Figure 3.12 Rock chip images before and after image processing: (a) and (b) are for $p = 5$ mm and $s/p = 1$, and (c) and (d) are for $p = 9$ mm and $s/p = 1$

3.4.3 Sieve test

The results of size distribution from split desktop were verified by the direct sieve test, and the sieve test was used for the analysis for rock powder generation (Figure 3.12).



Figure 3.13 The direct sieving tester used in this study

4. Results of LCM test

4.1 Linyi-sandstone

The results of this chapter are for the 0° of skew angle and 45° of attack angle. The values of the angles were considered as the basic cutting condition in this study. The tests were performed to find the optimum cutting conditions for Linyi-sandstone specimen with varied penetration depth and cut spacing. The penetration depths were from 5 mm to 11 mm, s/p ratios were from 1 to 5, and cut spacing was determined by penetration depth and s/p ratio. The cutter forces were only considered for the relieved cut mode. The test results summarized in Table 4.1.

Table 4.1 The testing conditions and the results for the Linyi sandstone

Rock type	p (mm)	s (mm)	s/p	Attack angle (α)	Skew angle (θ)	Mean cutter force, F_{mean} (kN)			Peak cutter force, F_{peak} (kN)			Specific energy (MJ/m ³)	
						Side	Cutting	Normal	Side	Cutting	Normal	M*	C*
Linyi sandstone	5	5	1	45	0	0.81	3.21	3.61	1.21	7.64	8.95	82.96	131.4
		10	2			0.13	4.25	4.38	1.33	10.08	10.12	77.65	8.67
		15	3			0.17	5.21	5.29	0.62	13.24	13.32	77.86	8.86
		20	4			0.53	5.81	5.87	1.59	12.99	13.54	67.57	7.41
		25	5			0.27	6.35	6.43	1.47	14.95	15.93	8.58	6.48
	7	7	1			0.47	3.48	3.51	1.08	1.71	8.46	5.47	9.06
		14	2			0.54	5.08	5.13	1.52	2.26	11.58	4.89	6.62
		21	3			0.61	6.07	6.84	1.51	2.35	12.80	4.22	5.03
		28	4			0.84	6.96	7.25	1.42	3.03	17.03	4.49	4.53
	9	9	1			0.60	5.02	5.65	1.57	12.13	12.17	49.73	75.91
		13.5	1.5			0.51	6.15	7.20	1.65	14.95	16.90	45.66	60.23
		18	2			0.52	6.63	7.96	1.83	19.20	19.54	37.69	52.22
		22.5	2.5			0.38	8.29	9.18	1.20	20.41	21.17	36.50	55.73
		27	3			0.52	7.59	9.40	1.67	19.61	20.99	33.12	42.50
		36	4			0.78	8.30	10.95	1.83	21.92	23.34	39.70	39.22
	11	11	1			0.26	6.97	7.29	0.86	16.06	17.20	46.30	78.41
		22	2			0.63	7.93	8.39	1.87	16.13	17.16	34.39	44.61
		33	3			1.27	8.90	9.64	2.14	22.70	26.14	31.10	33.37
		44	4			1.30	10.02	12.96	2.38	24.91	27.88	32.71	31.68

* The “M” and “C” specific energies means “measured specific energy” and “calculated specific energy”, and were calculated using the cut rock volume obtained from weighing method and simple calculation method, respectively.

4.1.1 Cutter forces

Figure 4.1 shows the representative three orthogonal cutter forces (i.e., cutting, normal and side forces) obtained from the LCM test. The peak cutter forces are the maximum values of the forces, and the mean cutter forces are the average values of the forces obtained during the tests. The side force was oscillating around zero and significantly small compared with other forces because the skew angle was set as 0° . In this study, it was not considered that the side forces did not affect the cutting performance when the skew angle was set as 0° .

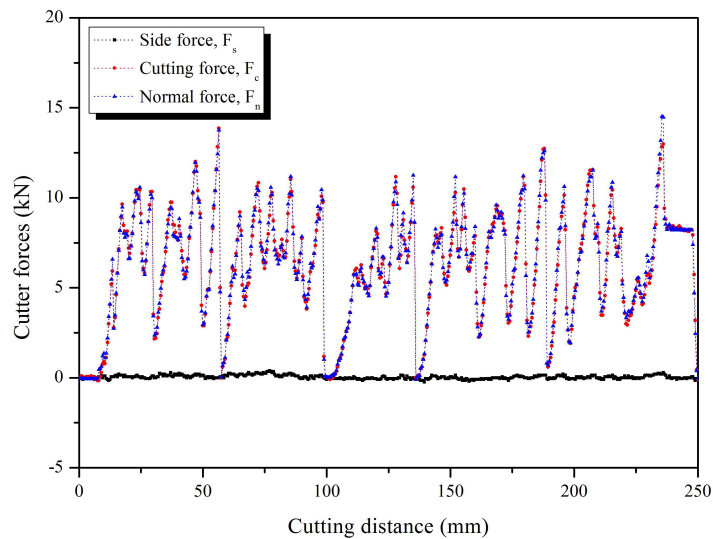


Figure 4.1 The representative cutter forces obtained from LCM test

Figure 4.2 shows the relationship between the mean cutter forces and s/p ratio. Some data for 5 mm and 9 mm of penetration depths were omitted

for graph plotting. The mean cutting force linearly increased with cut spacing for all penetration depths, and the cutting forces increased with the penetration depth.

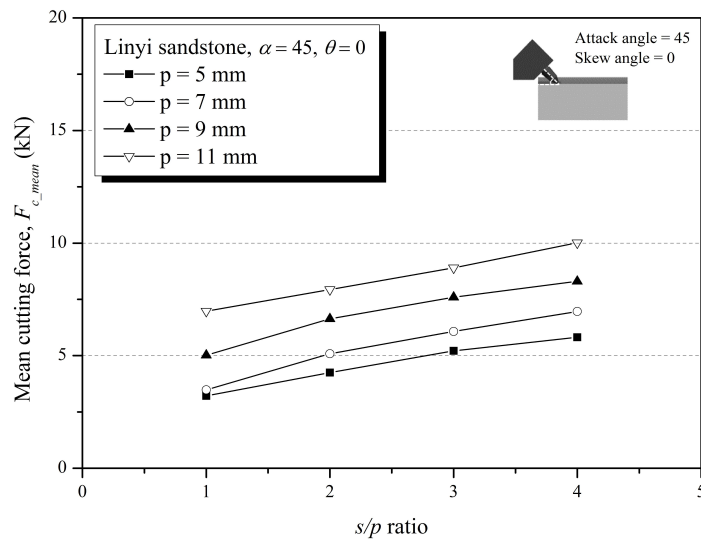


Figure 4.2 Effect of s/p ratio on the mean cutting force (Linyi sandstone, $\alpha = 45^\circ$ and $\theta = 0^\circ$)

Figure 4.3 shows the relationship between the mean normal forces and s/p ratio. The mean normal force also linearly increased with cut spacing for all penetration depths, and the normal forces also increased with the penetration depth.

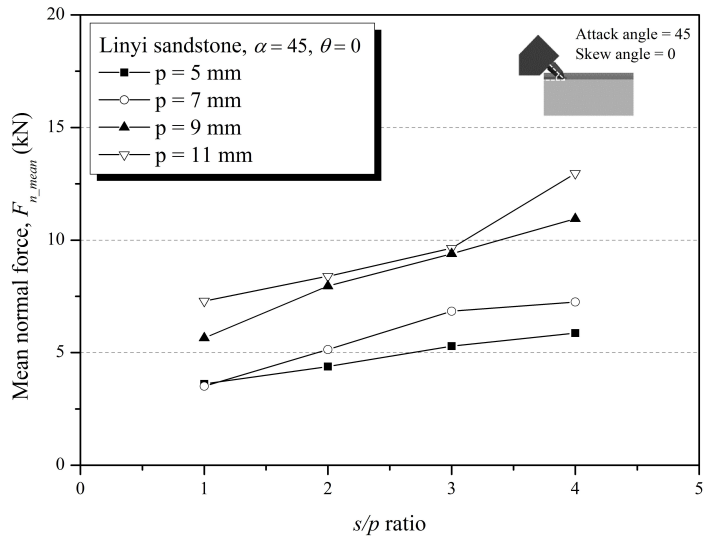


Figure 4.3 Effect of the s/p ratio on the mean normal force
(Linyi-sandstone, $\alpha = 45^\circ$ and $\theta = 0^\circ$)

Figure 4.4 shows the effect of the s/p ratio on the force index (FI) for the mean cutter forces for all penetration depth. The results show that the effect of the cut spacing (expressed by s/p ratio) on the cutter force is independent of the penetration depth, and the linear relationship between the normal force and cutting force and s/p ratio. While the side force is not influenced by the cut spacing.

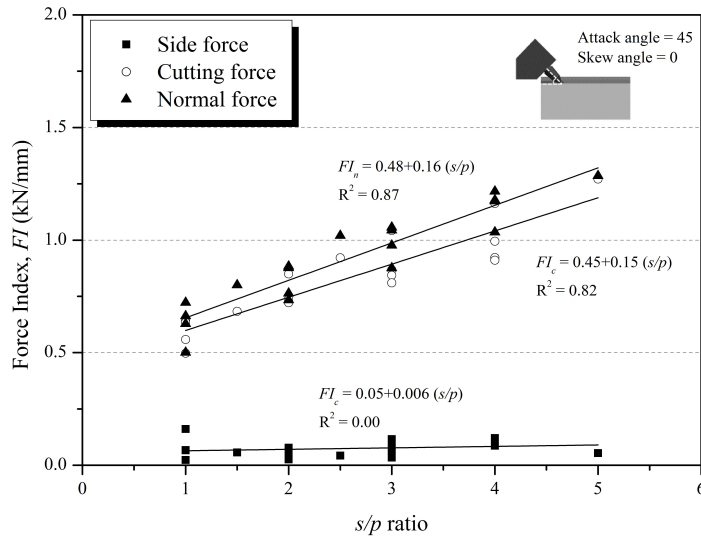


Figure 4.4 Effect of the s/p ratio on the force index (Linyi-sandstone, $\alpha = 45^\circ$ and $\theta = 0^\circ$)

The ratio of peak to mean cutter force is considered important to assess the vibration of the cutterhead and the damage of the machine during rock excavation. Also, the ratio can be used to estimate the mean force of the pick cutter from the peak cutting force which is calculated by the theoretical model. From the previous researches on LCM test (Bilgin et al., 2006; Choi et al., 2014), it was noted that the ratio was found to be around three to four. However, figure 4.5 shows that the relationship between peak cutter force and mean cutter force of the Linyi sandstone, and it was found to be around two in this study.

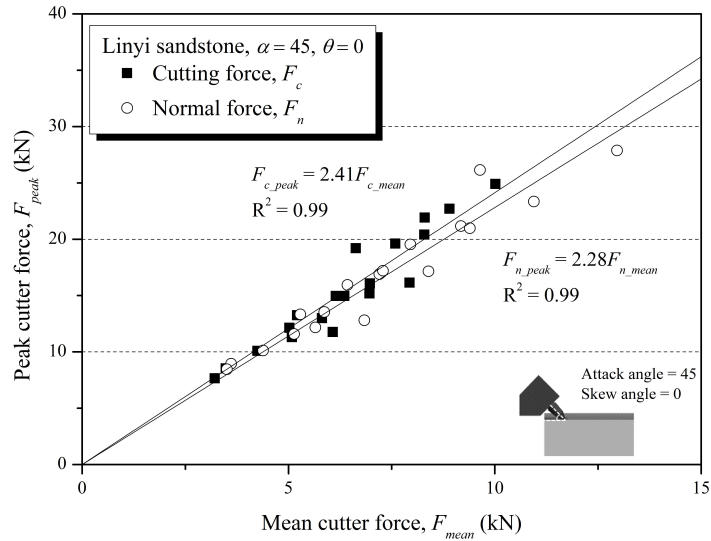


Figure 4.5 The relationship between the peak cutter force and mean cutter force (Linyi-sandstone, $\alpha = 45^\circ$ and $\theta = 0^\circ$)

Figure 4.6 shows the ratios of the cutting force to the normal force in different cutting conditions. The ratio can be used to estimate the normal force of the pick cutter from the cutting force which is calculated by theoretical model. So, it is practically important design parameter to estimate the cutter forces and machine's specifications. The ratios for peak and mean forces were found to be around one for all cutting conditions. The ratio is affected by the coefficient of friction with the rock, the shape of the pick cutter, and the angle of the cutter tip, also, the ratio is physically related to the attack angle of a pick cutter; when the attack angle was set as 45° , the direction of the resultant force is 45° . Thus it is physically natural phenomenon that the normal force and cutting force are almost equal.

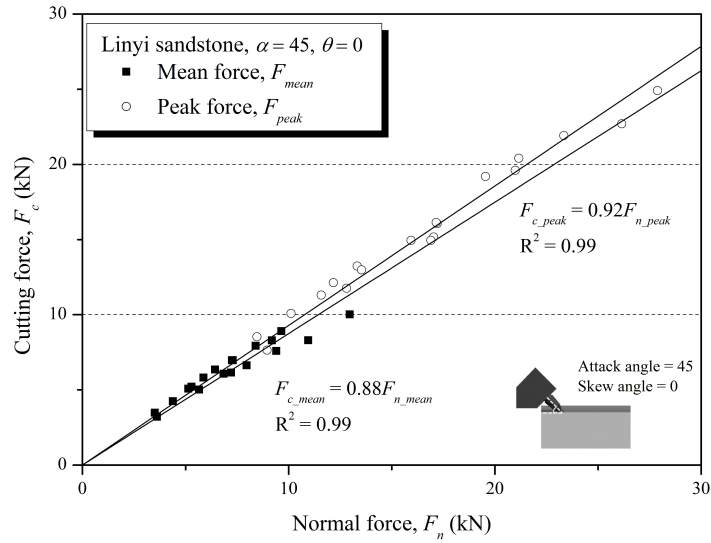


Figure 4.6 The cutting coefficients for the mean and peak forces
(Linyi-sandstone, $\alpha = 45^\circ$ and $\theta = 0^\circ$)

4.1.2 Specific energy

Figure 4.7 shows the relationship between the cut spacing and the specific energy. The optimum cutting condition is defined as the s/p ratio at the minimum specific energy. The optimum s/p ratios were found to be four for 5 mm of penetration depth and three for other penetration depths. The optimum cut spacing is increasing, and the corresponding to the optimum s/p ratio is decreasing with penetration depth.

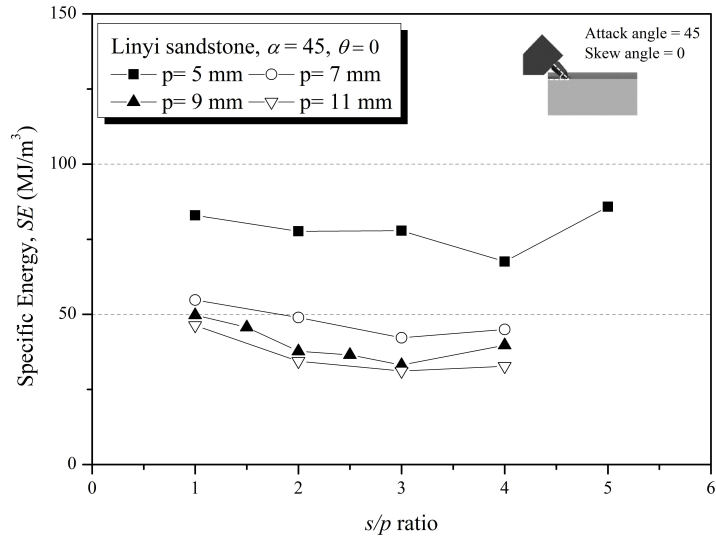


Figure 4.7 The relationship between s/p ratio and specific energy (Linyi-sandstone, $\alpha = 45^\circ$ and $\theta = 0^\circ$)

Figure 4.8 shows the relationship between the penetration depth and the specific energy at the optimum cut spacing. The specific energy at the optimum cutting condition was decreasing in exponential form with penetration depth which ranges from 5 mm to 11 mm. Although the range of considered penetration depth was limited, the result means that for greater penetration depth, smaller s/p ratio needs to be applied for efficient cutting. Also, the results show that the specific energy decreased with increasing of penetration depth. Thus, it is noted that machine operation is optimized at large penetration depth per revolution (per cutting pass for each cutter) with considering the machine capacity (i.e., thrust and torque). Some previous study (Chang et al., 2006; Cho, 2010) reported concept of the “*optimum*

penetration depth” that was defined at the specific penetration depth having a minimum (or converged) specific energy. In this study, the optimum penetration depth is not clearly defined since the lack of the tested data at the larger penetration depth, but it is considered that the optimum penetration depth will be found at the penetration depth of 11 mm or more, based on the trend line.

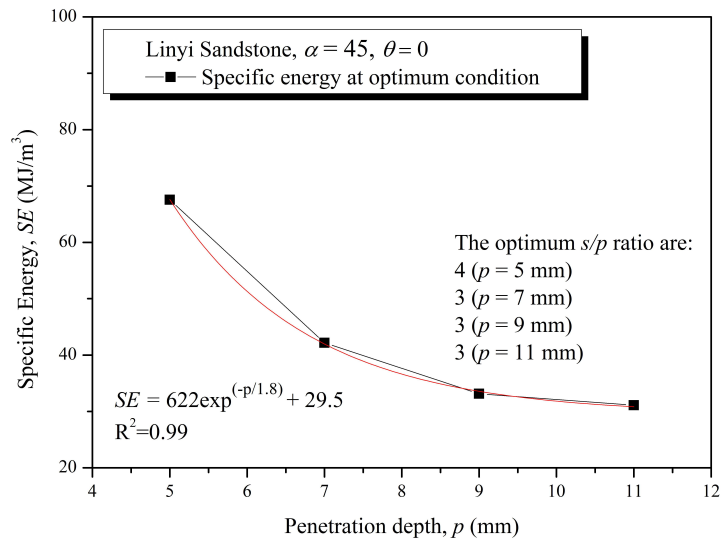


Figure 4.8 The relationship between penetration depth and specific energy at the optimum cutting condition (Linyi-sandstone, $\alpha = 45^\circ$ and $\theta = 0^\circ$)

Figure 4.9 shows the difference between the two specific energies according to the method for calculation of the cut volume. The cut volume was obtained from two methods in this study. The ‘measured specific energy’ was calculated using weighing the rock debris, and the ‘calculated

specific energy' was from the approximation method. Also, the calculated specific energy was overestimated when cut spacing was narrow, while it was underestimated when cut spacing was wide compared with the measured specific energy. Because the calculated specific energy continuously decreased with the increase of the cut spacing The difference has been reported by the several studies (Cho et al., 2010; Jeong, 2010; Cho et al., 2013), thus optimum s/p ratio was not found using the simple calculation method. The results show that it is important to measure excavated rock volume accurately in rock cutting test.

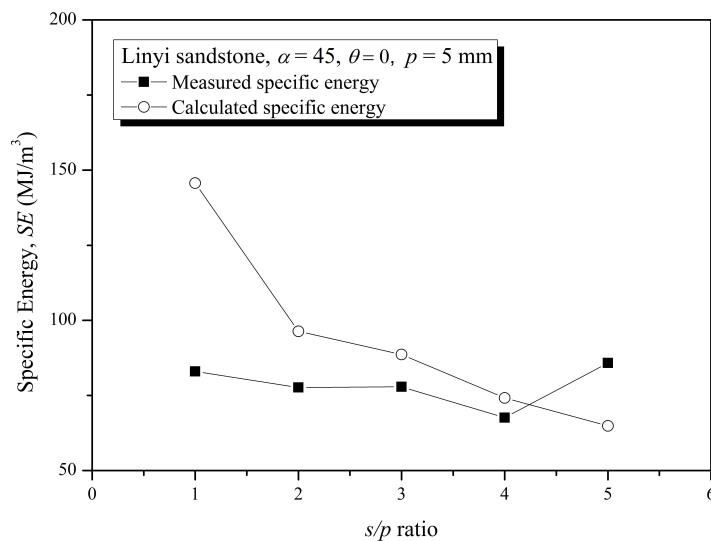


Figure 4.9 The relationship between penetration depth and specific energy at the optimum cutting condition (Linyi-sandstone, $\alpha = 45^\circ$ and $\theta = 0^\circ$ at $p = 5$ mm)

4.2 Concrete

The results of this chapter are also for the 0° of skew angle and 45° of attack angle. The testing angles were considered as the general cutting condition in this study. The tests were performed to find the optimum cutting conditions for the concrete specimen with different penetration depth and cut spacing. The penetration depths were from 5 mm, 7 mm, 9 mm, and 11 mm, and the cut spacing were fixed from 15 mm to 35 mm. The s/p ratio was determined by given penetration depth and cut spacing. The cutter forces were only considered for the relieved cut mode. Finally, these results used for application to design the chain type of trenching cutter. The testing conditions and the results were listed in Table 4.2. Figure 4.10 showed the concrete specimen and cut surface after cutting tests.

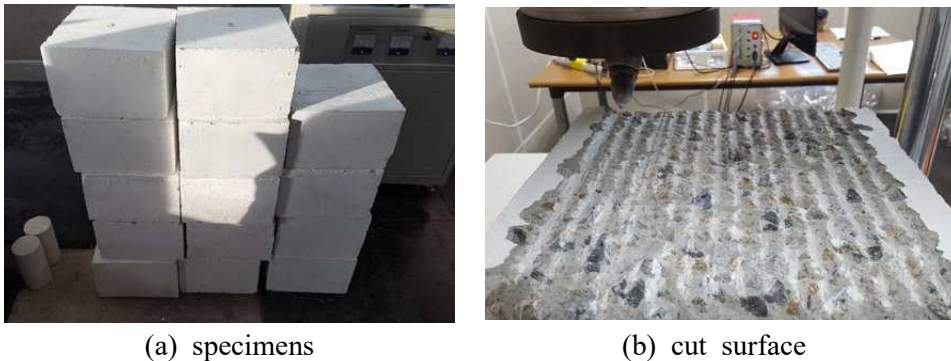


Figure 4.10 The concrete specimens used in this study: (a) concrete blocks and (b) cut surface

Table 4.2 The testing conditions and the results for the concrete specimen

Rock type	p (mm)	s (mm)	Attack angle (α)	Skew angle (θ)	Mean cutter force, F_{mean} (kN)			Peak cutter force, F_{peak} (kN)			Specific Energy (MJ/m ³)	
					Side	Cutting	Normal	Side	Cutting	Normal	M*	C*
Concrete	5	15	45	0	1.27	2.55	1.74	3.43	7.40	0.58	31.88	27.80
	5	20			0.78	2.82	1.93	2.23	9.65	0.71	29.43	28.77
	5	25			1.21	3.28	2.59	3.54	13.35	1.03	33.69	35.93
	5	30			1.54	3.80	2.85	4.00	10.99	0.82	37.07	38.76
	5	35			0.99	3.85	2.72	2.70	12.99	0.92	40.62	39.26
	7	15			1.35	3.18	2.00	4.44	13.12	0.90	31.48	23.81
	7	20			0.96	3.21	2.29	2.94	11.64	0.91	27.03	25.49
	7	25			1.29	3.92	3.82	4.60	14.01	1.03	26.03	30.99
	7	30			1.36	4.49	4.02	3.85	13.26	1.09	26.75	37.37
	7	35			2.13	5.16	4.31	5.83	17.87	1.33	33.01	44.80
	9	15			1.10	4.19	2.87	3.26	14.03	0.96	29.38	35.16
	9	20			1.38	4.36	3.61	3.72	15.54	1.13	27.75	28.80
	9	25			1.53	4.72	4.12	5.15	18.94	1.50	23.79	25.71
	9	30			1.55	6.63	4.27	5.77	19.30	1.34	25.37	31.34
	9	35			1.44	7.37	4.80	4.08	23.72	1.57	30.64	31.85
	11	15			0.90	4.92	3.50	2.32	17.84	1.33	28.91	36.52
	11	20			1.27	5.77	4.26	2.56	18.48	1.43	25.72	32.14
	11	25			1.41	5.99	4.76	3.01	21.04	1.83	22.53	27.80
	11	30			1.35	7.61	5.64	4.79	22.32	1.92	22.99	29.43
	11	35			1.44	8.84	7.71	5.06	27.88	2.22	23.29	31.25

* The "M" and "C" specific energies means "measured specific energy" and "calculated specific energy", and were calculated using the cut rock volume obtained from weighing method and simple calculation method, respectively.

4.2.1 Cutter forces

Figure 4.11 shows the relationship between the mean cutting forces and penetration depth where the cut spacings were 15, 20, 25, 30, and 35 mm. The mean cutting force linearly increased with penetration depth for all cut spacings.

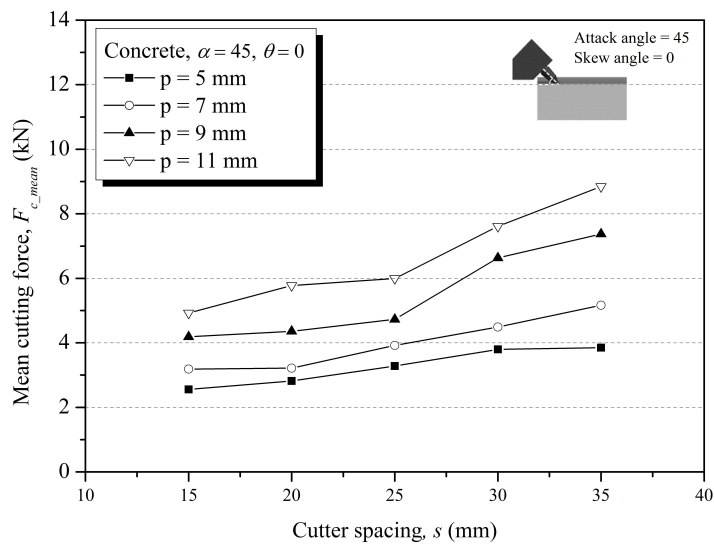


Figure 4.11 The effect of the penetration depth and the cut spacing on the mean normal force (Concrete, $\alpha = 45^\circ$ and $\theta = 0^\circ$)

Figure 4.12 shows the relationship between the mean normal forces and s/p ratio. The mean normal force also increased with cut spacing for all penetration depths, and the normal forces also increased with the penetration depth.

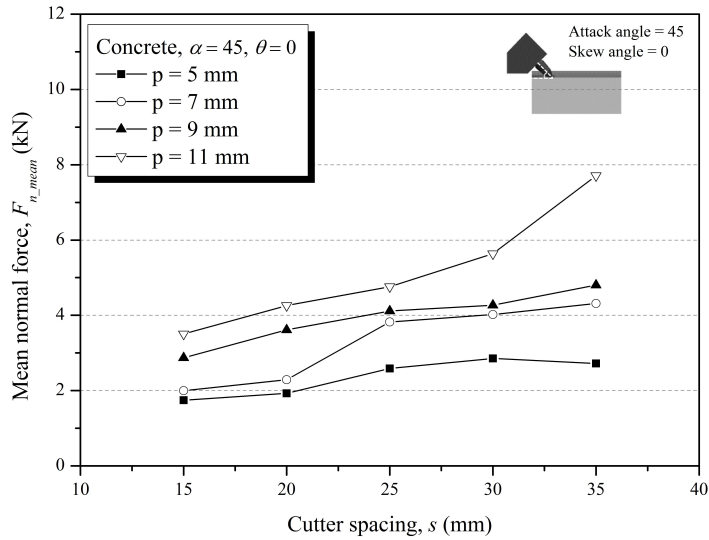


Figure 4.12 The effect of the penetration depth and the cut spacing on the mean normal force (Concrete, $\alpha = 45^\circ$ and $\theta = 0^\circ$)

Figure 4.13 shows the effect of the s/p ratio on the force index (FI) for the mean cutter forces for all penetration depth in concrete. As shown in the result of Linyi sandstone (figure 4.4), it is confirmed that the effect of the cut spacing on the cutter force is independent of the penetration depth, and the linear relationship between the normal force and cutting force and the cut spacing. While the side force is not influenced by the cut spacing.

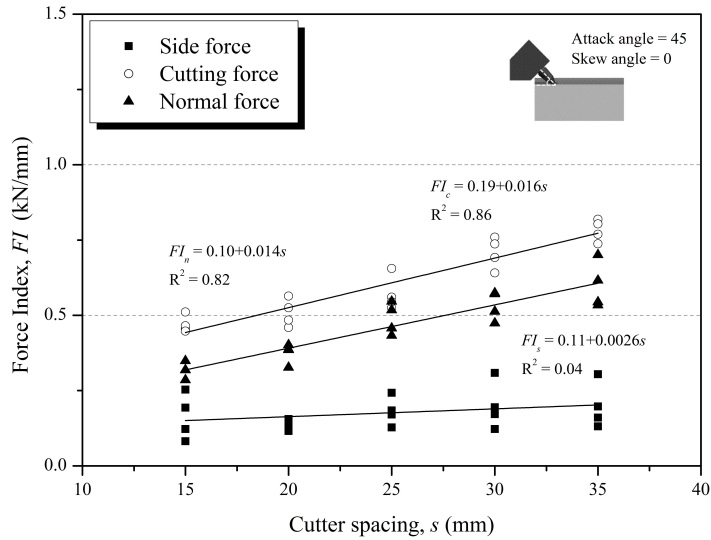


Figure 4.13 Effect of the cut spacing on the force index (Concrete, $\alpha = 45^\circ$ and $\theta = 0^\circ$)

Figure 4.14 shows the ratio of the peak cutter forces to the mean cutter forces. The ratios were found to be around 3.28 and 3.30 for the normal force and the cutting force, respectively. The ratios obtained from the concrete were larger than those of Linyi sandstone. The concrete contains aggregates (maximum size is 25 mm) that are difficult to cut (or not cuttable), and its distribution is heterogeneous, while Linyi-sandstone is composed of relatively easy-to-cut materials and is homogeneous. Moreover, considering the difference in strength of the two specimens, this result indicates that the ratio is dominantly influenced by the composition of the rock and the fragmentation behavior (brittle/ductile) of the rock, rather than the strength of the rock. It is supported by the results of the previous study

(Bilgin et al., 2006), it can be found that the ratio varies in the range of 2.0 to 4.5 according to the rock type, and it is not influenced by the strength of the rock.

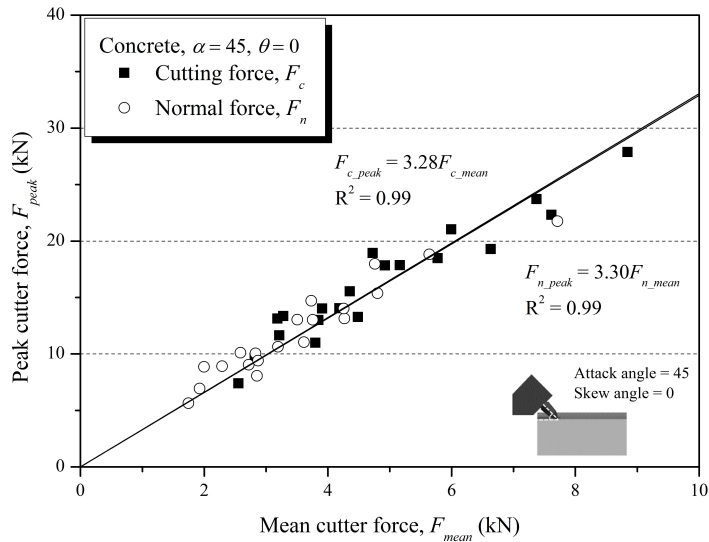


Figure 4.14 The relationship between the peak cutter force and mean cutter force (Linyi-sandstone, $\alpha = 45^\circ$ and $\theta = 0^\circ$)

Moreover, the cutting (or fragmentation) characteristic (brittle or ductile) of rock in cutting and indentation process was discussed by several studies using the LCM test and the punch penetration test (Copur 1999; Copur 2003; Yagiz 2002; Yagiz 2009; Jeong 2010; Jeong et al., 2016). The studies indicate that the behavior of rock under loading is comparatively more brittle, it shows relatively more fluctuated response in acting force due to chipping, while less fluctuation for more ductile rocks (Copur, 2003; Jeong, 2010).

And they concluded that the force-penetration response also can be affected by the micro (i.e., texture, grain geometry, and matrix material) and macro (i.e., strength and elastic modulus) properties of rocks, geometry of cutting tools, the environmental parameters (i.e., type of loading, confinement, and temperature). Because of the environmental parameters and cutting tools are constant variables in this study, the characteristic of rock and the mechanical properties of rock make the difference of the ratio of the peak cutter force to mean cutter force between Linyi sandstone and concrete.

If the machine and the components of the machine have the sufficient stiffness to endure the vibration of the cutter forces corresponding to the ratio of the peak cutter force to the mean cutter force, then the problems due to the vibrations of the cutter forces can be minimized. While, if their stiffness is not sufficient to endure the vibration, then the cutting efficiency and performance can be reduced. To optimize the machine's performance, the stiffness of the machine and components should be sufficient to endure the vibration corresponding to the ratio.

On the other hand, figure 4.15 shows the cutting coefficients in different cutting conditions. They were found to be 1.33 for all cutting conditions on average, and the resultant angle is found to be $32 \sim 41^\circ$. Comparing with the result of Linyi sandstone in same cutting angles, the resultant angles were found to be $45 \sim 52^\circ$. This means that the resultant angle can vary depending on the characteristics of the rock although the same attack angle is applied, and it independent the cut spacing and penetration depth; thus, it is necessary to carry out the cutting test with given rock type and attack

angle to estimate the accurate resultant angle.

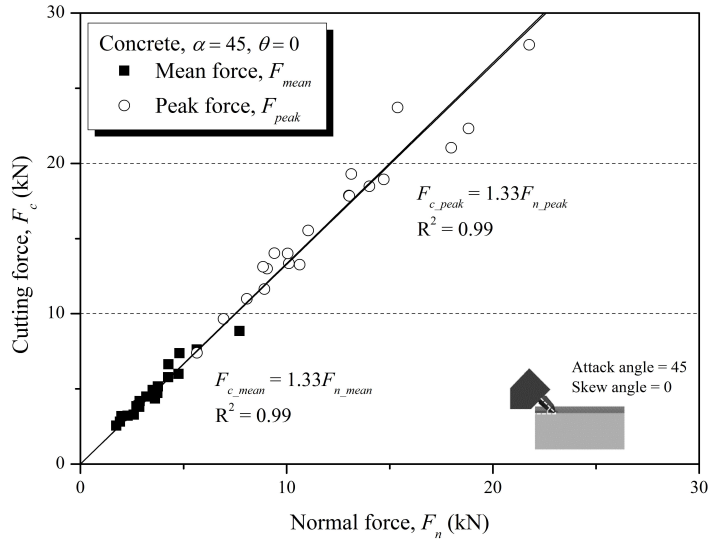


Figure 4.15 The relationship between the cutting force and normal force (Concrete, $\alpha = 45^\circ$ and $\theta = 0^\circ$)

Figure 4.16 shows the relationship between the direction of the resultant force and the attack angle in Linyi sandstone and concrete. The attack angle and direction of the resultant force are matched well for the Linyi sandstone, while in the case of concrete, attack angle and direction of resultant force are not matched well. For Linyi sandstone, 45° of the attack angle provides the mechanical stability, and it can be the optimum attack angle because the bending force is minimized. While the angle is not preferable for the concrete due to the mechanical stability.

As the difference between the two specimens, the direction of resultant force (or the ratio of the cutting force to the normal force) can be affected

by the dynamic friction coefficient between the pick cutter and the rock. Therefore, contact area between the pick cutter and rock, the roughness of rock surface, and the composition of rock are the influencing parameters to the direction of the resultant force.

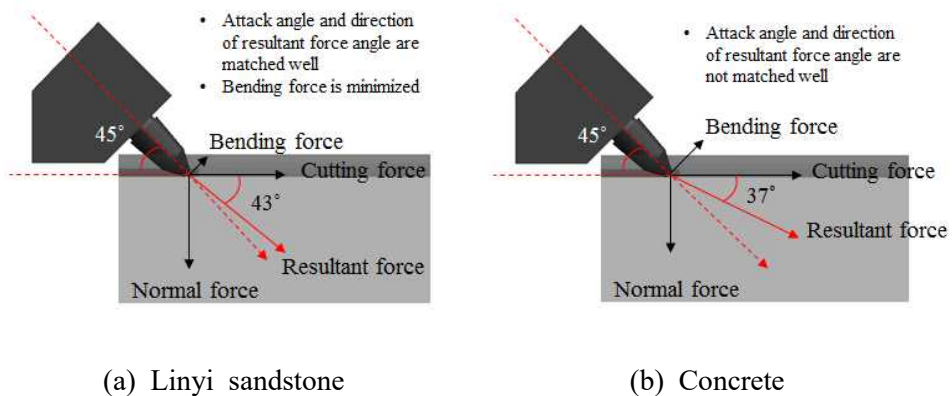


Figure 4.16 The bending force according to the skew angle and direction of resultant force

4.2.2 Specific energy

Figure 4.17 shows the effect of the cut spacing on the specific energy for the concrete specimen. The optimum cut spacings of given penetration depths can be found at 20 mm, 20 - 25 mm, 25 - 30 mm and 25 - 35 mm, corresponded s/p ratios were 4, 2.86 - 4.29, 2.78 - 3.33 and 2.27 - 3.18. In the case of 11 mm penetration depth, it tended to converge from the 25 mm until 35 mm. The results mean that the optimum s/p ratio can be decreased as the penetration depth increases rather than it is an absolute value for given rock type.

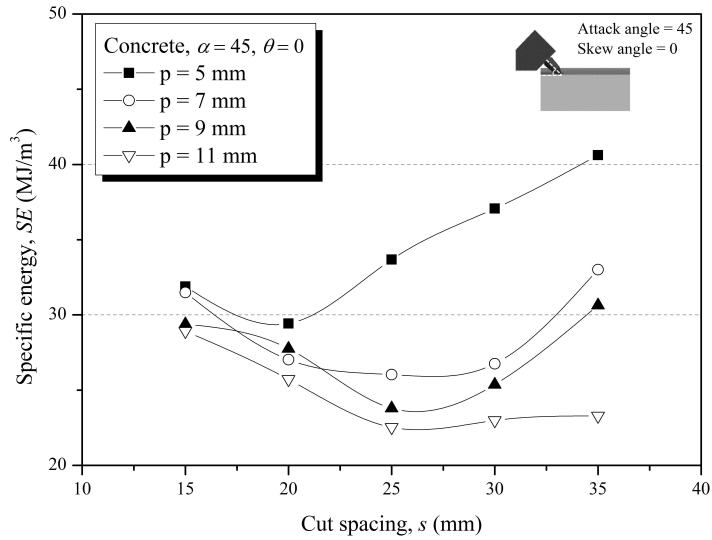


Figure 4.17 The effect of cut spacing on the specific energy and optimum cut spacing at the different penetration depth (Concrete, $\alpha = 45^\circ$ and $\theta = 0^\circ$)

Figure 4.18 shows the effect of the penetration depth on the specific energy. The specific energy linearly decreased with increasing of the penetration depth. The results of specific energy are the same with that of Linyi sandstone (Figure 4.7).

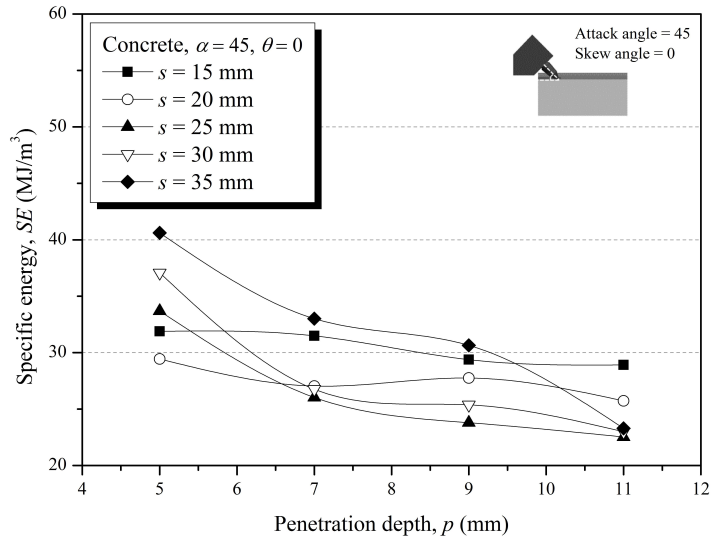


Figure 4.18 The effect of the penetration on the specific energy at different cut spacing (Concrete, $\alpha = 45^\circ$ and $\theta = 0^\circ$)

Based on the figures 4.17 and 4.18, the range of 20 mm - 30 mm of cut spacing can be considered as the optimum cut spacing for the concrete specimen with the given range of penetration depths. The 20 mm of cut spacing is optimum cutting condition for the 5 mm of penetration depth, whereas the cutter spacing of 25 mm and 30 mm are the optimum cutting condition that minimizes specific energy at penetration depths of 7 mm or more.

4.3 Effect of skew angle

4.3.1 Testing conditions

The skew angle is defined by the angle between the cutting direction and the central axis of a pick. The skew angle is generally adopted to pick cutter as the pick cutter is arranged on the cutting head of the mechanical excavator such as roadheader and trenching cutter. It is important to determine the optimum skew angle and the effect of the skew angle on the cutting performance of a pick cutter.

This study conducted a linear cutting test on various skew angles to investigate the effect of skew angle on the cutting performance of the pick cutter and find an optimum skew angle for the different penetration depths. The cutting conditions and results of LCM tests are summarized in Table 4.3 and Table 4.4, respectively.

Table 4.3 LCM test conditions to analyze the effect of the skew angle on the optimum cutting conditions

Rock type	p (mm)	s (mm)	Attack angle, α (degree)	Skew angle, θ (degree)
Linyi sandstone	5	20	45	0
				-5
	7	21		+5
				-10
	9	27		+10
				-15
	11	33		+15
				-20
				+20
				0
Concrete	7	21	45	-5
				+5
	7	21		-10
				+10
	7	21		-15
				+15
	7	21		-20
				+20
				0
				-5

Table 4.4 The testing conditions and the results of the linear cutting test with different skew angles

Rock type	p (mm)	s (mm)	Attack angle (α)	Skew angle (θ)	Mean cutter force, F_{mean} (kN)			Peak cutter force, F_{peak} (kN)			Specific Energy* (MJ/m ³)	
					Side	Cutting	Normal	Side	Cutting	Normal	M	C
Linyi sandstone	5	20	45	0	0.53	5.81	5.87	1.59	12.99	13.54	67.57	74.15
				-5	0.92	6.98	5.27	1.69	15.09	12.61	69.46	83.13
				+5	0.86	6.57	4.72	1.59	16.79	13.75	74.58	76.63
				-10	1.48	8.47	5.74	2.33	16.86	11.79	72.04	108.01
				+10	1.76	8.23	5.56	2.92	17.68	11.78	93.05	106.07
				-15	1.57	6.08	4.09	4.13	17.33	14.49	67.65	70.91
				+15	1.87	6.09	4.49	5.04	18.49	14.69	65.90	69.93
				-20	4.22	5.26	4.84	13.86	15.05	16.28	56.29	62.60
				+20	3.68	4.81	4.68	14.50	18.63	14.90	41.40	56.06
				0	0.61	6.07	6.84	1.51	11.76	12.80	42.17	50.29
	7	21	45	-5	1.33	8.63	5.88	2.51	23.91	19.35	62.90	71.85
				+5	1.00	8.26	6.24	2.78	27.00	22.35	59.26	68.82
				-10	1.76	8.31	6.27	3.41	21.94	14.65	62.47	69.21
				+10	1.70	9.18	6.47	2.96	20.31	13.73	75.51	76.44
				-15	1.43	7.35	5.71	3.42	21.50	18.21	58.59	59.57
				+15	2.17	6.96	5.22	6.82	19.50	15.19	46.44	55.23
				-20	5.15	5.65	5.82	15.66	16.43	21.55	38.34	45.72
				+20	4.70	5.99	6.34	13.10	17.74	19.99	37.59	49.87

Table 4.4 (Continued)

Rock type	p (mm)	s (mm)	Attack angle (α)	Skew angle (θ)	Mean cutter force, F_{mean} (kN)			Peak cutter force, F_{peak} (kN)			Specific Energy* (MJ/m ³)	
					Side	Cutting	Normal	Side	Cutting	Normal	M	C
Linyi sandstone	9	27	45	0	0.52	7.59	9.40	1.67	19.61	20.99	36.10	42.50
				-5	1.28	9.34	6.84	2.70	25.52	20.85	42.82	44.84
				+5	1.60	8.51	6.78	4.04	26.62	22.27	38.51	40.84
				-10	2.08	10.74	8.40	5.26	26.84	21.31	46.56	60.11
				+10	1.98	11.30	8.41	5.21	27.83	18.96	44.16	71.18
				-15	1.88	9.21	7.51	4.27	25.04	20.83	42.17	48.33
				+15	1.64	9.31	7.49	6.01	21.89	18.07	42.68	48.86
				-20	6.58	7.54	8.71	16.49	21.08	26.48	33.02	42.23
				+20	2.80	4.23	4.48	10.41	13.61	16.03	17.61	21.32
	11	33	45	0	1.15	9.54	10.20	2.05	23.98	27.90	31.10	33.37
				-5	1.52	9.73	7.69	3.61	30.23	26.26	47.87	32.81
				+5	1.15	9.45	9.52	3.55	27.83	26.93	37.84	31.88
				-10	2.03	11.71	8.14	4.48	26.26	20.57	35.56	49.39
				+10	2.09	10.97	8.27	3.90	25.86	18.32	41.39	46.26
				-15	2.05	11.30	8.33	6.41	31.91	27.51	37.90	42.36
				+15	2.35	12.20	8.05	8.53	29.57	22.76	35.87	45.73
				-20	4.18	4.65	6.90	15.07	18.25	27.54	12.42	17.44
				+20	4.40	5.60	6.25	13.82	20.42	24.10	18.38	21.00

*“M” indicates the measured specific energy from the weighing method, and “C” indicates the calculated specific energy from the simple calculation method.

Table 4.4 (Continued)

Rock type	p (mm)	s (mm)	Attack angle (α)	Skew angle (θ)	Mean cutter force, F_{mean} (kN)			Peak cutter force, F_{peak} (kN)			Specific Energy* (MJ/m ³)	
					Side	Cutting	Normal	Side	Cutting	Normal	M	C
Concrete	7	25	45	0	0.49	3.91	3.82	2.07	14.01	13.03	26.03	29.69
				-5	1.47	4.19	3.73	3.50	14.72	12.40	28.91	36.40
				+5	1.76	4.09	3.54	2.42	13.09	10.90	27.60	35.48
				-10	2.10	4.41	3.93	4.22	13.19	13.87	27.29	35.98
				+10	1.77	4.31	3.63	4.08	12.23	12.91	27.98	34.21
				-15	2.16	4.16	3.37	5.21	15.68	16.90	27.30	33.28
				+15	2.25	4.70	2.51	4.40	16.70	12.31	25.65	35.21
				-20	2.99	4.51	3.20	9.25	16.89	13.48	27.55	34.61
				+20	3.63	4.02	2.55	8.89	17.35	11.68	22.79	33.46

*“M” indicates the measured specific energy from the weighing method, and “C” indicates the calculated specific energy from the simple calculation method.

4.3.2 Cutter forces

Figure 4.19 shows that the cutting force changes according to the skew angle at the different penetration depths (optimum cutting condition where the attack angle is 45° and skew angle is 0°), and figure 4.20 shows the cutting force normalized by that at the 0° of the skew angle.

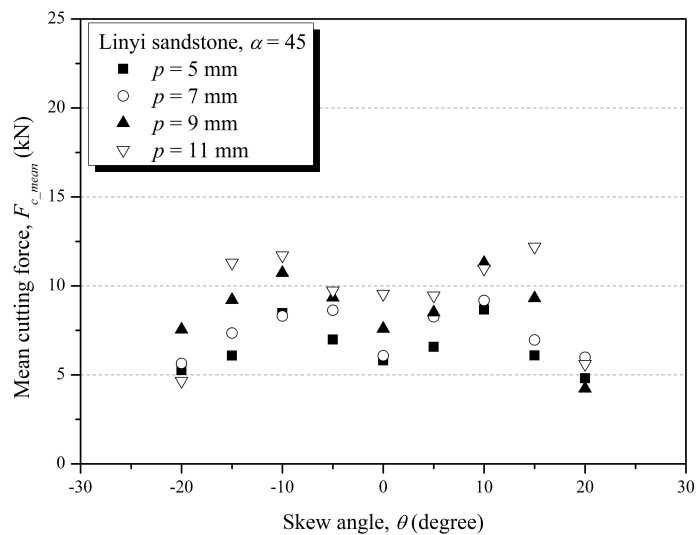


Figure 4.19 The effect of the skew angle on the mean cutting force at the different penetration depths.

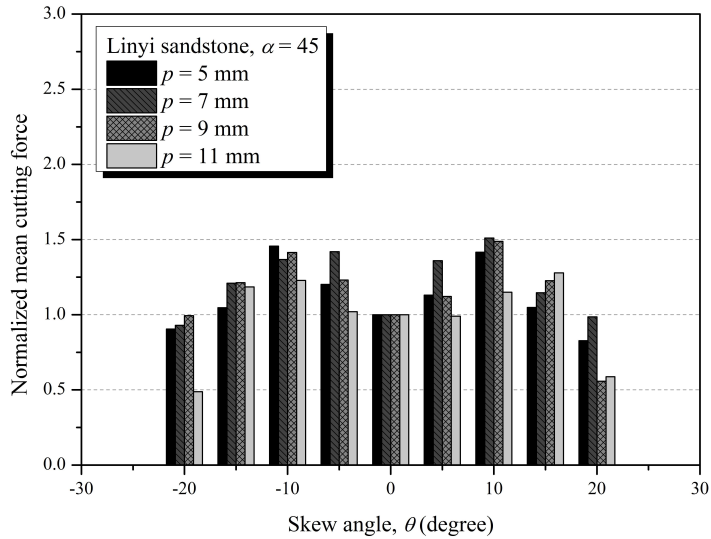


Figure 4.20 The normalized mean cutting force at the different penetration depths and skew angles.

Compared to where the skew angle is 0° , the cutting force gradually increases according to the skew angle, the force has maximum value (Normalized value = 1.14 ~ 1.51) where the skew angle is 10° , and the force where the skew angle is 15° is still larger than that of where skew angle is 0° (Normalized value = 1.04 ~ 1.27). However, at 20° of skew angle, the cutting force showed the lowest value (Normalized value = 0.48 ~ 0.98). Especially, where the penetration depth is 11 mm, the cutting force is significantly reduced compared to other penetration depths, the Normalized values of the -20° and $+20^\circ$ of skew angle were 0.48 and 0.58, respectively.

To determine the specific energy and to assess the cutting efficiency, only

the cutting force is used, it can be expected that the specific energy increases with the skew angles (from 0° to 15°) until 20° when it can be assumed that the pick cutter cut the same volume of rock in the different skew angles.

On the other hand, the normal force slightly decreases with the skew angles (Figure 4.21), and figure 4.22 shows the cutting force normalized by that at the 0° of the skew angle.

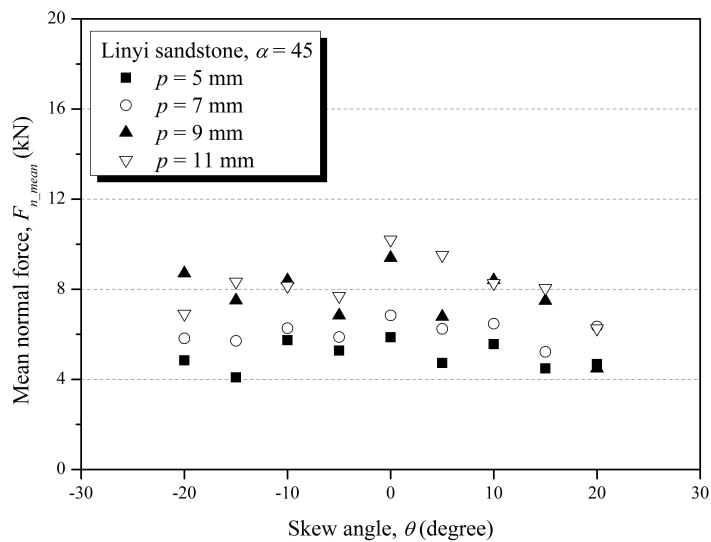


Figure 4.21 The effect of the skew angle on the mean normal force at the different penetration depths (Linyi sandstone, $\alpha = 45^\circ$).

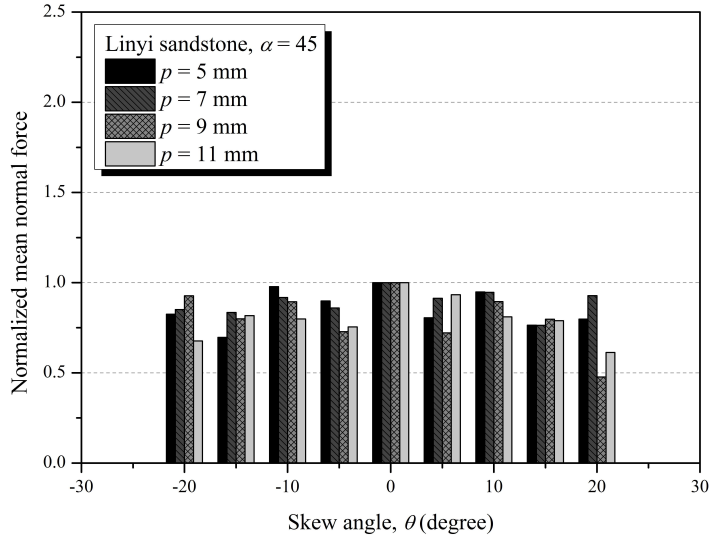


Figure 4.22 The normalized mean normal force at the different penetration depths and skew angles (Linyi sandstone, $\alpha = 45^\circ$).

Compared to where the skew angle is 0° , the normal force gradually decreases according to the skew angle, and the normal force generally had the minimum value when the skew angle was 20° . However the normal force decreases without significant trend line at some penetration depths, and it was difficult to clearly distinguish the skew angle with the lowest value of the normal force. However, compared to when the skew angle is 0° , it can be confirmed that the normal force generally decreases when the skew angle is applied.

On the other hand, the side force is significantly smaller than the other forces (Figure 4.1) where the skew angle set as 0° . From a series of LCM

test at the different skew angles in this study, the results showed that the skew angle significantly makes the side force of a pick cutter, and figure 4.23 and Figure 4.24 show the side force and the normalized side forces according to the skew angles.

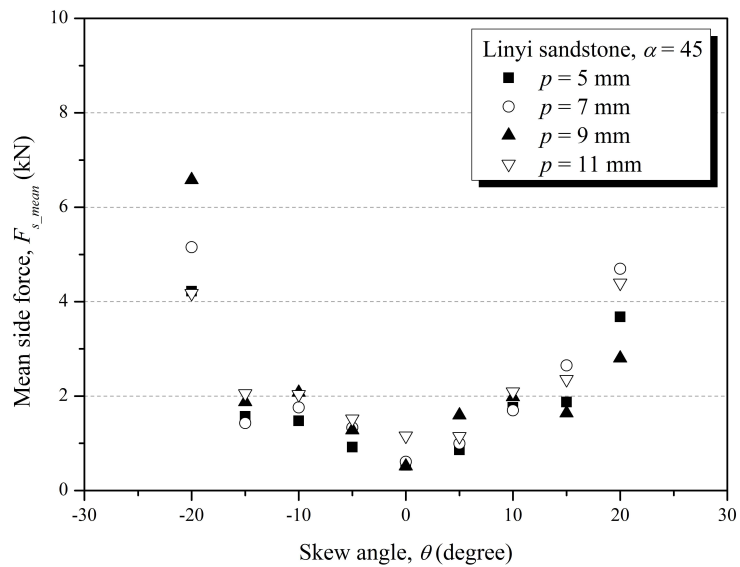


Figure 4.23 The effect of the skew angle on the mean side force at the different penetration depths (Linyi sandstone, $\alpha = 45^\circ$).

The side force steadily increased with the skew angle up to 15° , especially it drastically increased at 20° of the skew angle. Since the side force at 0° of the skew angle is close to zero, the magnitude of the normalized side force is not a significant value.

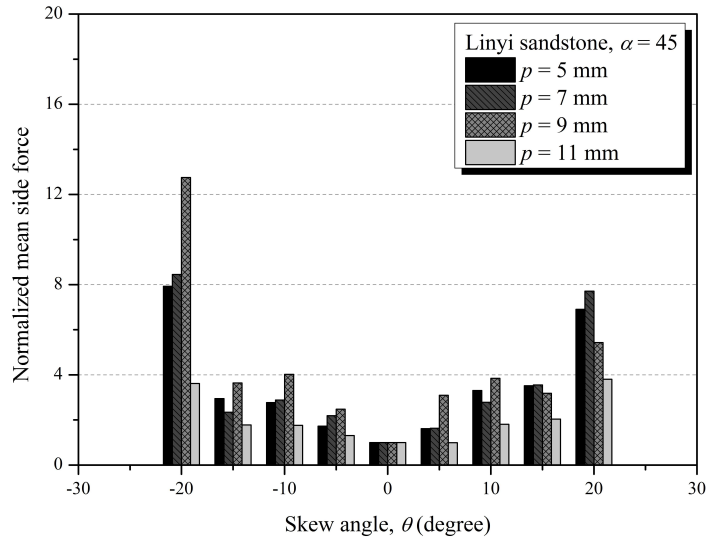


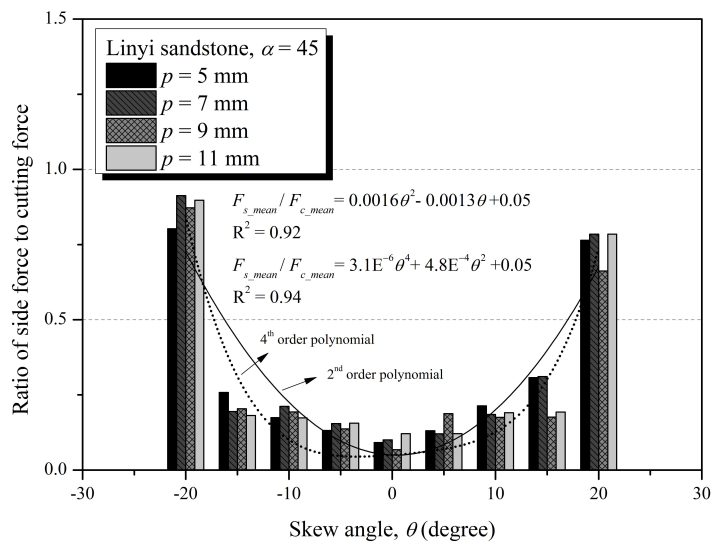
Figure 4.24 The normalized mean side force at the different penetration depths and the skew angles (Linyi sandstone, $\alpha = 45^\circ$).

The side force and the cutting force act in directions perpendicular to each other in the same plane (rock surface), and both forces are components which are orthogonal to the normal force. Therefore, the ratio of the side force to the cutting force is an important value to determine the direction of the resultant force on the cutting surface.

Figure 4.25 shows the ratio of the side force to the cutting force according to the skew angle of a pick cutter. The ratio is about 0.1 (0.07 - 0.16) on average where the skew angle is 0° , and it increased with the skew angle up to 20° . The ratios for 5° , 10° , 15° and 20° were 0.15 (0.12 - 0.19), 0.2 (0.17 - 0.21), 0.25 (0.19 - 0.31) and 0.85 (0.66 - 0.90),

respectively. Especially, it drastically increased where the skew angle was 20° and becomes the important force component which has the same level of magnitude with the cutting force. It is related to the decreasing of the cutting force. Among the three components of cutter forces, the cutting force is only considered in calculating the specific energy, and it means that the most efficient cutting condition can be obtained when the skew angle is 20° .

In practically, the side force is estimated using the side force coefficient (the ratio of the side force to the cutting or normal forces). The side force coefficient is expressed by the ratio of the side force to the cutting force in this study, and the relationship between the side force coefficient found with 2nd order and 4th order polynomial regression models.



On the other hand, it is preferable to match the skew angle and of the pick cutter with the direction of the resultant force of the pick cutter for the structural stability of the machine. Otherwise, the bending moment acts on the pick cutter and the parts connecting the pick cutter and the machine. Figure 4.26 shows the optimum skew angle and the non-optimum skew angle, respectively. If the skew angle and direction of the resultant force angle are matched well (figure 4.23 (a)), then the bending force acts on the pick cutter is minimized. While the bending force significantly acts on the pick cutter where the skew angle is not matched with the direction of the resultant force.

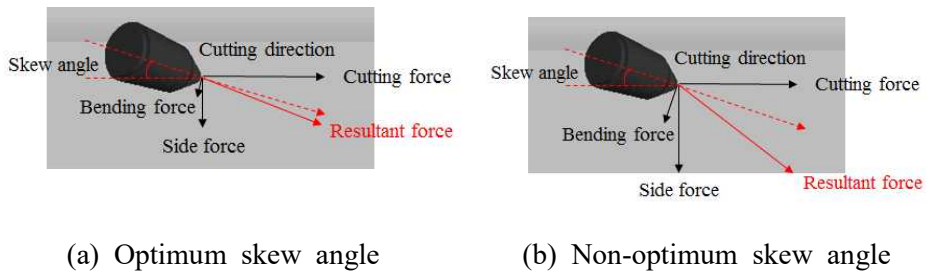


Figure 4.26 The bending force according to the skew angle and direction of resultant force

Table 4.5 presents the direction of the resultant force on the cutting surface which is obtained from vector summation of three directional cutter forces according to the skew angle.

Table 4.5 The direction of resultant force according to the skew angle

Skew angle (degree)	penetration depth (mm)	Direction of resultant force on the cutting surface (degree)	Angle of resultant force with cutter axis (degree)
0	5	5.2	5.2
	7	5.7	5.7
	9	3.9	3.9
	11	6.9	6.9
	avg.	5.4	5.4
-5	5	-7.5	2.5
	7	-8.8	3.8
	9	-7.8	2.8
	11	-8.9	3.9
	avg.	-8.2	3.2
+5	5	7.5	2.5
	7	6.9	1.9
	9	10.6	5.6
	11	6.9	1.9
	avg.	8.0	3.0
-10	5	-9.9	0.1
	7	-11.9	1.9
	9	-10.9	0.9
	11	-9.9	0.1
	avg.	-10.7	0.7
+10	5	12.1	2.1
	7	10.5	0.5
	9	10.0	0
	11	10.8	0.8
	avg.	10.8	0.8
-15	5	-14.5	0.5
	7	-11.0	4.0
	9	-11.5	3.5
	11	-10.3	4.7
	avg.	11.8	3.2
+15	5	17.1	2.1
	7	17.3	2.3
	9	10.1	4.9
	11	10.9	4.1

Table 4.5 Continued.

Skew angle (degree)	penetration depth (mm)	Direction of resultant force on the cutting surface (degree)	Angle of resultant force with cutter axis (degree)
-20	5	-38.8	18.8
	7	-42.4	22.4
	9	-41.1	21.1
	11	-41.9	21.9
	avg.	41.1	21.1
+20	5	37.4	17.4
	7	38.1	18.1
	9	33.5	13.5
	11	38.1	18.1
	avg.	36.8	16.8

Figure 4.27 and figure 4.28 show the angle of the resultant force on the cutting surface with the cutter axis and the cutting direction. When the skew angle is 0° , the resultant force acts within 7° from the cutting direction, since the side force has the significant small portion of the resultant force compared with the other forces. When the skew angle increases by 5° , the direction of the resultant force acts with the angle of 7 to 10° between the cutting direction, and the resultant force acts within 5° of the center axis of the cutter. For 10° and 15° of skew angles, the resultant forces also act within about 10° and 15° with the cutting direction, respectively, and within 5° with the center axis of a pick cutter. The difference is minimized at 10° of the skew angle.

However, the side force at 20° of the skew angle is much larger than the other skew angle, so the direction of the resultant force is significantly different with the cutter axis, and the difference is about 20° . Although the

cutting efficiency (specific energy) can be optimized at 20° of the skew angle since the cutting force is reduced compared to the smaller skew angle, it should be considered that the direction of the resultant force and the skew angle of the cutter on the cutting surface greatly differ.

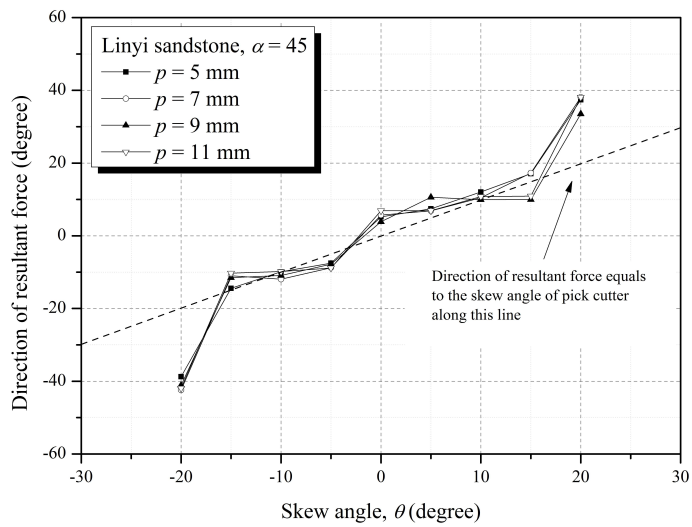


Figure 4.27 The direction of the resultant force on the cutting surface according to the skew angle

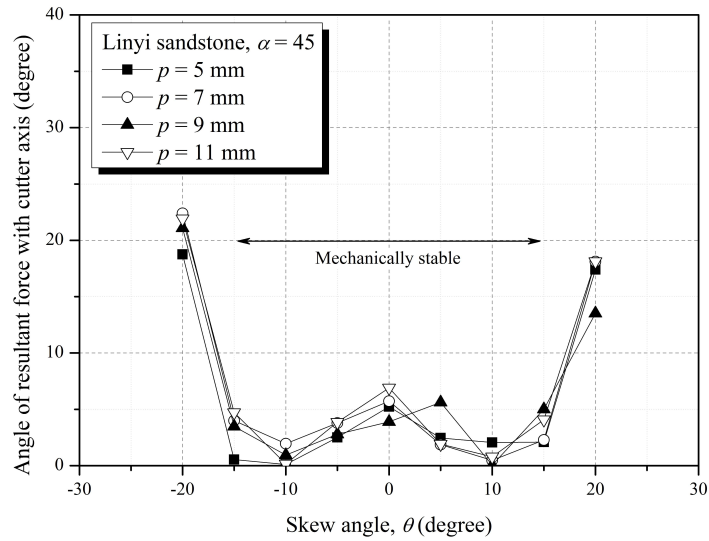


Figure 4.28 The difference between the direction of the resultant force and the cutter axis according to the skew angle

Figure 4.29 shows the change of cutting coefficient according to skew angle, and the skew angle is divided into three ranges (0° , $5\sim 10^\circ$ and 20°). As described in 4.5, the cutting coefficient was found at around one (0.91) where the skew angle is 0° . It was found at 1.24 where the skew angle ranges from 5° to 15° , and at 0.82 where the skew angle is 20° .

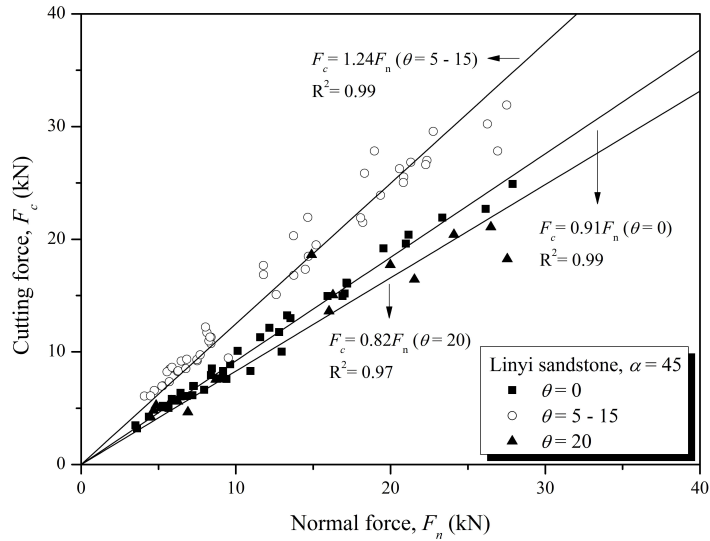
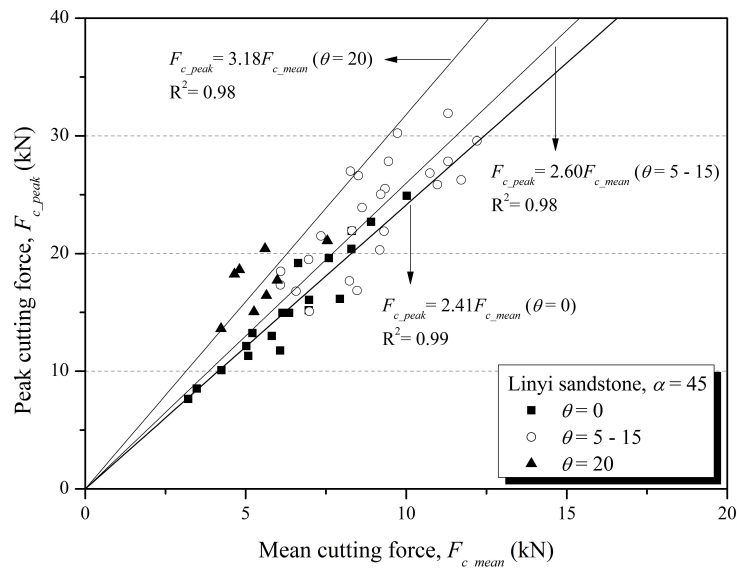


Figure 4.29 The cutting coefficients depending on the skew angle (Linyi-sandstone, attack angle = 45°)

As described in figure 4.5, the ratios of the peak cutter force to the mean cutter force of the normal and cutting forces were found to be around two, on the other hand, figure 4.30 shows the ratio of peak to mean of cutting, normal and side forces at the different range of skew angle, respectively. The result indicates that for all cutter forces, the ratio of the peak force to mean force gradually increased according to the skew angle. The ratio of cutting force increased from 2.41 to 3.18, the ratio of normal force increased from 2.28 to 3.45, and the ratio of side force increased from 2.24 to 3.07.

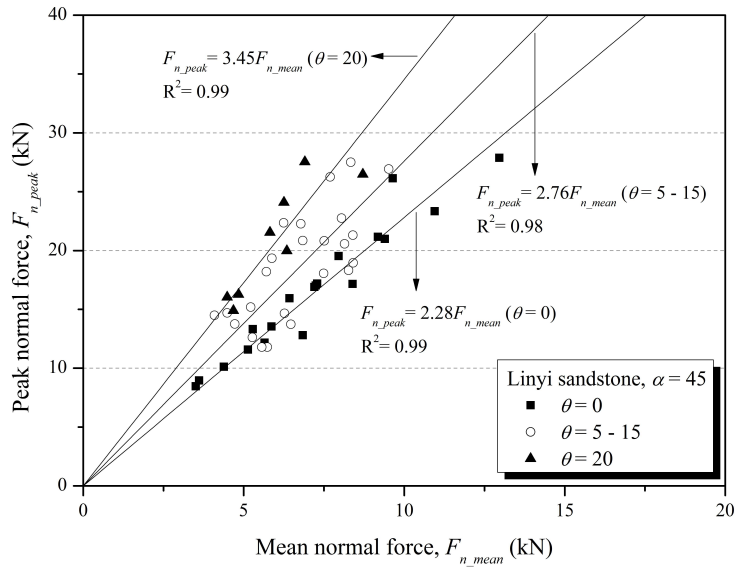
The values in this study were within the range of values reported in other previous studies, but this ratio varies depending on the brittle characteristics

of the rock and the cutting characteristics of the pick cutter. Therefore, these results indicate that when the skew angle is applied, the ratio of the peak force to the mean force generally increases, so it is necessary to consider the effect of the skew angle on the stability of the machine, but also on the cutting efficiency.

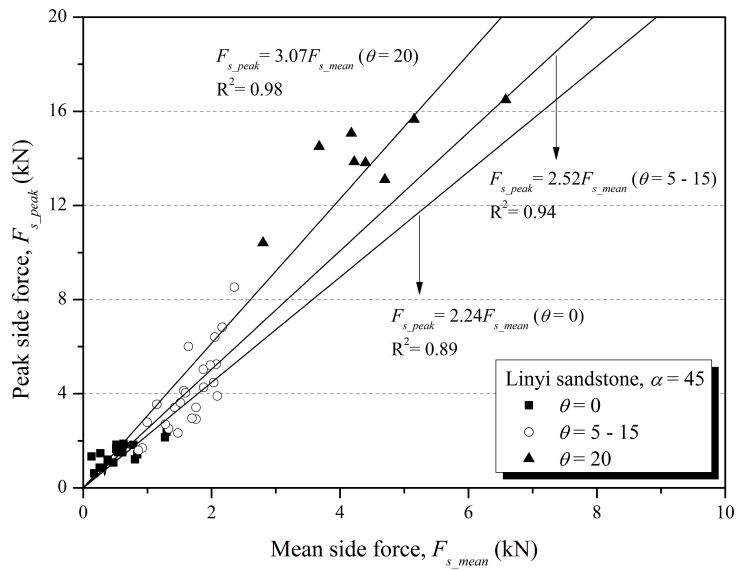


(a) Cutting force

Figure 4.30 The ratio of the peak to mean cutter forces depending on the skew angle (Linyi-sandstone, attack angle = 45°)



(b) Normal force



(c) Side force

4.3.3 Specific energy

Figure 4.31 and figure 4.32 showed the variation of the specific energy and normalized specific energy according to the skew angle at different penetration depths (with the optimum cut spacing). Compared to where the skew angle is 0° , the specific energy gradually increases according to the skew angle up to 10° , and it decreases as the skew angle up to 20° . The specific energy has the maximum value (normalized value = $1.06 \sim 1.79$) where the skew angle is 10° . The specific energies where the skew angle is 15° are still larger or similar as compared to the specific energy of 0° skew angle (normalized value = $0.97 \sim 1.38$). However at 20° of skew angle, the specific energy showed the lowest value (normalized value = $0.39 \sim 0.99$).

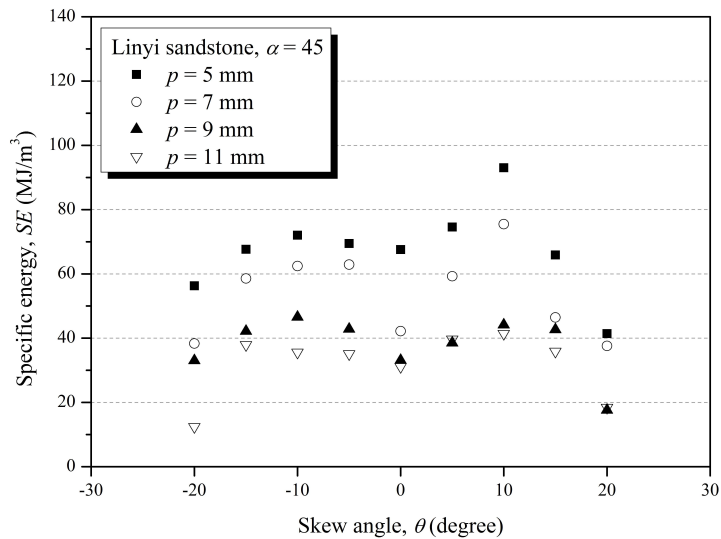


Figure 4.31 The specific energy according to the skew angle in different penetration depths

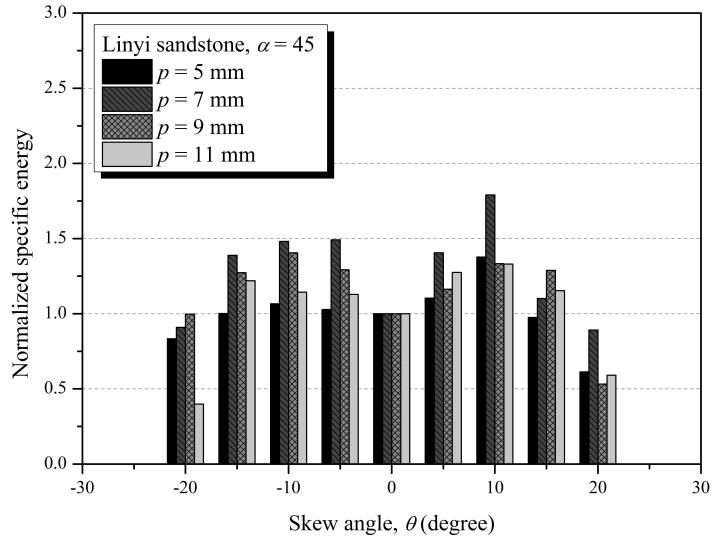
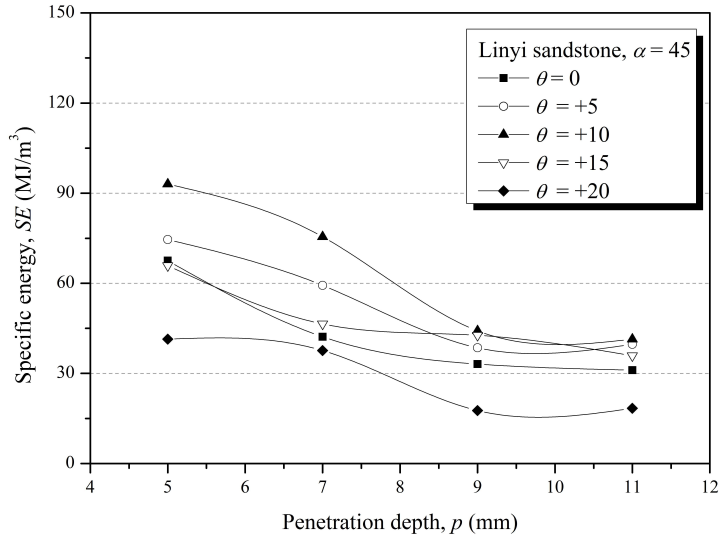


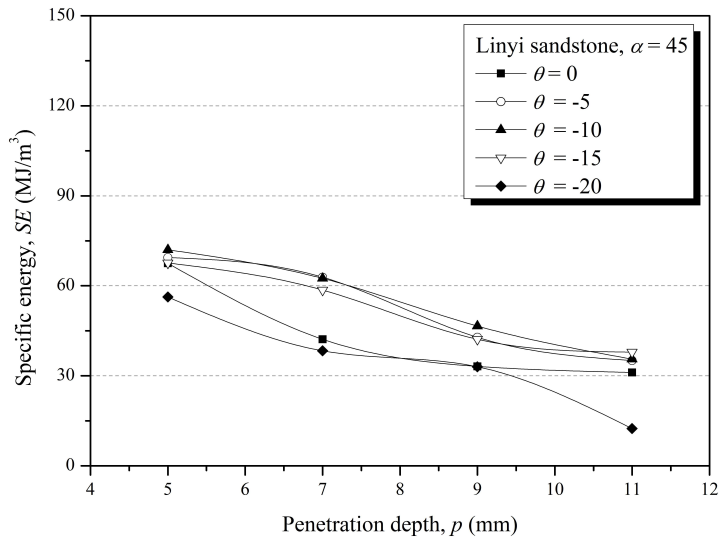
Figure 4.32 The normalized specific energy according to the skew angle in different penetration depths

Especially, where the penetration depth is 11 mm, the specific energy is significantly reduced compared to other penetration depths, the Normalized values of the -20° and $+20^\circ$ of skew angle were 0.39 and 0.59, respectively. In the case of the penetration depth of 5 mm, the variation of the specific energy according to the skew angle was not larger than that of the other penetration depths (normalized value = 0.39 ~ 0.99).

Figure 4.33 shows that this trend did not change even when the skew angle was applied (there was no significant difference between positive and negative skew angles). Moreover, the results concluded that the effects of penetration depth and the skew angle on the specific energy are independent of each other. In other words, the optimum skew angle can be determined regardless of the penetration depth.



(a) Positive skew angle

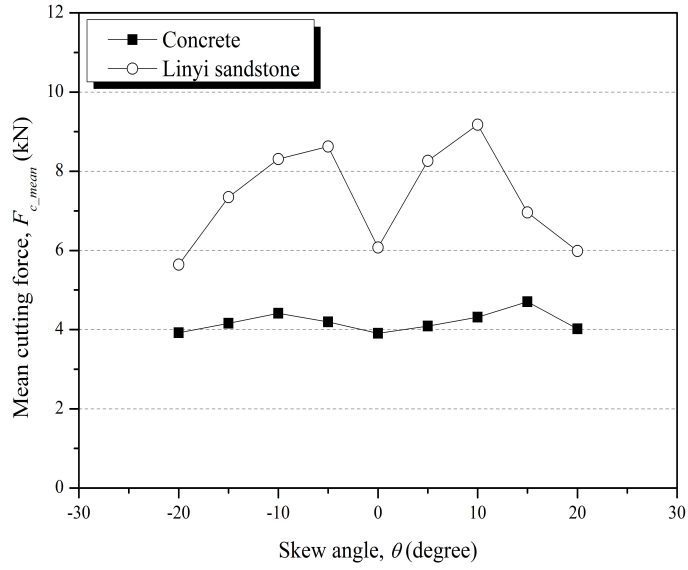


(b) Negative skew angle

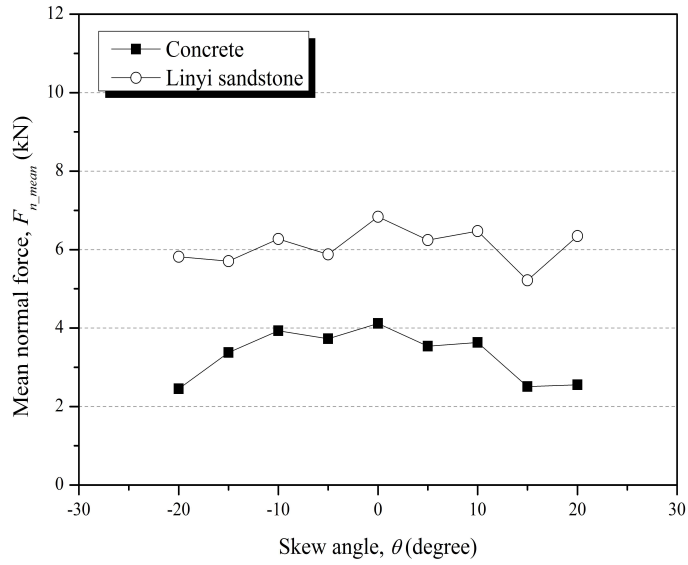
4.3.4 Concrete specimen

The LCM test was performed with the different skew angle for the concrete specimen to determine whether the results obtained from the above are affected by the rock types. For the testing, the penetration depth and cut spacing were set as 7 mm and 25 mm, respectively. Figure 4.34 shows the comparison result of the effect of the skew angle on the cutter forces in the Linyi sandstone and concrete specimens. For both specimens, the cutting force increased in the range of 5° to 15° skew angle compared to the skew angle of 0° and decreased at 20° of the skew angle. The normal force decreases according to the skew angle compared to when the skew angle is 0°, and the side force increases steadily as the skew angle increases and then increases drastically at 20 degrees.

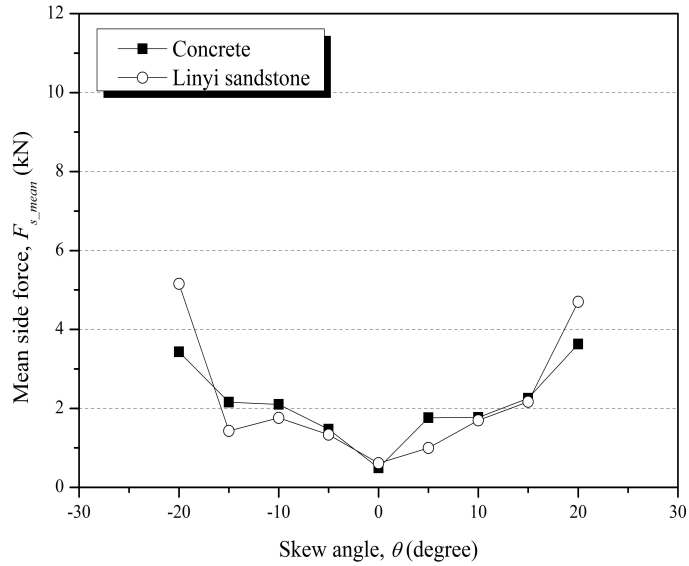
These results are similar to the result of the Linyi sandstone, and it concludes that the effect of the skew angle on the cutter force is independent of the rock type. Figure 4.35 shows the variation of the specific energy according to the skew angle in concrete, with the result of Linyi sandstone which performed with similar cutting conditions ($p = 7$ mm, $s = 21$ mm). Compared to the skew angle is 0°, the specific energy gradually increases according to the skew angle up to 10°, and it decreases as the skew angle up to 20°; The specific energy has maximum value where the skew angle is 10°. The specific energies where the skew angle is 15° are still larger or similar as compared to the specific energy of 0° skew angle, however, at +20° of skew angle, the specific energy showed the lowest value.



(a) Cutting force



(b) Normal force



(c) side force

Figure 4.34 The comparison of the effect of the skew angle on the side force in the Linyi sandstone and concrete (continued)

As the result of the cutter Force, according to the skew angle, the variation value of the specific energy is different, but the variation tendency agrees with each other. Therefore, it can be concluded that the effect of the skew angle on the specific energy is also independent of the type of rock. Regarding to the mechanical rock properties, the anisotropy of rock can be affect to the results of cutter forces and specific energy according to the skew angle.

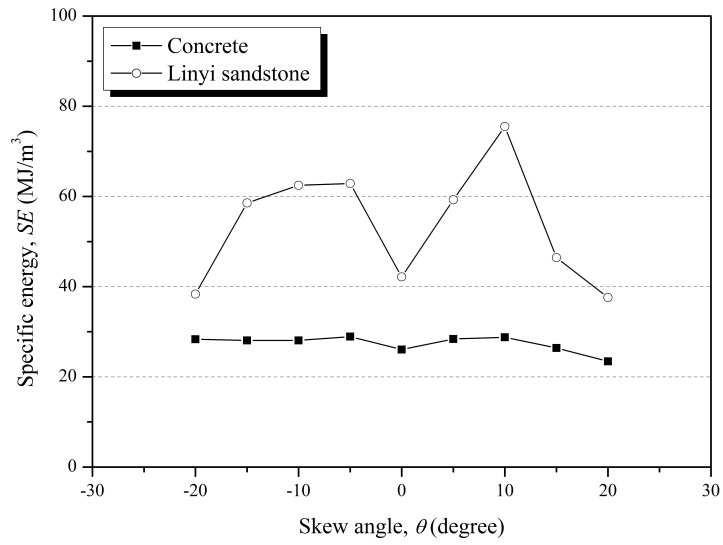


Figure 4.35 The comparison of the effect of skew angle on the specific energy in the Linyi sandstone and concrete

4.4 Effect of attack angle

4.4.1 Testing conditions

Park et al. (2016) reported that the optimum cutter spacing is influenced by the attack angle of a pick cutter. On the other hand, Shao (2017) reported that the attack angle significantly affects to the cutter forces of a pick and does not affect the optimum cutting conditions. Therefore, it is not enough to conclude the effect of the attack angle on the rock cutting mechanism, based on the results and discussions of the published literature up to now.

This study investigated the optimum cutting conditions under three different attack angles (35°, 45° and 55°) and penetration depths (5 mm and 7 mm). The test conditions and results were summarized in Table 4.6.

Table 4.6 The testing conditions and the results of the linear cutting test with different attack angles

Rock type	p (mm)	s (mm)	Skew angle (θ)	Attack angle (α)	Mean cutter force, F_{mean} (kN)			Peak cutter force, F_{peak} (kN)			Specific energy, SE^* (MJ/m ³)	
					Side	Cutting	Normal	Side	Cutting	Normal	M	C
Linyi sandstone	5	5	0	35	1.32	8.51	4.23	2.89	17.44	7.97	180.82	320.58
		10			1.07	12.50	6.24	2.83	24.11	11.74	164.38	244.33
		15			1.34	15.00	7.34	3.14	30.03	14.71	161.94	196.17
		20			0.89	15.03	7.48	2.07	36.37	17.84	142.71	196.60
		25			0.84	15.56	7.62	1.83	41.74	19.64	147.78	195.20
		5		0.81	3.21	3.61	1.21	7.64	8.95	86.70	131.14	
		10		0.13	4.25	4.38	1.33	10.08	10.12	80.09	86.68	
		15		0.17	5.21	5.29	0.62	13.24	13.32	81.95	70.90	
		20		0.53	5.81	5.87	1.59	12.99	13.54	67.57	74.15	
		25		0.27	6.35	6.43	1.47	14.95	15.93	89.86	64.84	
		5		0.85	1.70	2.00	1.98	4.25	4.51	61.37	115.33	
		10		0.98	1.88	2.25	2.38	5.25	4.94	47.12	42.43	
		15		0.77	1.97	2.35	1.97	5.48	4.95	51.51	41.94	
		20		1.07	2.81	2.86	2.31	8.49	7.19	39.62	53.71	
		25		0.89	2.76	2.70	2.08	9.55	6.83	50.38	87.06	

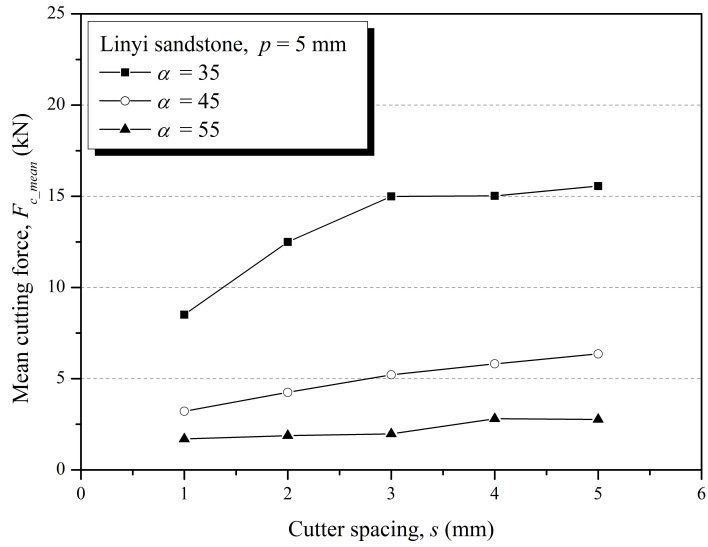
Table 4.6 The testing conditions and the results of the linear cutting test with different attack angles (Continued)

Rock type	p (mm)	s (mm)	Skew angle (θ)	Attack angle (α)	Mean cutter force, F_{mean} (kN)			Peak cutter force, F_{peak} (kN)			Specific energy, SE^* (MJ/m ³)	
					Side	Cutting	Normal	Side	Cutting	Normal	M	C
Linyi sandstone	7	7	0	35	1.42	12.34	6.12	3.04	24.59	11.72	141.16	329.52
		14			1.64	15.60	7.59	3.74	38.45	18.40	73.13	187.35
		21			1.32	18.38	8.71	2.96	45.26	21.17	70.26	160.01
		28			0.83	17.59	8.43	2.08	42.25	18.88	87.59	153.17
		7		45	0.47	3.48	3.51	1.08	8.53	8.46	54.74	90.57
		14			0.54	5.08	5.13	1.52	11.30	11.58	48.94	66.16
		21			0.61	6.07	6.84	1.51	11.76	12.80	42.17	50.29
		28			0.84	6.96	7.25	1.42	15.17	17.03	44.94	45.32
		7		55	0.39	2.17	2.54	3.73	8.56	6.18	48.12	70.49
		14			0.16	2.68	2.53	5.45	10.31	6.81	35.23	52.35
		21			0.24	3.61	3.40	2.85	10.02	7.88	34.34	39.14
		28			1.27	4.17	4.66	3.86	12.31	11.49	38.07	40.69

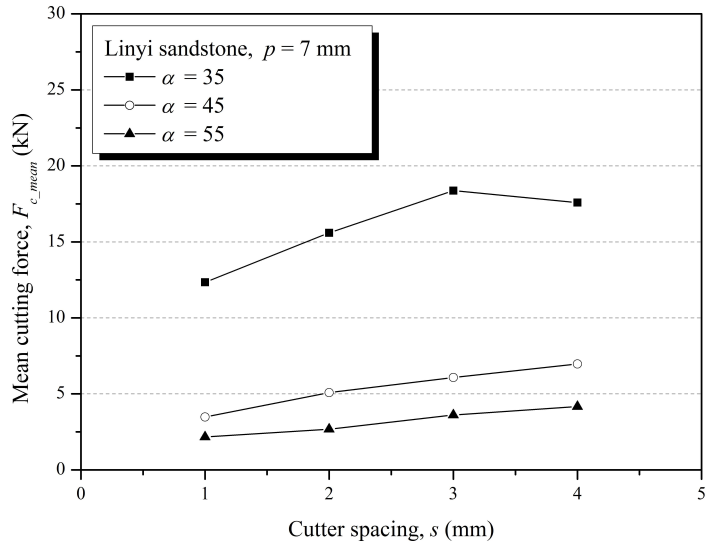
*“M” indicates the measured specific energy from the weighing method, and “C” indicates the calculated specific energy from the simple calculation method.

4.4.2 Cutter forces

Figure 4.36 shows the effect of the attack angle on the cutting force at penetration depths of 5 mm and 7 mm and different cut spacings. The cutting force slightly increases with the cut spacing, and it indicates that although the attack angle varies, the effect of the cut spacing on the mean cutting force is consistent. The result indicates that the cutting force is significantly influenced by the attack angle. Moreover, as the attack angle increases, the cutting force tends to decrease. Especially, the cutting force at 35° of attack angle, the cutting force was measured to be very large compared to the other two angles for both penetration depths. Because the cutter tip angle is fixed as 70° , the cutter tip entirely contacts with the rock surface when the attack angle is 35° (the clearance angle is zero degree in this case). The cutting force is highly related to the friction between the rock and pick cutter, so the cutting force increases with the contact area between the pick cutter and rock. Regarding the specific energy, the increase of the cutting force significantly indicates inefficient cutting. The attack angle should be larger than 35° in the installation of this type of pick cutter. Therefore, the relationship between the cutter tip angle and attack angle (clearance angle) should be considered.



(a) $p = 5$ mm

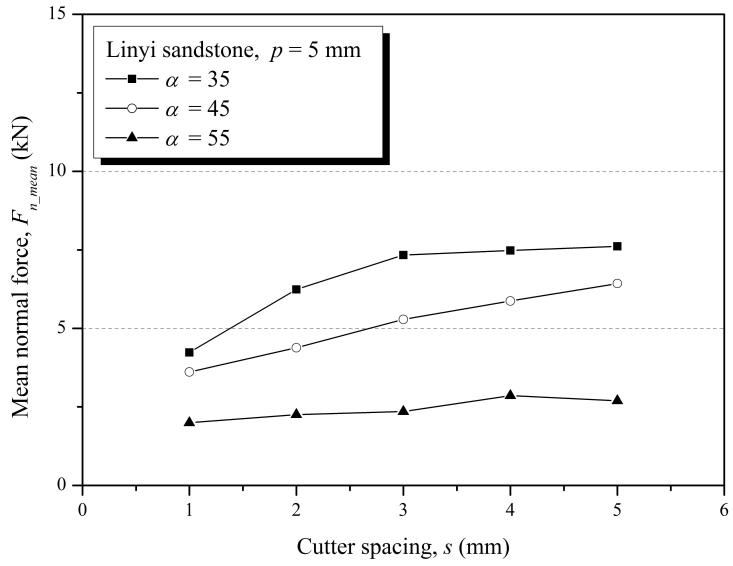


(b) $p = 7$ mm

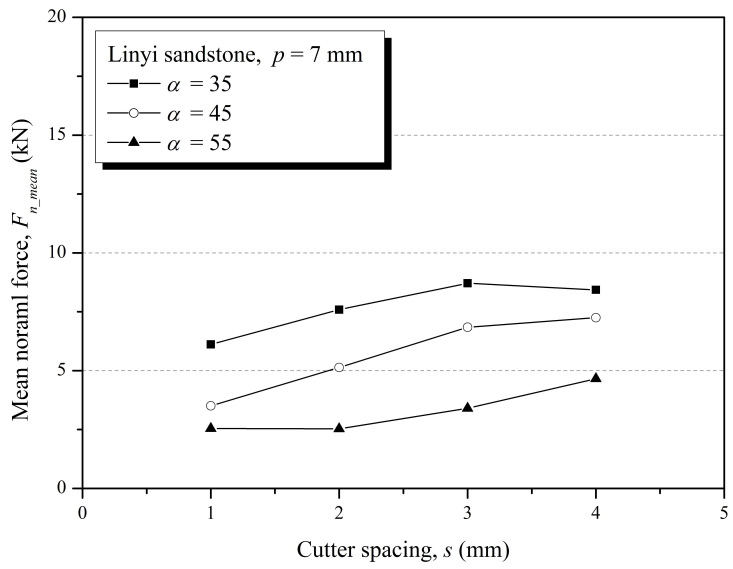
Figure 4.36 The effect of the attack angle on the cutting force at the different cut spacings and penetration depths

On the other hand, Figure 4.37 shows the variation of the normal force according to the attack angle in the cutting conditions mentioned above. The normal force showed the largest value at 35 degrees of attack angle compared with the other two attack angles, and it continuously decreased as the attack angle increased. While the cutter force drastically increases where the attack angle is 35°, the normal force gradually increases with the decreases of attack angle. Regarding the tip angle and attack angle, the relationship affects to the cutting force rather than the normal force, and the attack angle should be determined with consideration of cutter tip angle.

The normal force also slightly increases with the cut spacing, and it indicates that although the attack angle varies, the effect of the cut spacing on the mean normal force is consistent.



(a) $p = 5$ mm



(b) $p = 7$ mm

Figure 4.38 shows the ratio of cutting force to normal force according to the attack angle for two penetration depths. Because the ratio was not influenced by the cut spacing, the cut spacing was not considered, and the peak cutter force and the mean cutter force were shown together in the figure 4.34.

At 35° of attack angle, the ratio was found to be 2.07 ~ 2.14, and at the 45° and 55° of attack angle, the ratio was found to be 0.93 ~ 1.14, and there was no significant difference between the 45° and 55° of attack angles.

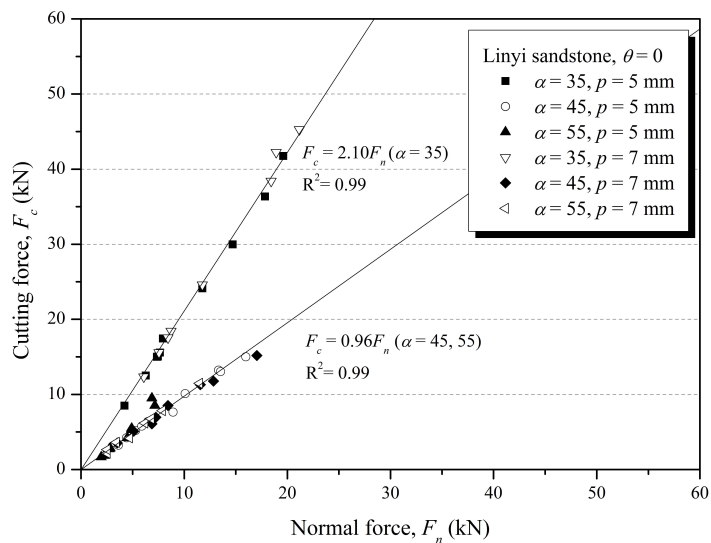


Figure 4.38 The ratio of the cutting force to the normal force at the different attack angles and penetration depths

However, if the attack angle of the pick cutter and the direction of the resultant force do not match, the bending force occurs in the pick cutter in

a direction orthogonal to the resultant force. Regarding mechanical stability of the machine, the conditions in which the direction of attack angle and resultant force are significantly different are not preferred.

Table 4.7 summarized the direction of resultant force and the difference between the attack angle and the direction of resultant force at the different cut spacing, penetration depth, and attack angle. The direction of the resultant force was independent of the penetration depth or cutter spacing and dependent on the attack angle. Based on the results of this study, it is considered that 45° degree is the most favorable attack angle regarding mechanical stability.

Table 4.7 The direction of resultant force according to the attack angle

Attack angle	penetration depth (mm)	Cut spacing (mm)	Direction of resultant force on the cutting surface (degree)	Angle of resultant force with attack angle (degree)
35	5	5	26.4	-8.6
		10	26.5	-8.5
		15	26.1	-8.9
		20	26.5	-8.5
		25	26.1	-8.9
		Average	26.3	-8.7
	7	7	26.4	-8.6
		14	25.9	-9.1
		21	25.4	-9.6
		28	25.6	-9.4
Average		25.8	-9.2	
45	5	5	48.3	3.3
		10	45.9	0.9
		15	45.4	0.4
		20	45.3	0.3
		25	45.3	0.3
		Average	46.0	1.0
	7	7	45.2	0.2
		14	45.3	0.3
		21	48.4	3.4
		28	46.1	1.1
Average		46.3	1.3	
55	5	5	49.6	-5.4
		10	50.1	-4.9
		15	50.0	-5
		20	45.5	-9.5
		25	44.3	-10.7
		Average	47.9	-7.1
	7	7	45.2	-9.8
		14	45.3	-9.7
		21	48.4	-6.6
		28	46.1	-8.9
Average		46.2	-8.8	

Figure 4.39 shows the ratio of peak to mean of cutting forces at the different attack angle. In Figure 4.3, the ratio of the peak force to the mean force for the cutting force and the normal force was 2.41 and 2.28, respectively. Without the data set for the cutting force at 55° of attack angle, the results indicate that the attack angle did not affect the ratio of the peak force to the mean force, thus the ratio is determined by the characteristics of the rock.

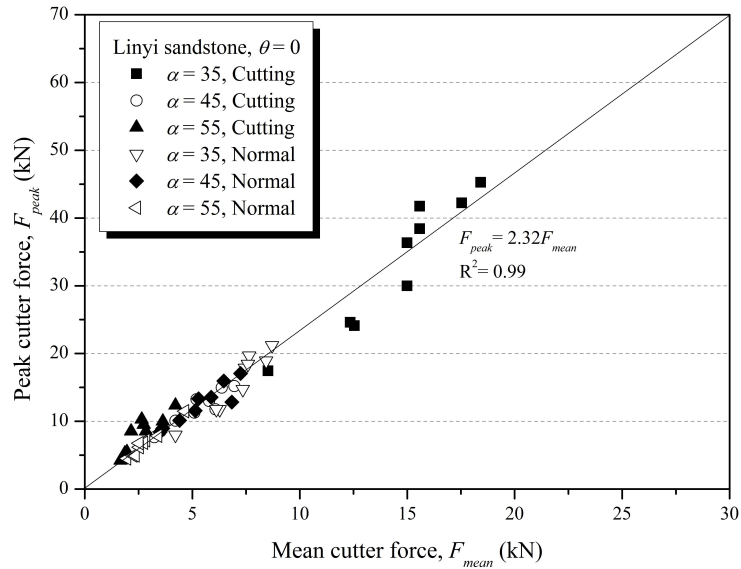
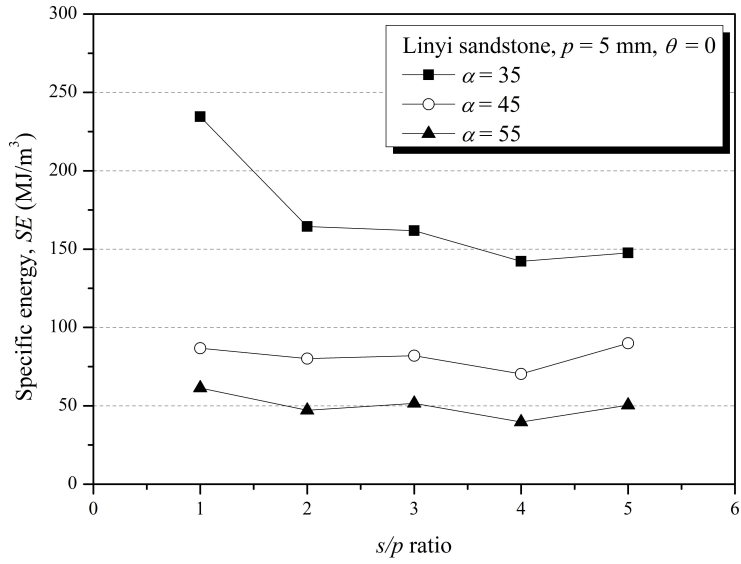


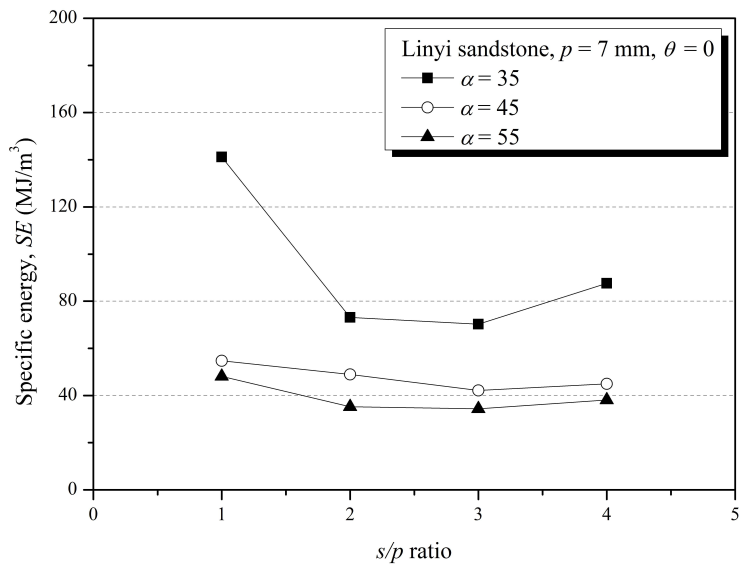
Figure 4.39 The ratio of the peak to the mean of cutting and normal forces at the different attack angles

4.4.3 Specific energy

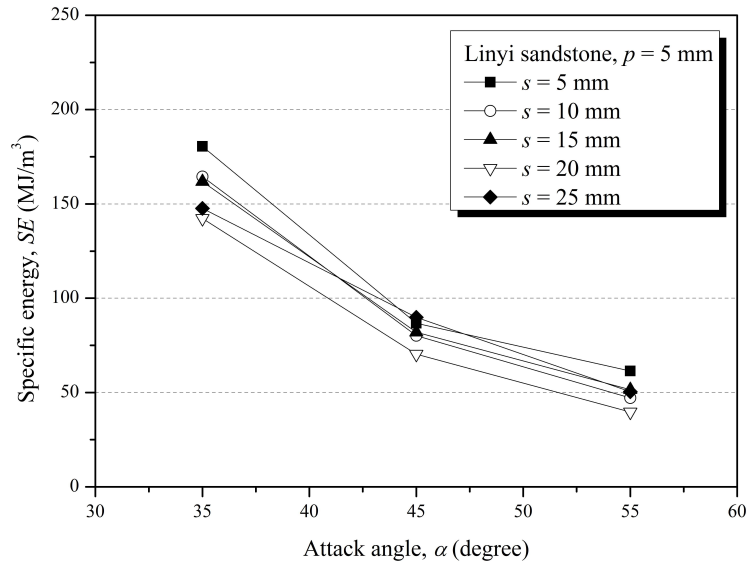
Figure 4.40 shows the relationship between the cut spacing and the specific energy at the different attack angle. The optimum cut spacings in 5 mm and 7 mm of penetration depths can be found at 20 mm, 21 mm, respectively, with regardless of attack angle. Of the three attack angles, 35° of attack angle is the most ineffective cutting condition. As the attack angle increases, the specific energy tends to decrease gradually under the same cut spacing and penetration depth (Figure 4.40). The effect of attack angle on the specific energy at various cut spacing is considered to be the same. It means that the effect of the attack angle and cut spacing on the specific energy is independent of each other. Thus, the optimum attack angle can be determined with consideration of the resultant force for the given rock type and the pick cutter. After that, the optimum cut spacing and penetration depth are determined by minimizing of the specific energy for the pre-determined attack angle.



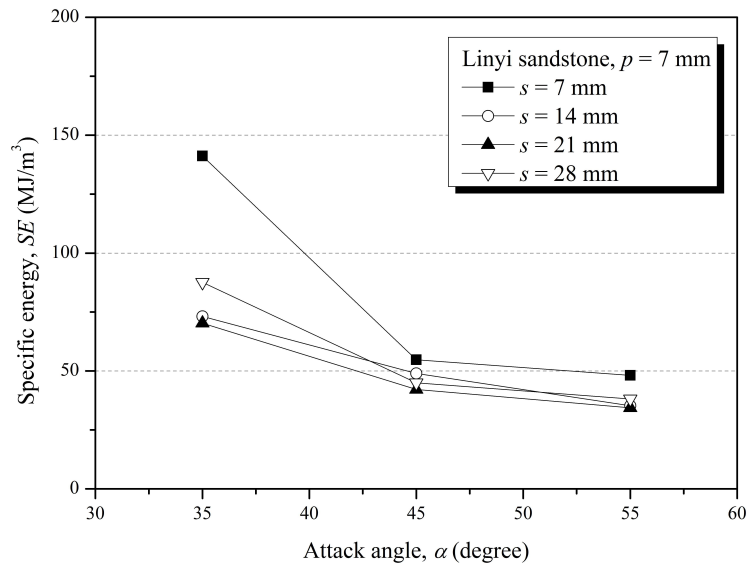
(a) $p = 5 \text{ mm}$



(b) $p = 7 \text{ mm}$



(a) $p = 5 \text{ mm}$



(b) $p = 7 \text{ mm}$

4.5 Relieved versus Unrelieved cut

The cutter force acting on pick cutter can be estimated from the several theoretical, experimental and numerical models. Of the models, in the theoretical model, only the peak cutting force in the unrelieved cut is considered and only the unrelieved cut is available in the core cutting test. If it is available to identify the correlation between the forces acting on two cutting modes based on the experimental database, the cutting forces acting on the pick cutter can be accurately predicted through a simple core cutting test or a theoretical model rather than a real cutting test.

As the original definition of the unrelieved cut, it can be defined as the cutting condition which the cut spacing is significantly larger than the optimum cut spacing. Alternatively, in the LCM test, the first cutting line is the significant unrelieved cut, regardless of any cutting conditions (i.e., cut spacing, penetration depth, skew angle and attack angle). Especially, when the other cutting conditions were constant, the cutter force obtained at the first cutting was not affected by the cutter spacing, which significantly affects the interactions between adjacent cutters.

Figures 4.42 and 4.43 show the correlation between the cutter forces of the relieved cut and the unrelieved cut at all the cutting conditions that performed on Linyi sandstone and concrete. The cutter force from the unrelieved cut is greater than that of the relieved cut by 1.27 to 1.36 times. Also, the ratio of cutter force in the unrelieved cut and the relieved cut was found to vary from 0.65 to 3.35.

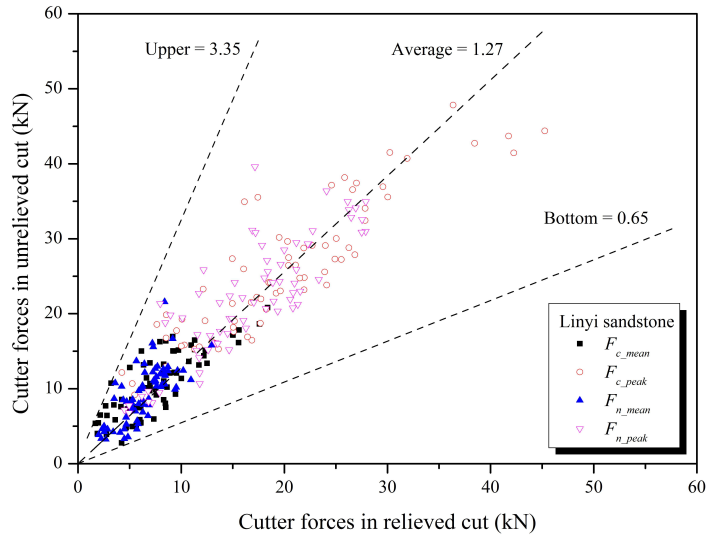
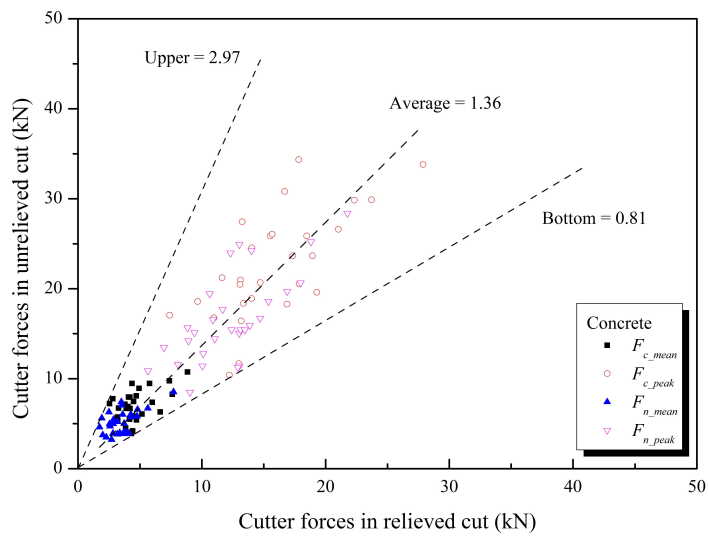


Figure 4.42 The comparison of the cutter forces in relieved cut and unrelieved cut (Linyi sandstone)



5. Chip size analysis

5.1 Chip size distribution

In this study, all of the rock chips generated after the linear cutting test were collected to analyze its size distribution as mentioned above. Figure 5.1 shows representative chip at the different penetration depths with optimum cut spacing (attack angle = 45° and skew angle = 0°).

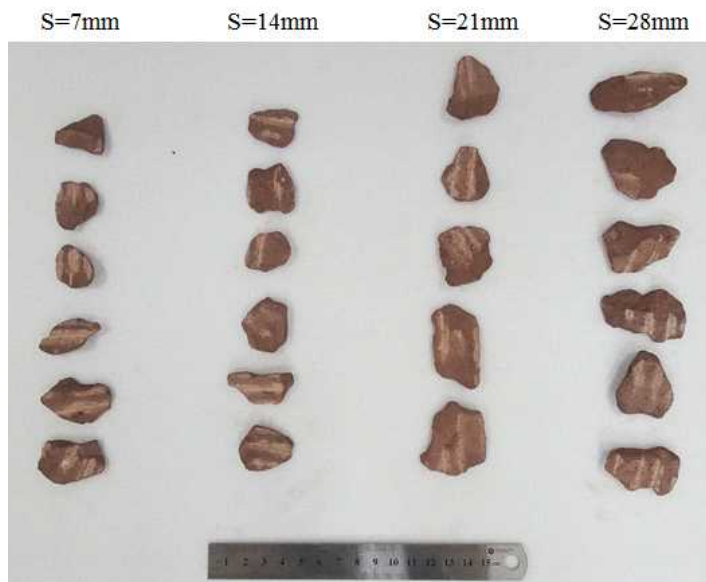
It can be seen that as the penetration depth increases, the size of the rock chip increases significantly at the optimum cutting spacing. The sizes of representative rock chips in each penetration depth are 20 mm \times 35 mm, 27 mm \times 45 mm, 35 mm \times 55 mm, 75 mm \times 45 mm, respectively. Figure 5.2 shows the photographs of rock chip at the different penetration depths and different cut spacings where the attack angle is 45° and skew angle is 0° . As the cutter interval increases, the size of the rock chip also gradually increases. The size of rock chip is maximized at the optimum cut spacings, at the larger cut spacings, for example 20 mm of cut spacing for 5 mm of penetration depth, the size of the rock chip decreases or becomes consistent after optimum cut spacing.



Figure 5.1 The representative rock chips in different penetration depth at optimum cut spacing



(a) penetration depth = 5 mm



(b) penetration depth = 7 mm

Figure 5.2 The photographs of the rock chip at the different penetration depths and different cut spacings



(c) penetration depth = 9 mm



(d) penetration depth = 11 mm

5.2 Size distribution parameters

The collected rock chip was analyzed using SPILT-DESKTOP software. The analysis is for the test results which performed under 45° of attack angle and 0° of the skew angle. The test results are suitable for analyzing the effect of the general cutting condition (cut spacing and penetration depth) on the size distribution of the rock chips produced by rock-cutting because the influence of other cutting conditions (i.e., attack angle and skew angle) can be excluded. The test conditions and the results are shown in Table 5.1, and the relationship between the variables is analyzed by the Spearman correlation matrix and summarized in Table 5.2.

Among the parameters, which were determined by the different methods, the coefficients of uniformity (C_u) and uniformity index (N) were highly correlated with each other ($r = -0.97$). The absolute size constant (D) has good correlation with D_{30} , D_{50} , D_{60} , D_{max} ; however, it has the poor correlation with D_{10} . The results show that the N and D determined by the Rosin-Rammler distribution can provide representative information to analyze the size distribution and particle of rock chip, respectively, compared with the parameters based on the soil mechanics theory.

The coarseness index was highly correlated with D , D_{30} , D_{50} , and D_{60} ($r = 0.96$, 0.96 , 0.97 and 0.93 , respectively), the cutter forces and the specific energy. On the other hand, it has the poor correlation with the size distribution parameters. The coarseness index can be considered as the parameter represents the particle size rather than size distribution of the particle.

Table 5.1 The results of LCM test and chip size distribution (Linyi sandstone)

Cutting Conditions (mm)		LCM results*			Size distribution				Particle size (mm)				
p	s	F_c mean	F_n mean	SE	C_u	C_c	CI	N	D	D ₁₀	D ₃₀	D ₅₀	D ₆₀
5	5	3.21	3.61	82.96	3.94	1.37	521.49	1.6	11.85	2.93	6.81	10.06	11.54
	10	4.25	4.38	77.65	3.16	1.29	527.47	1.86	11.49	3.55	7.16	9.88	11.23
	15	5.21	5.29	77.86	3.43	1.34	562.34	1.85	12.33	3.8	8.16	11.46	13.04
	20	5.81	5.87	67.57	4.9	1.44	575.22	1.42	14.75	3.02	8.01	12.61	14.79
	25	6.35	6.43	85.81	4.1	1.38	561.64	1.54	13.75	3.24	7.71	11.49	13.29
7	7	3.48	3.51	54.74	5.81	1.49	557.61	1.32	13.84	2.42	7.11	11.76	14.05
	14	5.08	5.13	48.94	4.08	1.3	660.01	1.47	20.22	4.55	10.49	15.66	18.55
	21	6.07	6.84	42.17	3.02	1.27	659.19	1.92	17.62	5.9	11.57	15.74	17.82
	28	6.96	7.25	44.94	4.01	1.38	669.76	1.57	19.74	4.98	11.69	17.38	19.95
9	9	5.02	5.65	49.73	3.74	1.35	654.86	1.71	17.52	4.99	11.21	16.31	18.64
	13.5	6.15	7.20	45.66	4.46	1.33	699.34	1.41	23.69	5.08	12.37	18.93	22.64
	18	6.63	7.96	37.69	3.87	1.37	728.87	1.51	25.95	6.25	14.39	21.06	24.21
	23.5	8.29	9.18	36.50	3.49	1.34	696.50	1.72	20.85	6.14	13.26	18.85	21.4
	27	7.59	9.40	33.12	3.83	1.36	736.24	1.56	25.32	6.45	14.69	21.5	24.69
	36	8.30	10.95	39.70	3.59	1.34	734.23	1.62	25.41	6.86	15.07	21.74	24.66
11	11	6.97	7.29	46.30	15.26	1.84	670.99	0.9	25.10	1.74	9.23	20.3	26.55
	22	7.93	8.39	34.39	4.09	1.38	708.39	1.49	23.78	5.62	13.35	19.96	23
	33	8.90	9.64	31.10	7.67	1.61	755.99	1.16	28.55	4.1	14.41	25.77	31.44
	44	10.02	12.96	32.71	4.99	1.44	714.97	1.33	25.93	5.02	13.44	21.43	25.07

*The units of F_c mean, F_n mean and SE are kN, kN and MJ/m³, respectively.

Table 5.2 The spearman correlation matrix of the parameters

	Cutting Conditions		LCM results			Size distribution			Particle size						
	p	s	$F_c\ mean$	$F_n\ mean$	SE	C_u	C_c	CI	N	D	D_{10}	D_{30}	D_{50}	D_{60}	D_{max}
p		0.38	0.81	0.83	0.83	0.37	0.34	0.82	-0.48	0.87	0.42	0.73	0.88	0.92	0.88
s			0.81	0.79	-0.25	0.04	0.16	0.68	-0.05	0.60	0.54	0.73	0.64	0.56	0.44
$F_c\ mean$				0.98	-0.66	0.25	0.34	0.85	-0.30	0.84	0.54	0.83	0.87	0.86	0.74
$F_n\ mean$					-0.69	0.26	0.29	0.86	-0.31	0.85	0.54	0.83	0.86	0.87	0.76
SE						-0.17	-0.09	-0.76	0.32	-0.78	-0.53	-0.69	-0.76	-0.79	-0.74
C_u							0.82	0.71	-0.97	0.32	-0.48	-0.05	0.27	0.40	0.53
C_c								0.15	-0.74	0.28	-0.46	-0.02	0.28	0.38	0.41
CI									-0.32	0.96	0.70	0.96	0.97	0.93	0.87
N										-0.47	0.34	-0.10	-0.40	-0.52	-0.66
D											0.58	0.89	0.97	0.96	0.93
D_{10}												0.84	0.60	0.46	0.35
D_{30}													0.92	0.83	0.74
D_{50}														0.97	0.90
D_{60}															0.95
D_{max}															

Figure 5.2 shows the relationship between the mean particle size (D_{50}) and the particle size parameters at the different passing rates (i.e., 10, 30, 60 and 100%). The particle sizes at the different passing rates had good linear relationships between the mean particle size. However, D_{10} is lower correlation value with the mean particle size based on the Spearman correlation analysis. The maximum particle size (D_{max}) is 2.7 times bigger than the mean particle size. As the results, the mean particle size can be representative particle size parameters among the parameters, and to be parameters representing the particle size, the passing rate must be at least 30%.

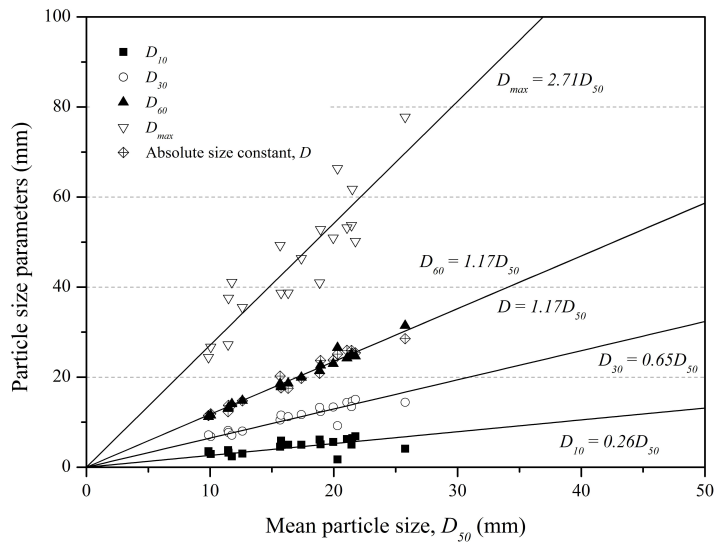


Figure 5.2 The relationship between the mean particle size (D_{50}) and the different particle size parameters (Linyi sandstone)

Figure 5.3 shows the effect of the cut spacing on the particle size which

was represented by coarseness index. The result shows that the coarseness index tends to maximize where the cut spacings were optimum conditions at the different penetration depth. The higher the coarseness index means that there is a high probability that the larger size of rock chip will be produced. Based on the rock cutting mechanism, it is reasonable that the size of rock chip is maximized around the optimum cut spacing.

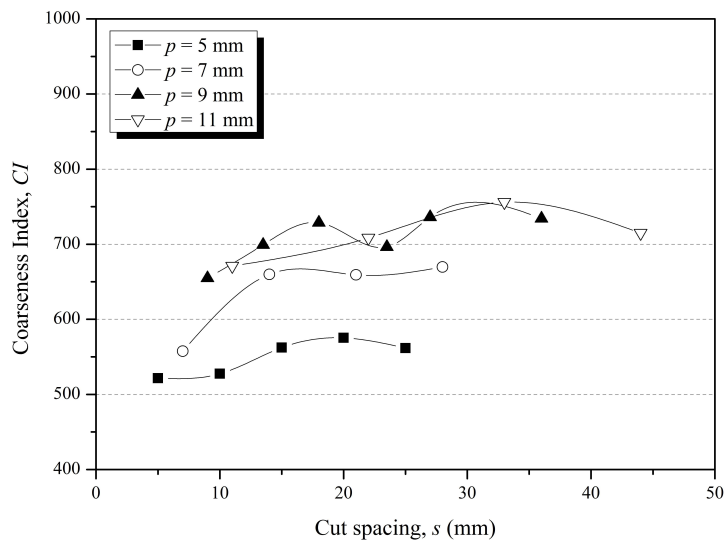


Figure 5.3 The effect of the cut spacing on the coarseness index (Linyi sandstone)

Figure 5.4 shows the relationship between the cutter forces and the mean particle size (D_{50}). The maximum The cutter forces linearly increased with the mean particle size. The maximum chip size appeared at the 11 mm of penetration depth and 33 mm of cut spacing. The results indicate that the larger cutter force was required to cut the rock into the larger debris.

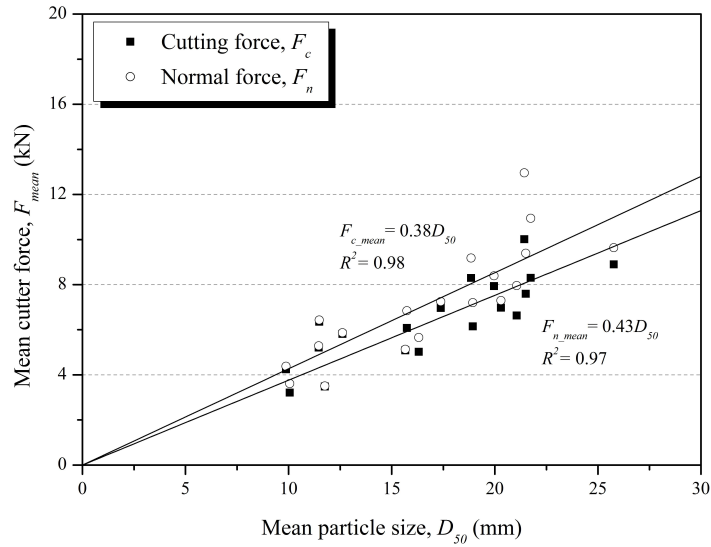


Figure 5.4 The relationship between the mean particle size and the cutter forces (Linyi sandstone)

In addition to, figure 5.5 shows the relationship between coarseness index and specific energy. The relationship also indicates the cutting condition with the larger coarseness index is more efficient conditions. The result had good agreement with the previous studies (Roxborough, 1973; Altindag, 2003; Kahraman, 2004; 2005; Tuncdemir et al., 2008; Abu Bakar and Gertsch, 2013), it was proven that the specific energy decreases with the increase of the coarseness index. As mentioned above, the coarseness index is dependent on the sieve sizes which are used in the analysis, and then the testing data is not representative values for the cutting tools. However, the similar trend and results of this study indicate that the image processing technique can provide the quantitative information to analyze the size

distribution of the rock chip compared with the direct sieving test.

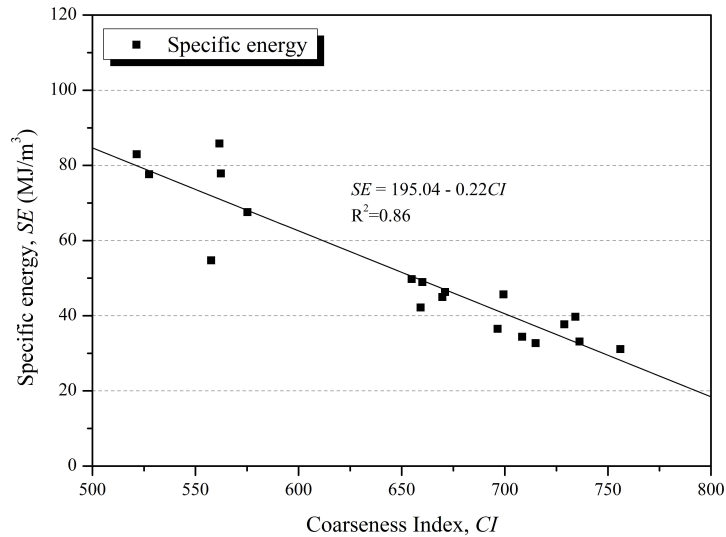


Figure 5.5 The relationship between the specific energy and coarseness index (Linyi sandstone)

Figure 5.6 shows the effect of the penetration depth on the characteristic of particle size and its distribution. It is clearly found that the larger penetration depth, the larger size of the rock chip is produced, and the distribution has the lower uniformity. In addition to, the particle size and its distribution are more dependent on the penetration depth than the cut spacing. Based on the rock cutting theory, It is well-known the maximized rock fragmentation induces the efficient rock-cutting. Thus, the results supported the that the operational condition with the deep penetration depth is efficient cutting condition.

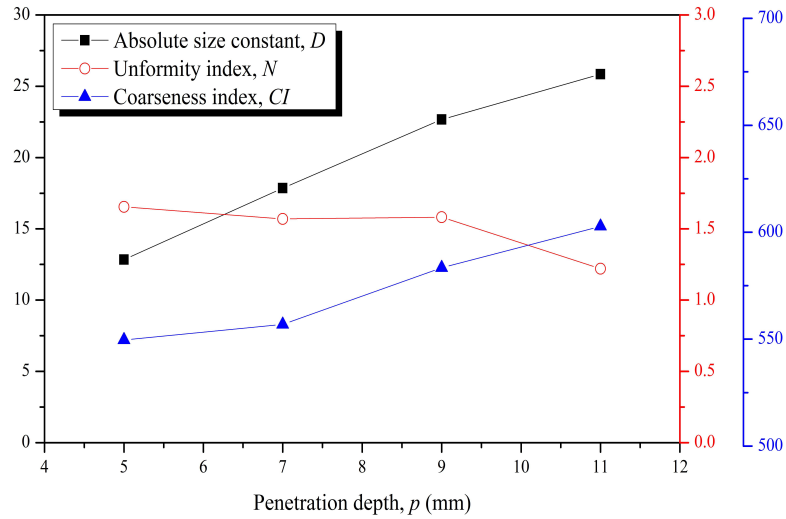


Figure 5.6 The relationships between the penetration depth, absolute size constant, uniformity index, and coarseness index (Linyi sandstone)

5.3 Rock powder generation

It is well known that the condition for maximizing the chip size is efficient cutting conditions. The previous result of the size distribution indicates well the fact. As the mechanism of rock cutting, compressive stress concentration occurs directly under the cutter in contact with the rock, so that the rock in that part is crushed into rock powder (very fine material) rather than the rock chip.

It is not preferable to increase the proportion of rock powder in mining by mechanical excavation, and rock powder is difficult to recover compared with rock chip. Therefore, especially when working in subsea, these rock

powders meet with water and produce the slurry, which increases the cutter force and causes the cutting efficiency to decrease (Jackson et al., 2007).

In this study, the volume of the rock fragments obtained after the cutting test was classified into rock powder and rock chips to analyze the proportion of the rock powder in rock cutting.

There are many available standards to classify the soil particle depending on its size, and the standards were summarized in Table 5.3. Of the standards, Unified Soil Classification System (ASTM, 1999) is generally adopted for the classification of the soil particle. In this study, the particles less than 2 mm in diameter are defined as rock powder according to the classifications.

Table 5.3 Soil particle size classification

Name of organization	Grain size (mm)			
	Gravel	Sand	Silt	Clay
Unified Soil Classification System (USCS)*	76.2 to 4.75	4.75 to 0.075	Fines (i.e., silts and clays) <0.075	
U.S. Department of Agriculture (USDA)	>2	2 to 0.05	0.05 to 0.002	<0.002
American Association of State Highway and Transportation Officials (AASHTO)	76.2 to 2	2 to 0.075	0.075 to 0.002	<0.002
Massachusetts Institute of Technology (MIT)	>2	2 to 0.06	0.06 to 0.002	<0.002

*USCS was suggested by U.S. Army Corps of Engineers, U.S. Bureau of Reclamation, and American Society for Testing Materials

Figure 5.7 shows the rock particles sieved in each sieve, and Table 5.4 presents the results of the rock powder analysis in this study.



(a) 20 mesh (2 mm)



(b) 40 mesh (0.4 mm)



(c) 100 mesh (0.0675 mm)



(d) pass

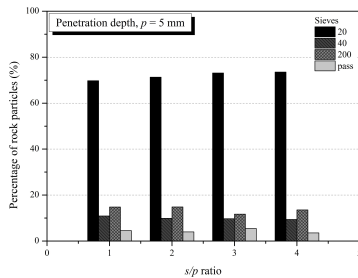
Figure 5.7 The rock particles sieved by the 20, 40 and 100 meshes of sieves

Table 5.4 The results of the analysis for the rock powder generation (Linyi sandstone, $\alpha = 45$, $\theta = 0$)

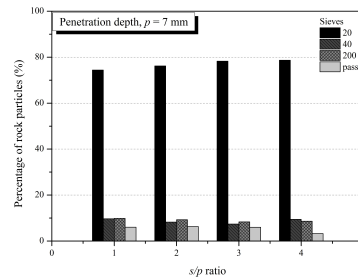
p (mm)	s (mm)	Total (g)	Remained rock debris on sieve (g)				Chip (g)	Powder (g)	Powder /Chip (%)	Powder /Total (%)
			10	40	200	pass				
5	5	220.8	154	24.1	32.7	10.0	154	66.8	43.4	30.3
	10	316.8	225.9	31.3	47	12.6	225.9	90.9	40.2	28.7
	15	189.7	138.7	18.4	22.2	10.4	138.7	51	36.8	26.9
	20	246.8	181.5	23.2	33.4	8.7	181.5	65.3	36.0	26.5
	25	210.8	151.8	19.6	26.9	12.5	151.8	59	38.9	28.0
7	7	164.2	122.2	15.9	16.2	9.9	122.2	42	34.4	25.6
	14	275.2	209.7	22.7	25.5	17.3	209.7	65.5	31.2	23.8
	21	367.9	287.9	27.2	30.7	22.1	287.9	80	27.8	21.8
	28	416	327.3	39.3	35.9	13.5	327.3	88.7	27.1	21.3
9	9	352	281.8	23.9	32.4	13.9	281.8	70.2	24.9	20.0
	13.5	440.9	371	23.2	31.9	14.8	371	69.9	18.8	15.8
	18	516.4	414.4	11.7	50.3	40	414.4	102	24.6	19.8
	22.5	424.7	359.7	24.4	23.2	17.4	359.7	65	18.1	15.3
	27	468.1	420.4	21	23.5	3.2	420.4	47.7	11.4	10.2
	36	365	311.7	22.7	20.4	10.2	311.7	53.3	17.1	14.6
11	11	306.5	266.8	17.3	15.2	7.2	266.8	39.7	14.9	13.0
	22	475.7	425	21	20.6	9.1	425	50.7	11.9	10.7
	33	593	536.9	24	21.8	10.3	536.9	56.1	10.5	9.5
	44	473.5	427.3	20.4	17	8.8	427.3	46.2	10.85	9.8

5.3.1 Effect of the penetration depth and cut spacing

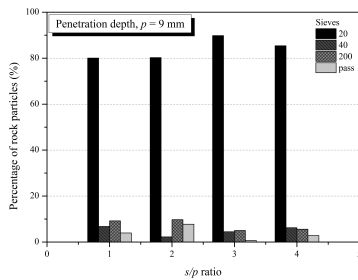
Figure 5.8 shows the distribution of the rock particles sieved by the 20 (2 mm), 40 (0.4 mm) and 200 (0.0675 mm) mesh of standard sieves according to the cut spacing and the penetration depth. The result indicates that the proportion of the rock particles sieved by each sieve (with respect to the total mass) is consistent with cut spacing.



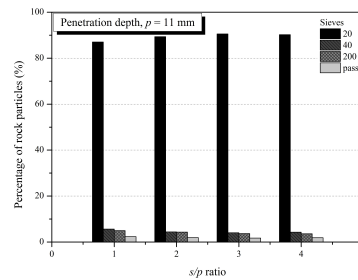
(a) $p = 5$ mm



(b) $p = 7$ mm



(c) $p = 9$ mm



(d) $p = 11$ mm

Figure 5.8 The distribution of the sieved rock particles according to the s/p ratio

As mentioned above, the particles sieved by 20 mesh of sieve were classified as rock powder in this study. As shown figure The percentage of

rock powder for the total weight of cut rock at the 5 mm, 7 mm, 9 mm and 11 mm of penetration depths were 28.1% (26.5 ~ 30.3%), 23.1% (21.3 ~ 25.6%), 15.9% (10.2 ~ 19.9%) and 11.5% (9.5 ~ 13.0%), respectively, on average. In addition, the percentage of rock powder for significant chip at the 5 mm, 7 mm, 9 mm and 11 mm of penetration depths were 39.5% (36.0 ~ 43.4%), 30.1% (27.1 ~ 34.37%), 19.2% (11.4 ~ 24.9%) and 12.0% (10.5 ~ 14.9%), respectively.

Also, the ratio of rock powder tended to decrease linearly with the penetration depth (Figure 5.9). The results are reasonable; the possibility of producing a large size chip increases as the penetration depth increases. However, because the limited penetration depths were considered in this study, the discussion for the deeper penetration depths will be possible in further studies.

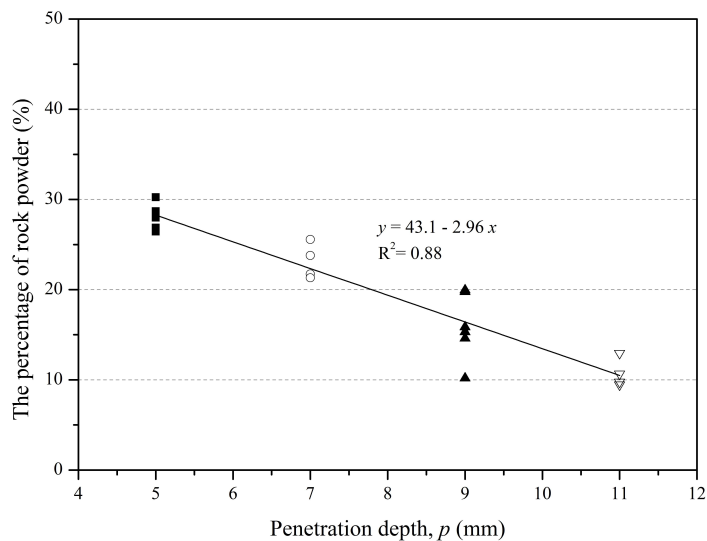


Figure 5.9 The percentage of rock powder according to the penetration depth (Linyi sandstone)

5.3.2 Effect of the skew angle

Table 5.5 summarizes the sieving results of rock particles according to skew angle and figure 5.10 shows the ratio of rock powder in the cut rock according to the skew angle. The result shows that compared with the case where the skew angle is 0° , the skew angle is considered to increase the ratio of rock powder. The ratio increases in the range of 5° to 15° , and it decreases at 20° of the skew angle. At 20° of the skew angle, it is still larger than that of 0° of the skew angle. Especially, the ratio of rock powder in the volume of cut rock increased up to 50% at the penetration depth of 5 mm.

Table 5.5 The results of the analysis for the rock powder generation with different skew angles

p (mm)	s (mm)	Skew angle, θ (degree)	Total (g)	Remained rock debris on sieve (g)				Chip (g)	Powder (g)	Powder /Chip (%)	Powder /Total (%)
				10	40	200	pass				
5	20	0	246.9	181.5	23.2	33.4	8.7	181.5	65.3	36.0	26.5
		-5	370.5	253.1	26.2	68.9	11.2	253.1	106.3	42.0	29.6
		5	371.1	234.3	27.8	82.5	15.5	234.3	125.8	53.7	34.9
		-10	210.3	136.1	15.1	40.5	7.3	136.1	62.9	46.2	31.6
		+10	194.5	122.4	15.1	40.0	6.1	122.4	61.2	50.0	33.3
		-15	378.8	243.8	29.9	83.5	10.5	243.8	123.9	50.8	33.7
		+15	438.2	282.7	35.5	95.7	13.8	282.7	145.0	51.3	33.9
		-20	344.5	225.7	28.4	69.3	10.6	225.7	108.3	48.0	32.4
	+20	489	339.9	35.3	90.2	13.3	339.9	138.8	40.8	29.0	
7	21	0	368.0	287.9	27.2	30.7	22.1	122.2	42	27.8	21.7
		-5	433.7	298.7	29.2	81.7	13.2	298.7	124.1	41.5	29.4
		5	441.5	325.0	23.8	70.8	10.9	325.0	105.5	32.5	24.5
		-10	421.1	320.3	21.7	58.8	9.3	320.3	89.8	28.0	21.9
		+10	384.7	280.1	40.3	43.6	9.3	280.1	93.2	33.3	25.0
		-15	463.1	322.1	32.5	86.7	10.9	322.1	130.1	40.4	28.8
		+15	632.3	438.7	44.9	124.4	12.6	438.7	181.9	41.5	29.3
		-20	542.8	384.1	35.7	96.5	15.5	384.1	147.7	38.5	27.8
	+20	503	375.3	28.2	76.3	12.9	375.3	117.4	31.3	23.8	

Table 5.5 The results of the analysis for the rock powder generation with different skew angles (Continued)

9	27	0	468.2	420.4	23.9	32.4	13.9	420.4	70.2	16.7	14.3
		-5	920.6	709.9	51.8	129.3	19.1	709.9	200.2	28.2	22.0
		5	1032.1	820.1	51.0	133.0	17.2	820.1	201.2	24.5	19.7
		-10	382.6	307.7	16.3	42.3	5.9	307.7	64.5	21.0	17.3
		+10	405	317.0	17.7	51.0	8.4	317.0	77.1	24.3	19.6
		-15	574.5	438.3	31.4	81.7	11.8	438.3	124.9	28.5	22.2
		+15	576.9	433.7	34.3	86.8	11.3	433.7	132.4	30.5	23.4
		-20	481.5	361.1	28.0	71.6	10.2	361.1	109.8	30.4	23.3
		+20	759.3	587.8	40.3	104.6	15.9	587.8	160.8	27.4	21.5
11	33	0	593.0	536.9	24.0	21.8	10.3	266.8	39.7	10.4	9.5
		-5	1326.5	1103.8	49.9	138.6	20.2	1103.8	208.7	18.9	15.9
		5	1141.7	951.3	41.1	118.6	19.3	951.3	179.0	18.8	15.8
		-10	520.8	436.5	18.0	47.3	8.6	436.5	73.9	16.9	14.5
		+10	419.4	331.3	18.4	50.8	8.1	331.3	77.3	23.3	18.9
		-15	628	479.0	34.8	92.7	10.3	479.0	137.8	28.8	22.3
		+15	716.5	558.1	34.9	99.6	13.2	558.1	147.7	26.5	20.9
		-20	789.3	652.6	32.8	79.9	13.0	652.6	125.7	19.3	16.2
		+20	642.1	512.3	28.3	78.4	12.3	512.3	119.0	23.2	18.8

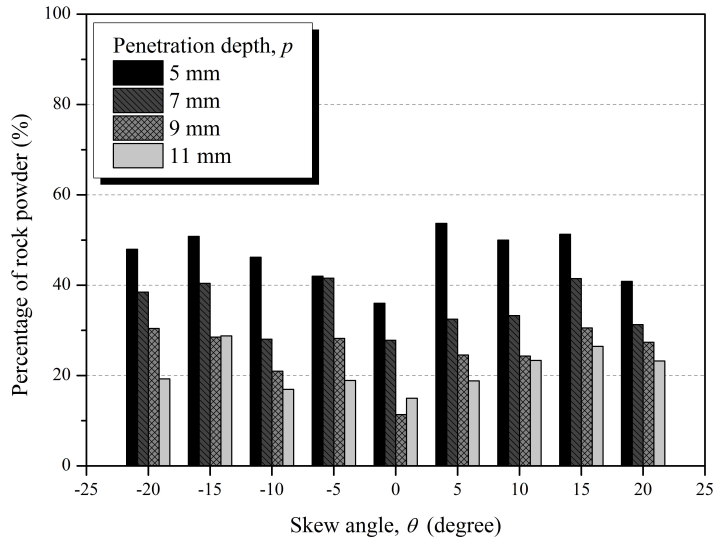


Figure 5.10 The effect of the skew angle on the rock powder producing (Linyi sandstone)

On the other hand, as described in Figure 5.10 above, the ratio of rock powder generally decreases with increasing penetration depth at the same skew angle. When the skew angle is 0° , -10° and -15° , their tendency deviates from that of the other skew angle, however, it can be considered as an experimental error.

As the skew angle of the pick cutter changes, the geometric size and shape of the cross-sectional area in contact with the rock will change. Therefore, when the skew angle is changed, the shape and area of the stress field in the crushed zone are changed. The results of rock powder ratio indicate the fact, and it concludes that the skew angle greatly affects the cutting efficiency of the rock. Moreover, there is no difference in the effect

of the negative skew angle and the positive skew angle on the chip formation of the rock.

5.3.3 Correlation with specific energy

Figure 5.11 shows the correlation between the specific energy and the ratio of rock powder. The LCM test results for the different skew angle are also considered in the analysis. The results show that as the ratio of rock powder increased, the specific energy also increased linearly.

Since the rock chip is created by the interaction of cracks due to the interaction between adjacent cutters, it means that the larger the mass of the chipped rock and the larger the chip size, the more efficient the cutting condition.

Because the rock chip is created by the connection of tensile cracks due to the interaction between the adjacent cutters, the larger volume of rock by chipping and the larger the size of the rock, the more efficient the cutting conditions. On the contrary, rock powder is produced in the crushed zone beneath the pick cutter after cutting, and this rock powder is completely crushed by the high level of compressive stress. To crush rocks by compressive stress, much more energy is required than the chipping. This is due to the mechanical characteristics of the rock. Because the rock behaves like brittle material, it has a weaker strength under tensile stress than under compressive stress.

Therefore, the proportion of rock powder for the total volume of cut rock is an indicator to estimate cutting efficiency. The higher the ratio of rock

powder, the more inefficient the cutting is. In contrast, the lower the ratio of rock powder means that it is considered to be an efficient cutting condition because it means that many rocks have been cut by chipping.

Therefore, the result of this study is reasonable, and to reduce the generation of rock powder, and it is possible to consider the increase of the penetration depth or not applying the skew angle like the determination of efficient cutting condition. It can be concluded that cutting efficiency was higher at the larger depth of cut as less rock powder, and more and larger chips were generated.

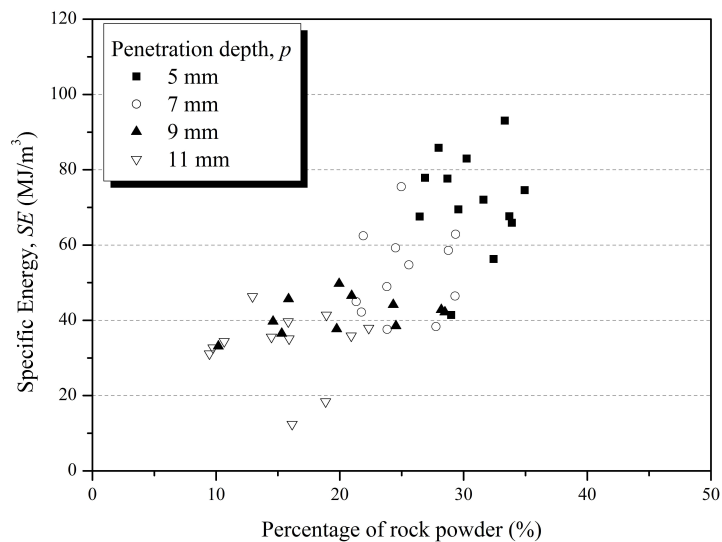


Figure 5.11 The relationship between the proportion of rock powder and the specific energy (Linyi sandstone)

6. Numerical modelling of rock cutting

6.1 Limitation of FEM in rock cutting simulation

As described in the literature review section (Chapter 2), various numerical techniques have been studied to simulate rock cutting processes by cutting tools. Among them, FEM is the most widely used technique to simulate the rock-cutting process. However, since the characteristics of the FEM technique, meshes are highly distorted by indentation and penetration process in rock cutting model simulated with FEM, and it should suffer from excessive mesh distortion and large deformation of mesh that may cause the failure of simulation. The erosion (element deletion) and re-meshing were applied to prevent the mesh distortion problem. The re-meshing is the time-consuming process, and the use of the erosion option has difficulties; erosion causes losses of internal energy, strength, and mass, it has the possibility that the accuracy of calculation decreases.

It is critical to determine the appropriate erosion criteria since the use of the erosion strongly affect the results of numerical simulation. Moreover, its application to the simulation requires the calibration with experimental results because they are not a material property or physics-based phenomena, and they cannot be quantitatively calculated; user can set the erosion with different ways (i.e., principal stress, principal strain, geometric strain, plastic strain, timestep, etc.), and each of these methods is divided into several criteria. There is a formula for calculating erosion strain and stress, and it can be calculated in simple one dimension problems. However, it is

impossible to calculate erosion strain and stress in complicated three-dimensional problems.

It may provide a useful way to simulate certain behavior or event with experimental observation, but it is limited without experimental observation. Despite the weaknesses, the erosion option is essential means in Lagrangian (FEM) calculation to handle large deformation and excessive distortion of meshes.

Some studies have suggested empirically recommended the criteria and erosion values for specific materials and analysis cases. However, it means that the value is appropriate for a similar type of numerical analysis and is not representative of the material for all analysis cases. Therefore, use of the values derives inappropriate results in other types of analysis, or numerical analysis itself may not be possible.

For rock cutting simulation, if the experimental results and the target value are available, the criterion erosion value can be found by trial and error for each rock type and cutting condition. However, this erosion criterion only meets the cutting conditions and rock types, and therefore, it derives an inappropriate result if the value is applied to the other rocks or the cutting conditions.

The fact is also supported by the previous studies, the different erosion values and criteria have been used to simulate the rock cutting process, and they are summarized in Table 6.1.

Table 6.1 The different erosion criteria and value used for the rock cutting simulation in previous studies

References	Criterion	Input value	Remarks
Xia et al., 2017	Instantaneous geometric strain	1.5	LS-DYNA
Cho et al., 2010	Incremental Geometric strain	Ranged value	AUTODYN
Huang et al., 2016	Not shown	Not shown	LS-DYNA
Yang et al., 2016	Not shown	Not shown	LS-DYNA

Until now, of the available literature, the numerical simulation of the rock cutting process using FEM has been studied only to compare the numerical results with experimental results for limited cases. Also, all of the FEM analysis take account the erosion technique into their modeling. The numerical method satisfies various cutting conditions and rocks has not been developed until now.

To deal with these limitations regarding of erosion technique, there are following ways;

- 1) Modeling the rocks without the erosion (Elements only occurred failure)
- 2) Determine the universally applicable erosion criterion for rock cutting rock-cutting regardless cutting conditions and rock types (apply as high erosion value as possible to minimize the effect of erosion on the numerical result)
- 3) Development of the calculation method for erosion value depending on the rock properties (Even though, all elements must not be removed by

erosion before they reach the failure criteria).

The first way is the method of simulating the fragmentation process of rock using only the failure criterion of the rock model without the erosion technique. However, it is impossible to simulate the rock cutting process in a conventional FEM because excessive deformation occurs in the rock elements.

In a second way, it is also difficult to determine the universal erosion values and criteria because there are many kinds of the criteria, and the range of its value is also very extensive. Even if the value can be determined, there is no guarantee that it will be suitable for all rock types and cutting conditions.

Although the third way is the best way to solve the problems in use of the erosion technique, it is impossible to set an appropriate erosion value and criterion on the basis of the rock properties up to now. If a theoretical model is developed that can fully describe the rock cutting process in three dimensions, then the third way can be used to overcome the limitation of erosion in FEM.

Moreover, use of erosion technique in rock cutting has the additional limitation regarding measuring for cutter forces. The limitation was already discussed in the several previous studies (Cho et al., 2010; Cho et al., 2013; Qeng et al., 2017;)

In the rock-cutting simulation, the problem in measuring the cutter force is that the cutter force is instantaneously dropped to zero by removal of the mesh due to the erosion. The previous studies measured the cutter force

with reasonable assumptions, but it is far from the measured cutter force in actual rock cutting test. These limitations are minimized with finer meshes, and it is also limited since the increasing of computation time.

6.2 Smooth particle hydrodynamics

AUTODYN hydrocode (hydrocode loosely defined as a code for solving large deformation, finite strain transient problems that occur on a short time scale) is capable of computing strains, stresses, velocities and propagation of shock wave as a function of time and position. AUTODYN has the capability to use various numerical methods for describing the physical governing equations: Grid-based methods (Lagrange and Euler) and mesh-free method SPH (Smooth particle hydrodynamics).

The Smooth Particle Hydrodynamics (SPH) is an N-body interaction scheme developed by Lucy (1977), Monaghan and Gingold (1983). The method was developed to avoid the limitations of mesh tangling and distortion in extreme deformation problems with the FEM. The main difference between the FEM and the SPH method is the absence of a grid (Villumsen and Fauerholdt, 2008). SPH is a mesh-free Lagrangian method. In SPH the medium is divided into a set of discrete elements, referred to as particles. There is no connectivity between the adjacent particles. The contribution of each particle to a property at a point of interest is weighted according to the distance of the particle from the point of interest. The particle approximation in SPH is defined using the function:

$$\Pi^h f(x) = \int f(y) W(x-y, h) dy \quad (6.1)$$

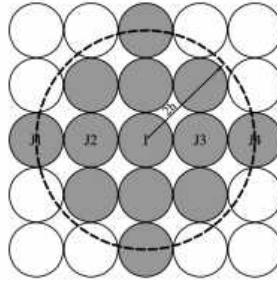
where W is the Kernel (or smoothing) function. The Kernel function is defined using the function θ by the relation:

$$W(x, h) = \frac{1}{h(x)^d} \theta(x) \quad (6.2)$$

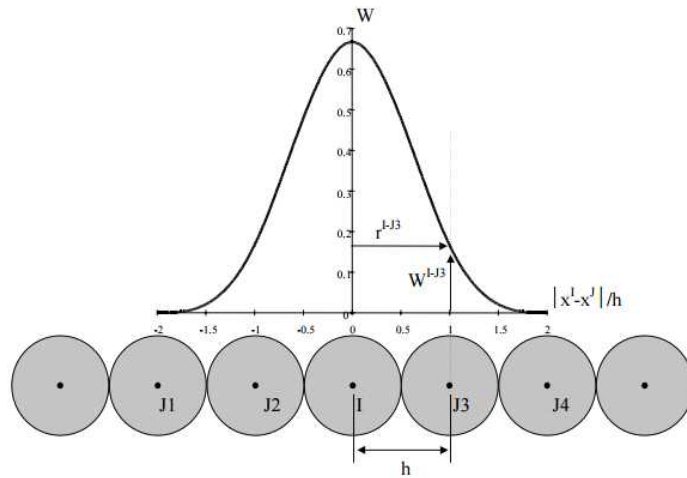
where d is the number of space dimensions and h is the so-called smoothing length which varies in time and space. $W(x, h)$ should be a centrally peaked function. The most common smoothing kernel function used along with SPH is the cubic B-spline which is defined by choosing θ as:

$$\theta(u) = C \times \begin{cases} 1 - \frac{3}{2}u^2 + \frac{3}{4}u^3 & \text{for } |u| \leq 1 \\ \frac{1}{4}(2-u)^2 & \text{for } 1 \leq |u| \leq 2 \\ 0 & \text{for } 2 < |u| \end{cases} \quad (6.3)$$

where C is a constant of normalization which depends on the number of spatial dimensions, and $u = \frac{r}{h}$, r is distance between two particles, h is the smoothing length (figure 6.1).



(a) Particles within two smoothing length



(b) Kernel density function (1-dimension)

Figure 6.1 Kernel function for the interpolation of SPH (Century Dynamics, 2005)

The SPH method is based on a quadrature formula for moving particles, and the location of particle i which moves along the specific velocity field (v) is expressed as $x_i(t)$, where $i \in \{1..N\}$. Then equation 6.1 can rewrite as:

$$\Pi^h f(x) = \sum_{j=1}^N w_j f(x_j) W(x_i - x_j, h) \quad (6.4)$$

where w_j is the weight of the particle j . The weight of a particle varies proportionally to the divergence of the flow. The SPH formalism implies a derivate operator. A particle approximation for the derivative operator must be defined. Before giving the definition of this approximation, the gradient of a function is defined as:

$$\nabla f(x) = \nabla f(x) - f(x) \nabla l(x) \quad (6.5)$$

where l is the unit function. The particle approximation to the gradient of a function can be defined:

$$\Pi^h \nabla f(x) = \sum_{j=1}^N \frac{m_j}{\rho_j} [f(x_j) A_{ij} - f(x_i) A_{ij}] \quad (6.6)$$

where $A_{ij} = \frac{1}{h^{d+1}} \theta' \left(\frac{\|x_i - x_j\|}{h} \right)$.

To the solve the conservation equations in discrete form, a solution is required:

$$L_v(\phi) + \text{div} F(x, t, \phi) = S \quad (6.7)$$

where $\phi \in R^d$ is the unknown, F^β with $\beta \in [1..d]$ represents the conservation law and L_v is the transport operator defined by:

$$L_v : \phi \rightarrow L_v(\phi) = \frac{\partial \phi}{\partial t} + \sum_{l=1}^d \frac{\partial (v^l \phi)}{\partial x^l} \quad (6.8)$$

The equation with strong form can be written, however, the strong form solution is not conservative; therefore the formulation is numerically not acceptable. Thus AUTODYN is compelled to use the weak form, in the weak form the adjoint of the L_v operator is used:

$$L_v^* : \phi \rightarrow L_v^*(\phi) = \frac{\partial \phi}{\partial t} + \sum_{l=1}^d v^l \frac{\partial (\phi)}{\partial x^l} \quad (6.9)$$

The discrete form of this operator corresponds to the discrete formulation of the adjoint of $D_{h,s}$:

$$D_{h,s}^* \phi(x_i) = \sum_{j=1}^N w_j [\phi(x_i) A_{ij} - \phi(x_j) A_{ij}] \quad (6.10)$$

A discrete adjoint operator for the partial derivative is also necessary and is taken to be with the α -th component of the operator:

$$D^* \phi(x_i) = \sum_{j=1}^N w_j \phi(x_j) A^\alpha(x_i, x_j) - w_j \phi(x_i) A^\alpha(x_j, x_i) \quad (6.11)$$

These definitions are leading to a conservative method. Thus all the conservative equations encountered in the SPH method will be solved using the weak form. With the definitions above, the conservation equations can

be written in their discrete form. The equation of conservation of mass is evaluated with the following SPH approximation:

$$\frac{d\rho}{dt} = -\rho \operatorname{div}(v), \quad \frac{d\rho}{dt}(x_i) = \sum_{j=1}^N m_j [v(x_j) - v(x_i)] A_{ij} \quad (6.12)$$

The SPH momentum equation can be written as:

$$\frac{dv^\alpha}{dt}(x_i) = \sum_{j=1}^N m_j \left[\frac{\sigma^{\alpha,\beta}(x_i)}{\rho_i^2} A_{ij} - \frac{\sigma^{\alpha,\beta}(x_j)}{\rho_j^2} A_{ji} \right] \quad (6.13)$$

where α and β are the space indices, and the energy conservation equation is:

$$\frac{dE}{dt}(x_i) = -\frac{P_i}{\rho_i^2} \sum_{j=1}^N m_j [v(x_j) - v(x_i)] A_{ij} \quad (6.14)$$

Therefore, the summation of the value of the function at all neighboring particles (interpolation points J1, J2, I, J3 and J4) multiplied by weighting function to calculate the value of a function at particle I. Hence, the SPH particle are not simply interesting mass points but they are interpolation points from which values of functions and their derivatives can be estimated at discrete points in the continuum. In SPH, the discrete points at which all quantities are evaluated are placed at the center of the SPH particles (Century Dynamics, 2005).

Figure 6.2 shows the basic steps used in each calculation cycle, as

6.3 Numerical Model

6.3.1 Pick cutter model

The pick cutter used in this study is the 735MB which manufactured by Vermeer, and the schematic and modeled pick cutter is shown in figure 3.6. The material model of the pick cutter was tungsten carbide which used for the cutter tip, and its material properties was determined by using the properties provided by the AUTODYN-3D library (Holmquist et al., 2005, Weerasooriya et al., 2005, Century dynamics, 2005).

The strength of the material is defined by the von Mises function and the pick cutter model is assumed not to be wear and the failure function is not defined; the cutter wear out due to cutting the rock, but it cut the rock model in a short distance (200 mm) compared to the real cutting condition.

The equation 6.1 is the Von Mises constitutive model for metal which is on the large deformation, high strain rate, high-temperature condition.

$$\sigma = [A + B \epsilon^n][1 + C \ln \dot{\epsilon}^*][1 - T^{*m}] \quad (6.1)$$

where, ϵ is the equivalent plastic strain, $\dot{\epsilon}^* = \dot{\epsilon}/\dot{\epsilon}_0$ is the dimensionless plastic strain. The constants A, B, n, C, m is the material properties, and they are summarized in Table 6.2

In order to decrease the computation time of numerical analysis, the pick cutter is partially modeled using only the part in contact with rock (Figure 6.3).

Table 6.2 Input parameters of tungsten carbide for modelling of pick cutter

Category	Model	Parameter	Input value
Equation of State	Shock	Density	18.1 (g/cm ³)
		Gruneisen coefficient	4000
		S1	1.268
Strength	Von Mises	Shear Modulus	160 (GPa)
		Yield stress	2 (GPa)
Failure	-	-	-



Figure 6.3 The modeled pick cutter used in numerical simulation in this study

6.3.2 Rock model

(1) Material model

- Equation of state (EOS): rock models were considered homogeneous and isotropic. The initial elastic behavior expressed by an approximation to Hooke's law (Century Dynamics, 2005). The properties of the rock models were represented using a linear equation of state (EOS). Bulk modulus, and

shear modulus were calculated based on elasticity, and the reference temperature was set to room temperature, 20 C.

- Strength model: The different strength models have been used to simulate the rock cutting process in the previous studies. The function for yield stress of the material is determined by the strength model in AYTODYN. Tham (2005) introduced the Drucker-Prager yield function which is suitable for the elasto-plastic material such as rock models. The yield points under uniaxial tension and compression were assumed to be 90% of brazilian tensile and compressive strength of rock, respectively.

- Failure model : AUTODYN provides several the failure model according to the strength and EOS of the material. Of the model, the principal stress/strain based model and the damage based model which calculate the damage of rock based on the plastic strain of element are generally used to simulate the fragmentation or cracking behavior of rock.

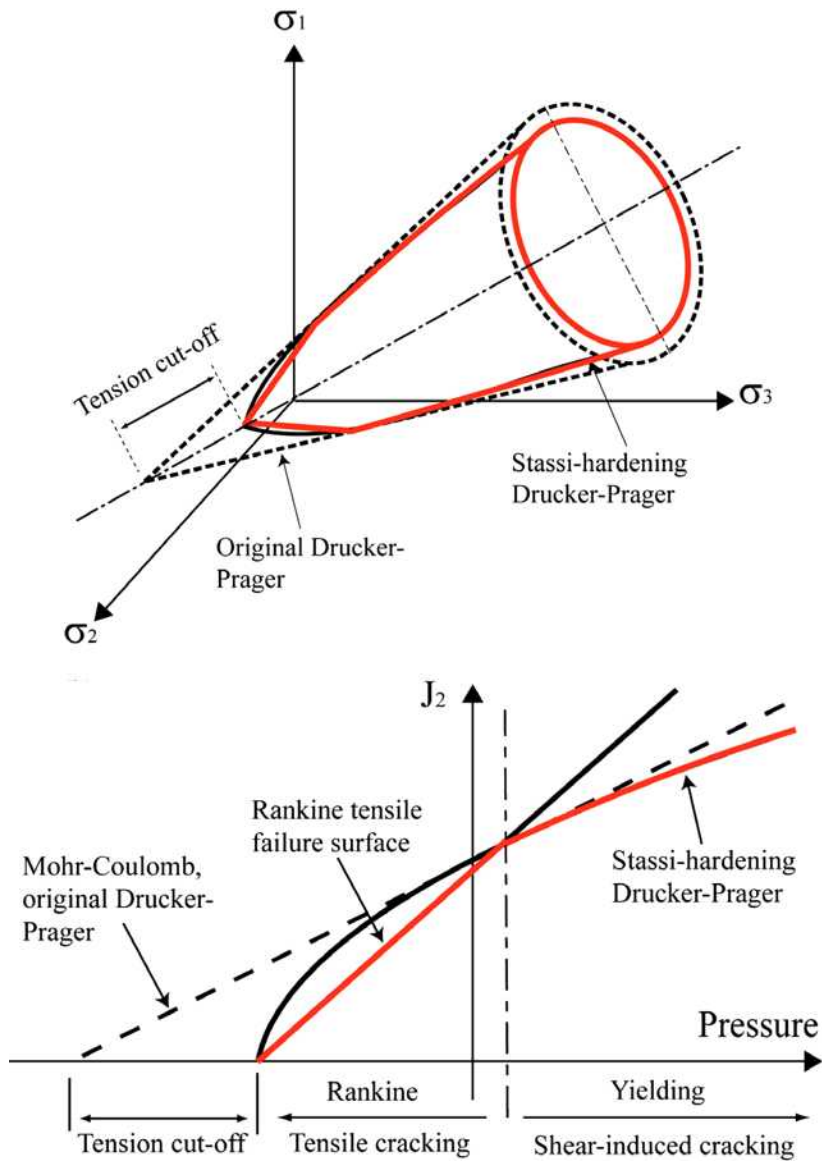


Figure 6.4 Description of the Drucker-Prager model with Stassi-hardening function (After Cho et al. 2010)

The stress and strain based model are based on the mechanical parameters and its strengths of the rock. The stresses and strains of each element are numerically calculated in the computation process, and the element reaches failure if it exceeds the predetermined strength and the strain criteria.

The damage based model, on the other hand, is a method of calculating the damage of a material based on the plastic strain in the plastic strain region (the stress level is above the yield stress of the material) according to defined function. The damage factor is calculated by the plastic strain in computation process, and it reduces the elastic modulus and yield strength based on the damage. The level of damage is used to define the failure of the material.

The strength and failure models based on the damage of material are Johnson and Cook (JC), Johnson and Holmquist (JH), RHT (Riedel, Hiermaier, and Thoma) concrete model (Riedel et al., 1999; Riedel 2000), the cumulative damage (CD) model, etc. Of the failure models, only cumulative damage model can be used with the different strength model; in other models, the strength model and the failure model should be defined with the same model. The RHT concrete model is suitable for the modeling of brittle materials such as concrete and rock, however only input parameters for limited compressive strength (35 and 140 MPa) of concrete have been suggested. Therefore, the input parameters should be estimated in other strength material using the parameters used for the two strengths of concrete. In this study, the CD failure criterion was used to describe the material failure in rock cutting.

The cumulative damage, CD model (Persson, 1990) can be used to

describe the macroscopic inelastic behavior of material such as ceramics and concrete where the strength of the material can be significantly degraded by crushing. In rock cutting, Since the area between the adjacent cutters where chipping can occur is damaged by the preceding cutting, the application of the cumulative damage model is considered as reasonable.

The cumulative damage model computes a damage factor (D) to model the progressive crushing and subsequent weakening of the materials. The parameter D which is zero for all plastic deformation for which the effective plastic strain is less than a value $EPS1$. When the strain reaches a value of $EPS1$, the damage parameter D increases linearly with strain up to a maximum value D_{max} (<1) at a value of the effective plastic strain $EPS2$, as shown in figure 6.5 (Century Dynamics, 2005, 2011)

$$D = D_{MAX} \left(\frac{EPS - EPS1}{EPS2 - EPS1} \right) \quad (6.2)$$

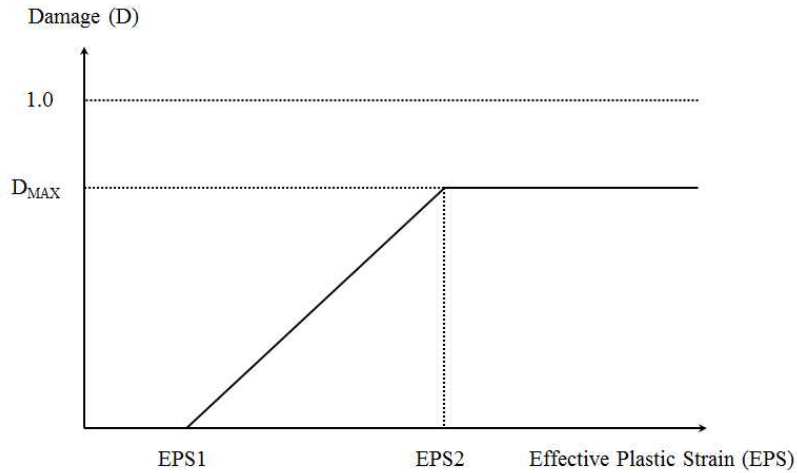


Figure 6.5 Cumulative damage as a function of effective plastic strain (After Century Dynamics, 2005)

The current value of the damage factor (D) modify the bulk modulus, shear modulus and yield strength of the material. The yield strength (Y) is reduced to Y_{dam} according to the damage factor. If the hydrostatic pressure is positive (compressive), the reduced yield strength is defined as equation 6.3.

$$Y_{dam} = Y(1 - D) \quad (6.3)$$

If the hydrostatic pressure is negative (tension), the reduced yield strength is defined as equation 6.4, and these reduced function are presented in figure 6.6.

$$Y_{dam} = Y\left(1 - \frac{D}{D_{MAX}}\right) \quad (6.4)$$

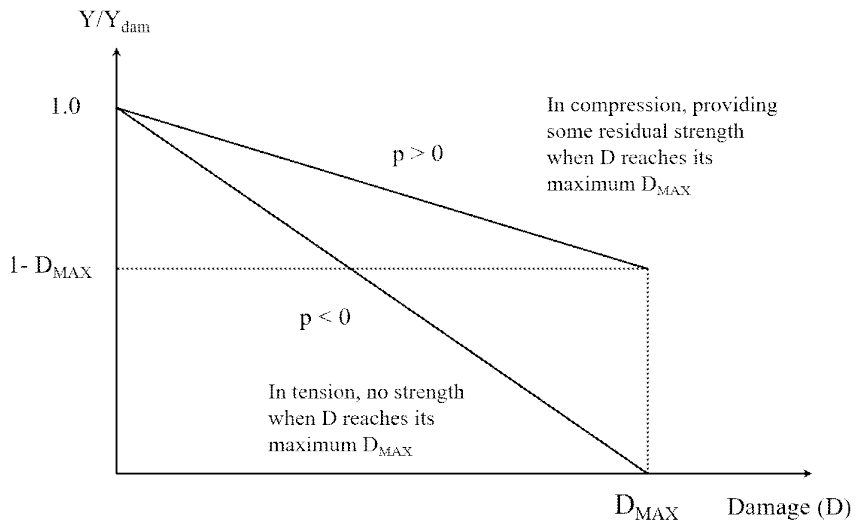


Figure 6.6 The yield stress as a function of cumulative damage model (Modified from Century Dynamics, 2005)

On the other hand, the bulk modulus and shear modulus are unaffected in compression, while in tension they are progressively reduced to zero when damage is complete. In tension, therefore, they are both reduced by the damage factor (Figure 6.7).

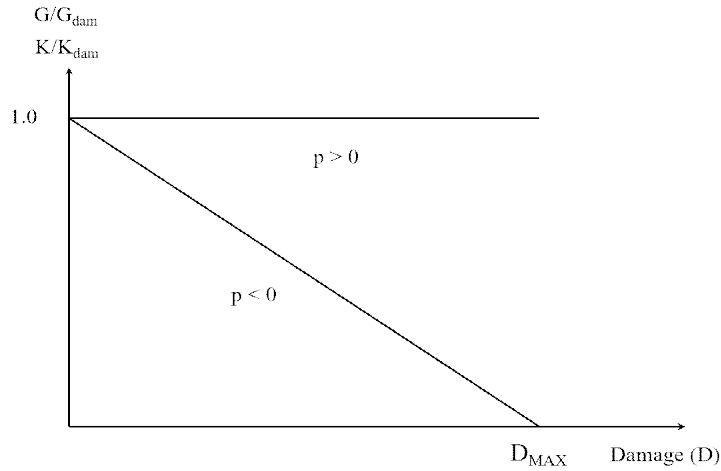


Figure 6.7 Bulk and shear modulus as functions of cumulative damage model (Modified from Century Dynamics, 2005)

The input parameters represents the failure behavior of rock in numerical simulation. Therefore, the parameters can affect the numerical results (i.e., cutter forces and cutting volume). The sensitivity analysis was carried out to investigate the effect of the input parameters (i.e., *EPS1* and *EPS2*) of failure model on the results, and to determine the values for the Linyi sandstone and concrete.

Table. 6.3 Input parameters and their factor levels for sensitivity analysis

Parameters	Factor Levels		
	A	B	C
<i>EPS1</i>	0.05	0.075	0.1
<i>EPS2</i>	0.5	1.0	1.5

Table. 6.4 Design matrix for the full factorial design

Cases	<i>EPS1</i>	<i>EPS2</i>
1	A	A
2	B	A
3	C	A
4	A	B
5	B	B
6	C	B
7	A	C
8	B	C
9	C	C

**EPS1* and *EPS2* are the input parameters of cumulative failure model, represents effective plastic strain at the damage of material is zero and maximum, respectively.

The numerical results, the cutting force, the normal force and specific energy were obtained in each case, and they are summarized in Table 6.5. The effect of the input parameters on the cutter forces and the specific energy were analyzed by Spearman correlation matrix and Pearson correlation matrix, and they summarized in Table 6.6 and 6.7. The Spearman and Pearson correlation coefficients indicate the degree of nonlinear and linear relationships between the variables.

Table. 6.5 The results of numerical simulation for sensitivity analysis

Cases	Cutting force, F_{c_mean} (kN)			Normal force, F_{n_mean} (kN)			Specific energy, SE (MJ/m ³)
	1	2	Avg.	1	2	Avg.	
1	6.01	5.17	5.59	2.88	2.93	2.91	13.68
2	5.63	5.13	5.38	2.78	2.63	2.71	12.67
3	5.54	5.12	5.33	2.86	2.73	2.80	12.10
4	6.52	5.72	6.12	3.52	3.34	3.43	26.48
5	6.31	5.61	5.96	3.48	3.18	3.33	23.97
6	6.08	5.51	5.80	3.34	3.35	3.35	22.67
7	6.62	5.93	6.28	3.66	3.42	3.54	54.91
8	6.39	5.78	6.01	3.52	3.25	3.39	49.40
9	6.73	5.92	6.33	3.75	3.41	3.58	48.72

Table 6.6 The Spearman correlation matrix of the input parameters and results of numerical simulation

Spearman coefficient	F_{c_mean}	F_{n_mean}	SE
<i>EPS1</i>	-0.21	-0.11	-0.32
<i>EPS2</i>	0.90	0.90	0.95
<i>EPS2/EPS1</i>	0.88	0.85	0.98

Table 6.7 The Pearson correlation matrix of the input parameters and results of numerical simulation

Pearson coefficient	F_{c_mean}	F_{n_mean}	SE
<i>EPS1</i>	-0.21	-0.07	-0.10
<i>EPS2</i>	0.93	0.92	0.97
<i>EPS2/EPS1</i>	0.87	0.81	0.89

Table 6.8 Input parameters of Linyi sandstone and concrete for rock model

Model	Parameter	Input value (Linyi sandstone)	Input value (Concrete)
Linear (EOS)	Density (g/cm ³)	2.41	2.29
	Bulk Modulus (kPa)	5.67e ⁶	1.24e ⁷
	Reference temperature (K)	Room temperature	293
Drucker-Prager (Strength)	Shear Modulus (kPa)	4.25e ⁶	1.07e ⁷
	Pressure hardening type	Stassi	Stassi
	Yield stress in Tension	4.23e ³	2.15e ³
	Yield stress in Compression	5.76e ⁴	1.89e ⁴
Cumulative damage (Failure)	Plastic strain (D = 0)	0.10	0.03
	Plastic strain (D = max)	1.0	0.7
	Maximum damage factor	0.99	0.99
	Erosion	None	None
	Minimum density Cut-off (SPH)	0.2 (default)	0.2 (default)
	Maximum density Cut-off (SPH)	1.0 (default)	1.0 (default)
	Maximum sound speed (m/s)	10000	10000

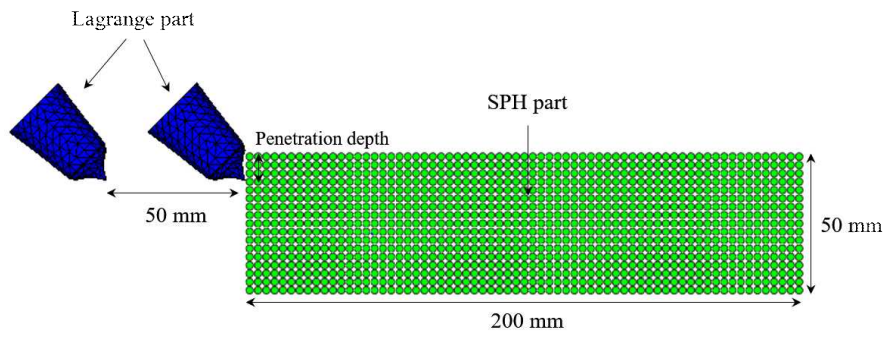
(2) Dimension of rock model

In this study, a rock model is modeled as a cube. The size of the rock model was determined as 200 mm × 100 mm × 50 mm. The particle size of the rock model was 3 mm, and the number of particles was about 38000. Based on the results of the numerical simulation, the rock thickness of 50 mm was sufficient to simulate the cutting conditions considered in this study.

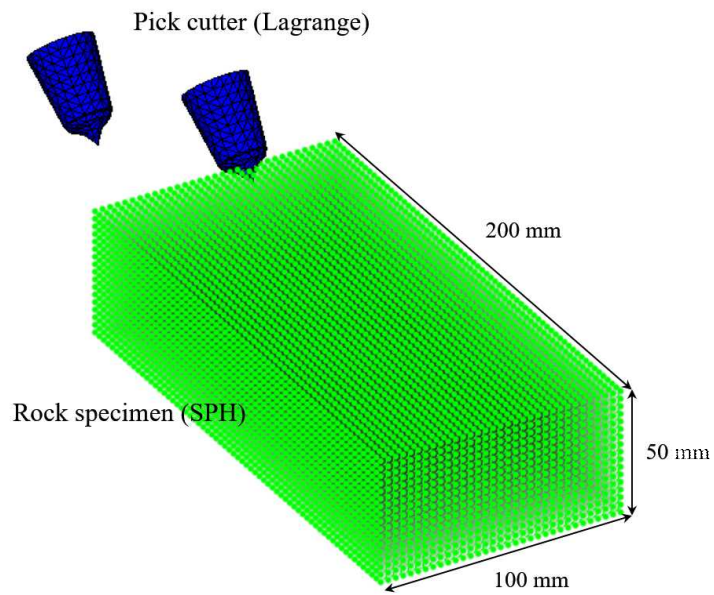
6.3.3 Rock cutting Model

The bottom surface of the rock model was constrained as fixed boundary condition to prevent displacement in all direction, and both sides of the rock model were constrained with roller boundary. The cutter linearly moves to cutting direction by the constant velocity (10 m/s) boundary condition to simulate the linear rock cutting in trencher or LCM test.

In this study, two cutters sequentially move and cut the rock model to observe the interaction between adjacent pick cutters. The line spacing was fixed as 50 mm, and the numerical model used in this study is described in figure 6.8.



(a) Side view



(b) Isometric view

Figure 6.8 The rock cutting model used in this study

6.3.4 Analysis of numerical results

The estimation of the cutter force acting on the pick cutter and the cut rock volume is important to assess the cutting efficiency. In AUTODYN, the contact force between the different parts (external contact force) is automatically calculated in the computational process and stored. Therefore, the three directional cutter forces acting on the pick cutter can be obtained by measuring the contact force between the rock model (SPH) and the pick cutter model (Lagrangian) during the pick cutter cut the rock model. In this numerical model, the volume of the cut rock was calculated by counting the fragmented particles which reach to the maximum damage after the cutting was finished.

6.4 Numerical simulation

6.4.1 Cutting conditions

The results of the numerical simulations for the Linyi sandstone and concrete were summarized in Table 6.9. The different penetration depths and cut spacings were considered where the attack angle and skew angles were set as 45° and 0° , respectively.

Table 6.9 The cutting conditions and results of numerical simulation

Rock type	p	S	Mean cutting force, F_{c_mean} (kN)		Mean normal force, F_{n_mean} (kN)		Specific energy (MJ/m ³)	
			LCM	Numerical	LCM	Numerical	LCM	Numerical
Linyi sandstone	5	5	3.23	2.84	3.63	2.94	82.96	57.89
		10	4.21	4.61	4.41	3.04	77.65	60.45
		15	5.19	4.80	5.29	4.31	77.86	53.08
		20	5.78	4.80	5.88	4.90	67.57	41.05
		25	6.37	5.00	6.47	5.10	85.81	50.66
	7	7	3.53	4.80	3.53	3.33	54.74	53.00
		14	5.10	5.78	5.10	4.41	48.94	45.67
		21	6.17	6.66	6.86	5.00	42.17	40.99
		28	6.96	6.57	7.25	4.80	44.94	49.00
		35	-	7.06	-	5.39	-	52.42
	9	9	5.00	8.82	5.68	4.12	49.73	57.94
		18	6.66	9.21	7.94	7.35	37.69	49.88
		27	7.55	9.41	9.41	10.49	33.12	42.80
		36	8.33	9.70	10.98	8.72	39.70	53.76
		45	-	9.02	-	13.82	-	52.86

		11	6.96	11.76	7.25	6.96	46.30	55.46
	11	22	7.94	12.25	8.43	8.62	34.39	43.10
		33	8.92	10.78	9.60	11.17	31.10	46.32
		44	10.00	10.58	12.94	10.58	32.71	45.40
		13	-	14.11	-	7.45	-	57.98
	13	26	-	14.21	-	9.41	-	50.93
		39	-	17.74	-	13.33	-	60.45
		45.5	-	13.43	-	12.25	-	67.71
		15	2.55	2.16	1.76	1.86	31.88	31.70
		20	2.84	2.25	1.96	1.96	29.43	28.51
Concrete	5	25	3.23	2.35	2.55	1.96	33.69	26.01
		30	3.82	2.45	2.84	2.06	37.07	30.91
		35	3.82	5.39	2.74	2.16	40.62	36.02

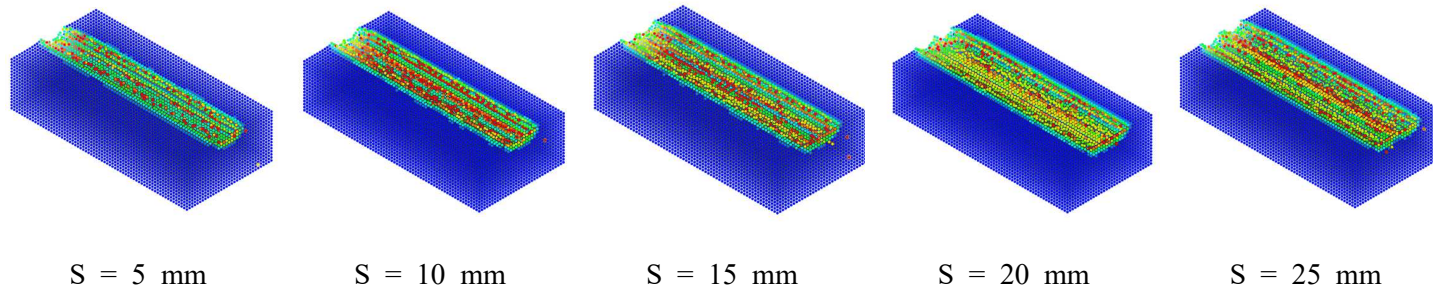
6.4.2 Fragmentation patterns

In the numerical analysis performed in this study, crack propagation and fragmentation behavior of rocks are represented by the damage level of each element. The elements which reach 0.99 of damage indicate that the element is failed according to the failure criterion (Cumulative damage).

Figures 6.9 - 6.13 show the fragmentation patterns of Linyi sandstone under different cut spacings and penetration depths, and figure 6.15 shows the that of concrete. The figures clearly show that the failed (chipping) area becomes larger as the cut spacing increases in the same penetration depth. The apparent optimum cut spacings at the different penetration depth is 20 mm ($p = 5$ mm), 21 mm ($p = 7$ mm), 27 mm ($p = 9$ mm), 22 mm ($p = 11$ mm), 26 mm ($p = 13$ mm) respectively. In the case of the concrete, the apparent optimum cut spacing is 25 mm. As the results of fragmentation patterns, the numerical model simulates well the rock cutting process by the pick cutter.

At these cut spacings, it is confirmed that the cutting area (failed region) is maximized by the interaction between the adjacent cutters. Also, it is confirmed that the ridge remains between the adjacent cutters above the optimum cut spacing, while in the case of spacing below the optimum cut spacing.

(a) Isometric view (without the failed particles)



(b) Top View (with the failed particles)

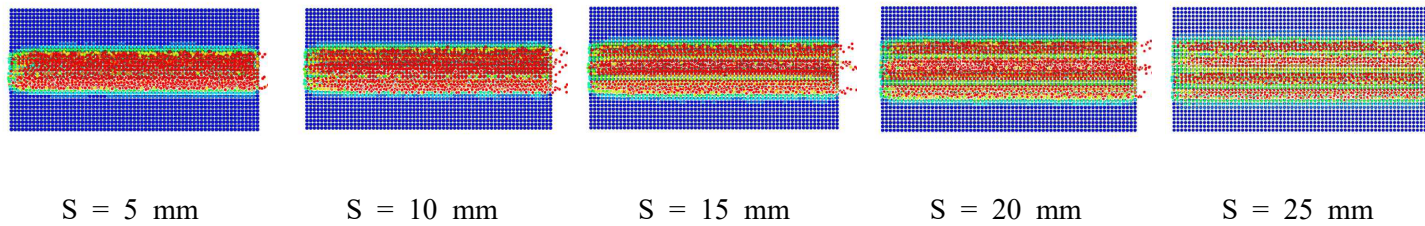
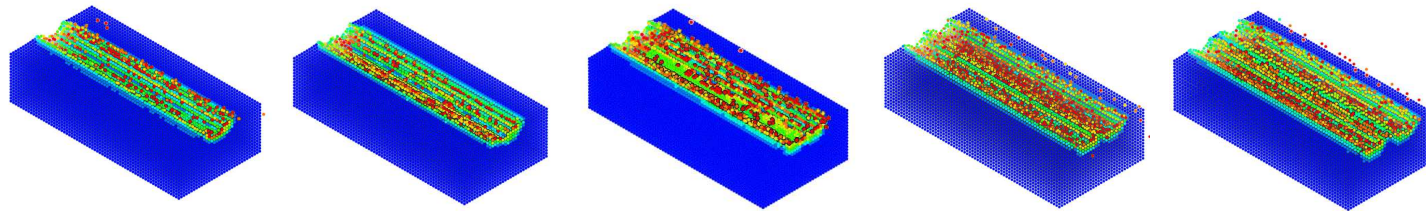


Figure 6.9 The fragmentation patterns in Linyi sandstone at the different cut spacing ($p = 5$ mm)

(a) Isometric view (without the failed particles)



S = 7 mm

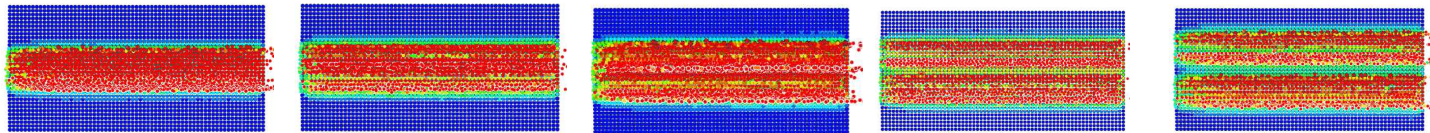
S = 14 mm

S = 21 mm

S = 28 mm

S = 35 mm

(b) Top View (with the failed particles)



S = 7 mm

S = 14 mm

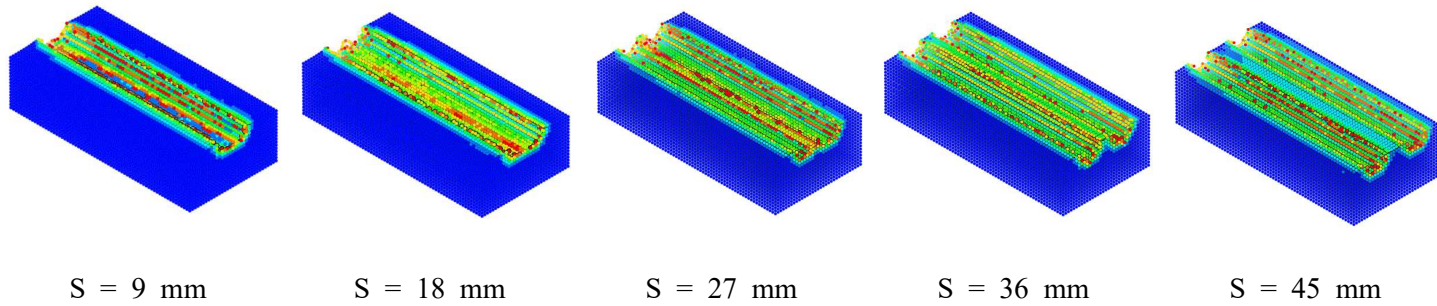
S = 21 mm

S = 28 mm

S = 35 mm

Figure 6.10 The fragmentation patterns in Linyi sandstone at the different cut spacing ($p = 7$ mm)

(a) Isometric view (without the failed particles)



(b) Top View (with the failed particles)

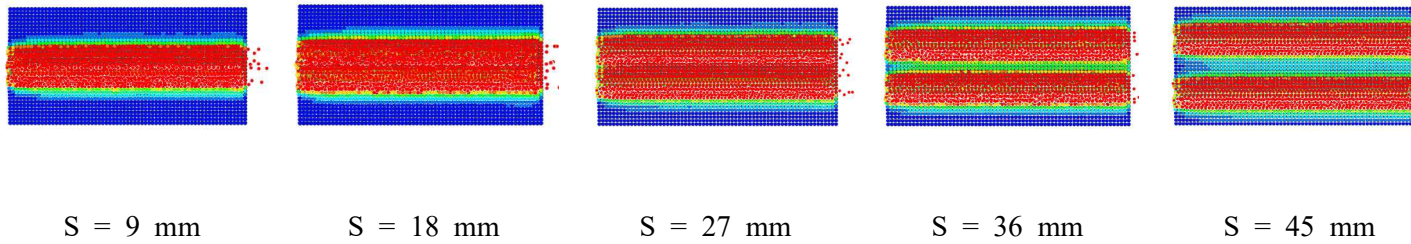
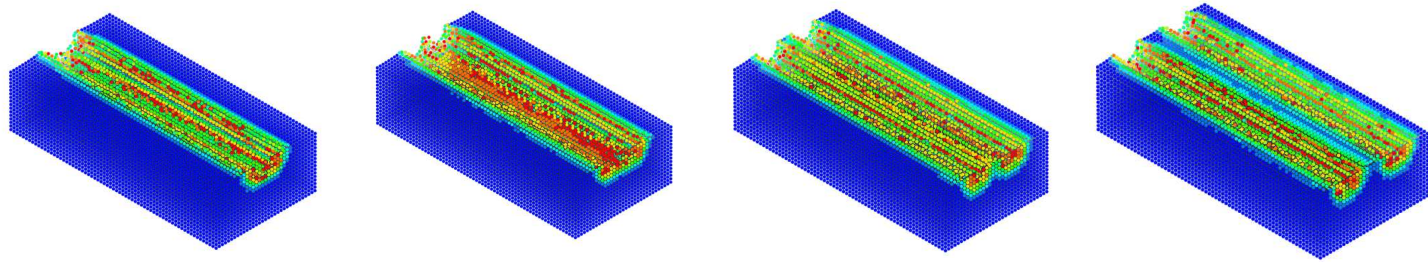


Figure 6.11 The fragmentation patterns in Linyi sandstone at the different cut spacing ($p = 9$ mm)

(a) Isometric view (without the failed particles)



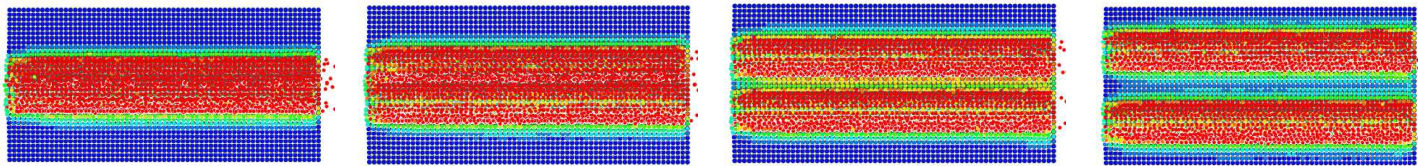
$s = 11$ mm

$S = 22$ mm

$S = 33$ mm

$S = 44$ mm

(b) Top View (with the failed particles)



$s = 11$ mm

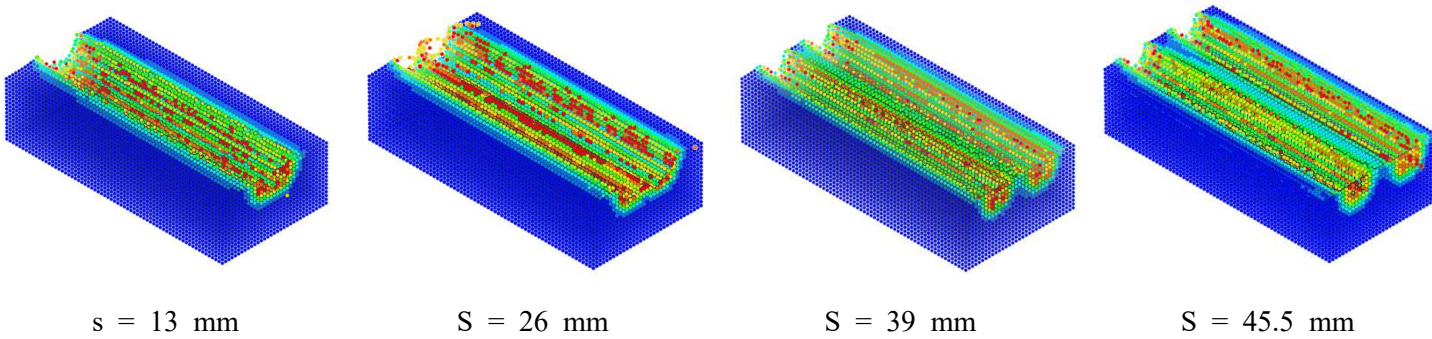
$S = 22$ mm

$S = 33$ mm

$S = 44$ mm

Figure 6.12 The fragmentation patterns in Linyi sandstone at the different cut spacing ($p = 11$ mm)

(a) Isometric view (without the failed particles)



(b) Top View (with the failed particles)

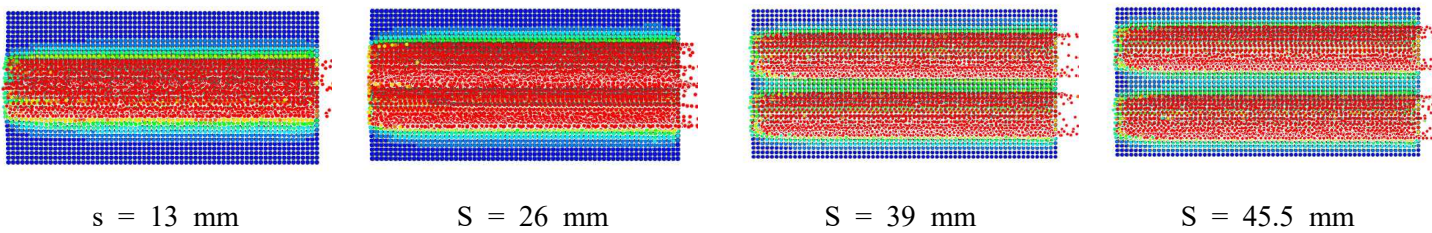
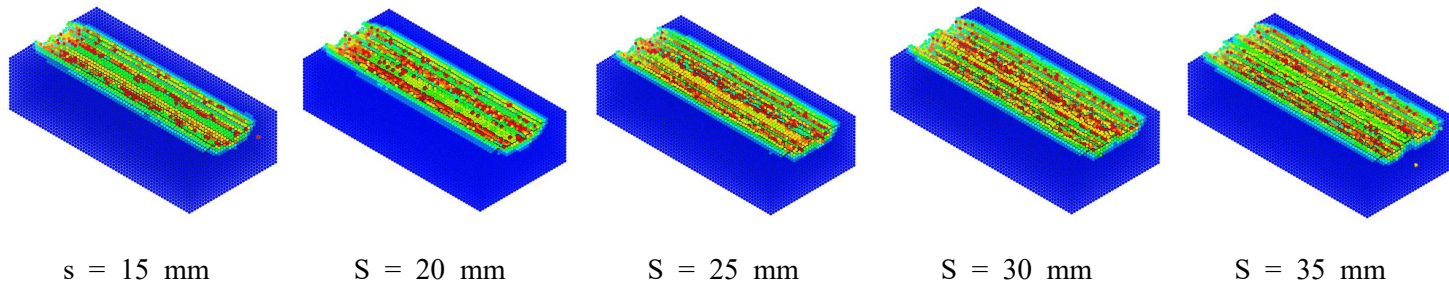


Figure 6.13 The fragmentation patterns in Linyi sandstone at the different cut spacing ($p = 13 \text{ mm}$)

(a) Isometric view (without the failed particles)



(b) Top View (with the failed particles)

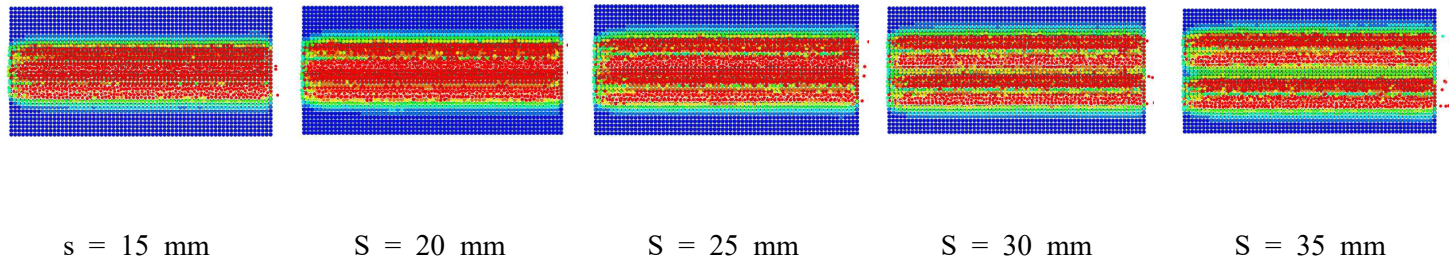
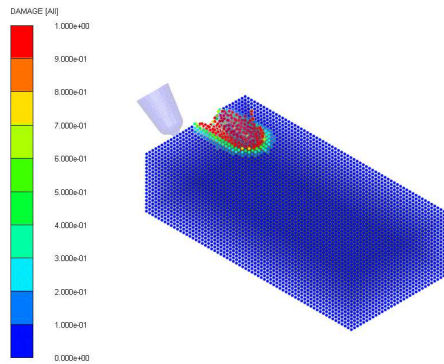
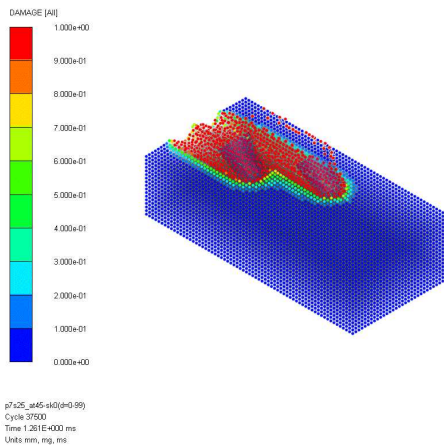


Figure 6.14 The fragmentation patterns in concrete at the different cut spacing ($p = 5$ mm)

Figure 6.15 (a) and (b) show the damage cumulating process by the interaction of adjacent cutters at the optimum cut spacing. The area between the two cutters which was damaged by the first cutter was again damaged by the second cutter and was failed. However, if the cut spacing is larger than the optimum cut spacing, the damaged area was limited as shown in figure 6.16.

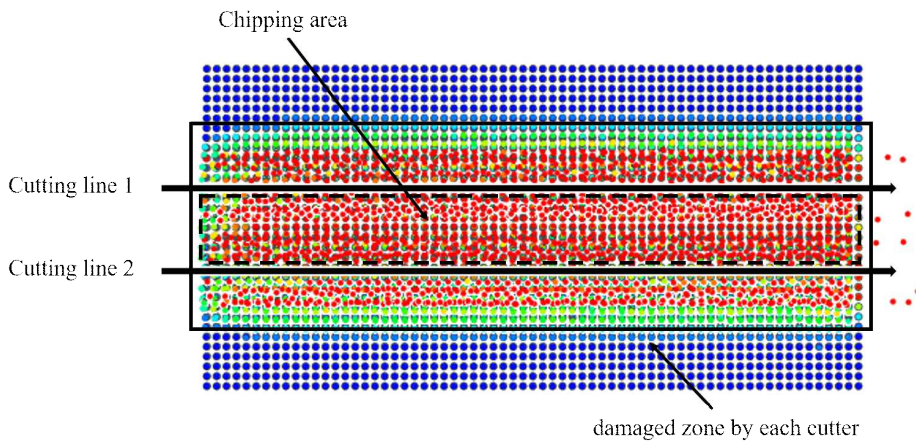


(a) first cutting

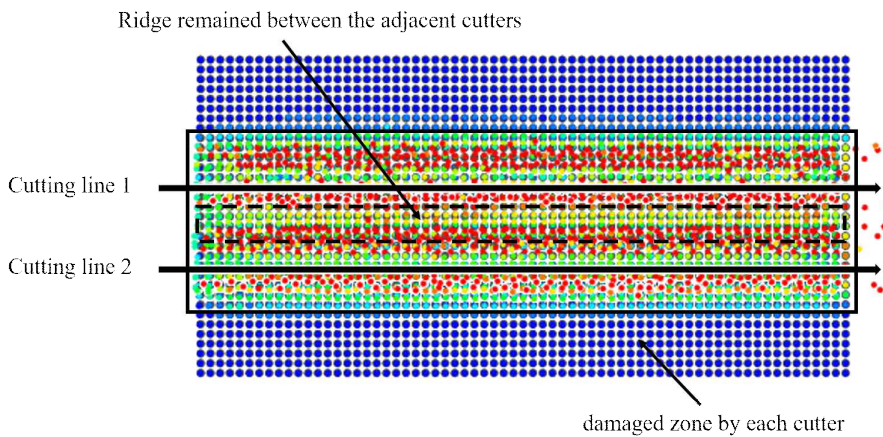


(b) second cutting

Figure 6.15 The crack generation due to interaction of adjacent cutters



(a) at the optimum cut spacing



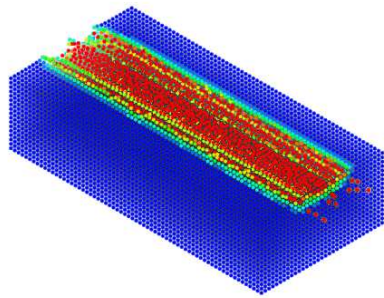
(b) at the cut spacing is larger than optimum cut spacing

Figure 6.16 The interaction between the adjacent cutters in numerical simulation at the different cut spacing condition

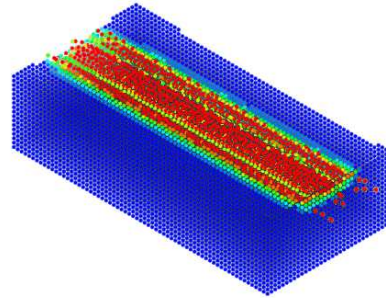
Figure 6.17 shows the damage contour of the cut surface after cutting at the different height of the rock model ($p = 5$ mm and $s = 20$ mm). The crack propagation length is represented by the range of the damaged

particles in the vertical direction when the 5 mm of penetration depth is 10 mm. Figure 6.18 shows the maximum principal stress and stress in the vertical direction. The high compressive stressed region appears beneath the pick cutter. This is one of the proofs that the numerical model applied in this study accurately simulate the cutting process of rock.

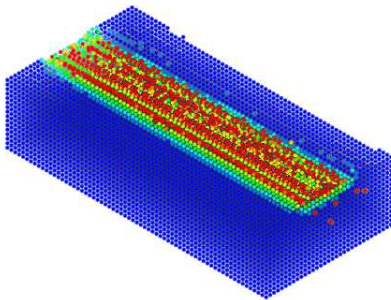
As mentioned in chapter 2. Although the crushing process and crushed zones were successfully simulated using partial modeling, it is difficult to explain that the problem of FEM is fundamentally solved. On the other hand, SPH numerical model proposed in this study seems to simulate the crushing process (crushed zone) in rock cutting based on the results above.



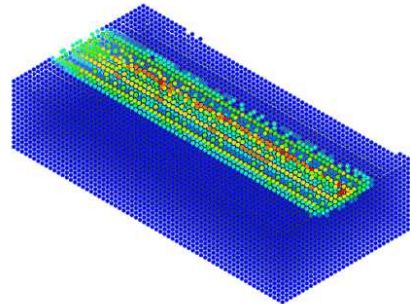
Surface



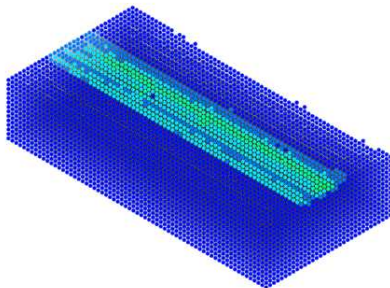
0.5 mm



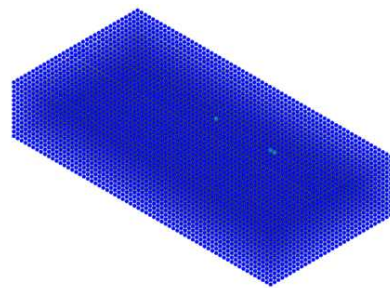
3.5 mm



6.5 mm

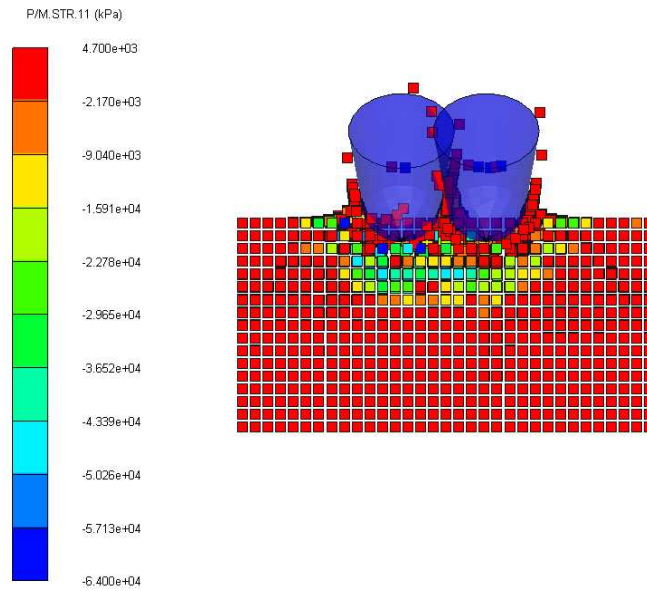


9.5 mm

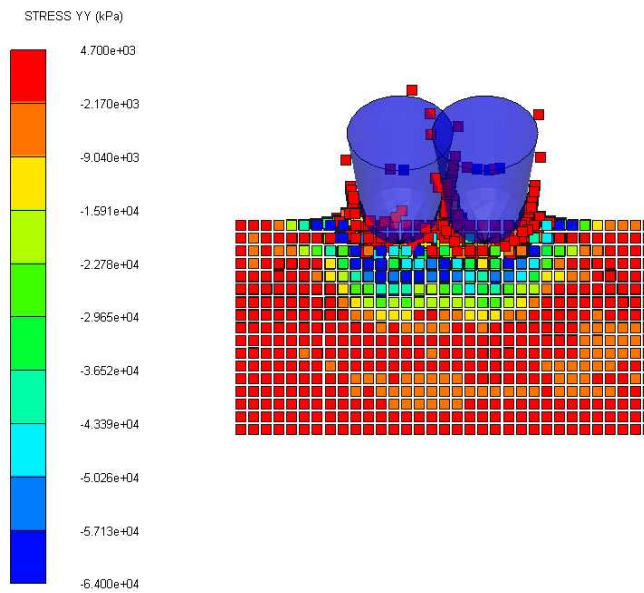


10 mm

Figure 6.17 The damage contour at the different height of the rock model
(cutting condition : $p = 5$ mm, $s = 20$ mm)



(a)



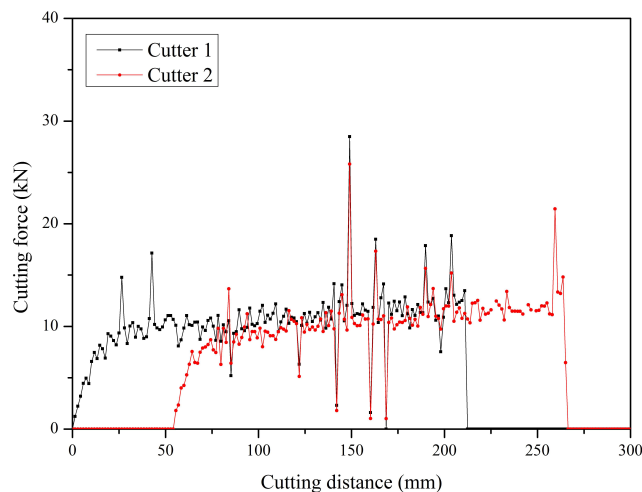
(b)

Figure 6.18 The distribution of (a) maximum principal stress and (b) stress in vertical direction (cutting condition : $p = 5 \text{ mm}$, $s = 20 \text{ mm}$)

6.4.2 Cutter forces

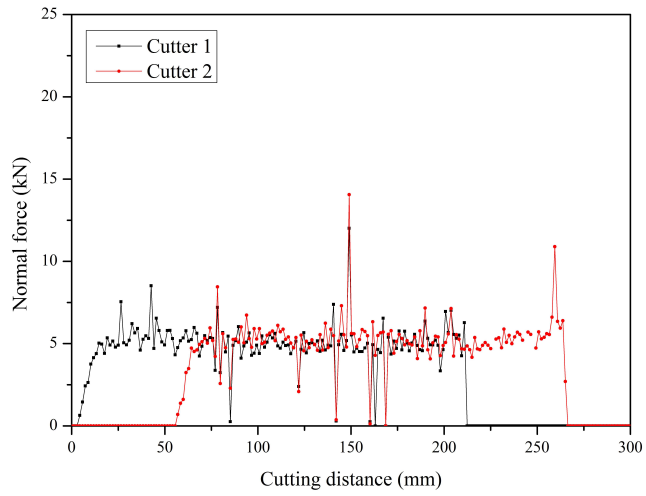
Figure 6.19 shows the representative cutter forces obtained from the numerical simulation (cutting condition is $p = 11$ mm and $s = 11$ mm). In the numerical analysis, the force of the first cutter and the second cutter are almost equal if the two cutters are apart a certain spacing (within relieved cut spacing). However, if the cutter spacing is too narrow, the force of the second cutter is reduced.

The force of the first cutter did not show a significant difference according to the cut spacing. Therefore, the mean force of the cutter in the numerical analysis is represented by the cutter force acting on the second cutter.

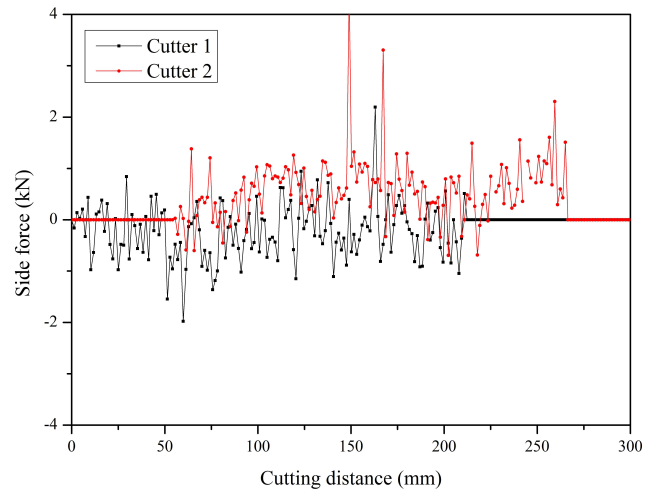


(a) Cutting force

Figure 6.19 The representative cutter force obtained from the numerical simulation



(b) Normal force

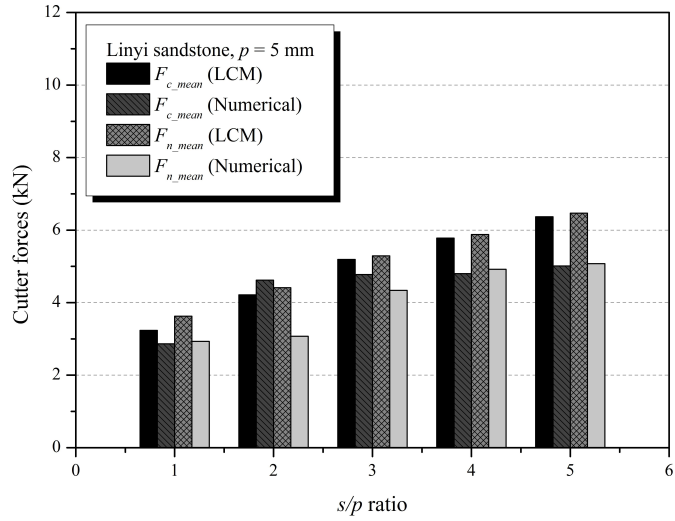


(c) Side force

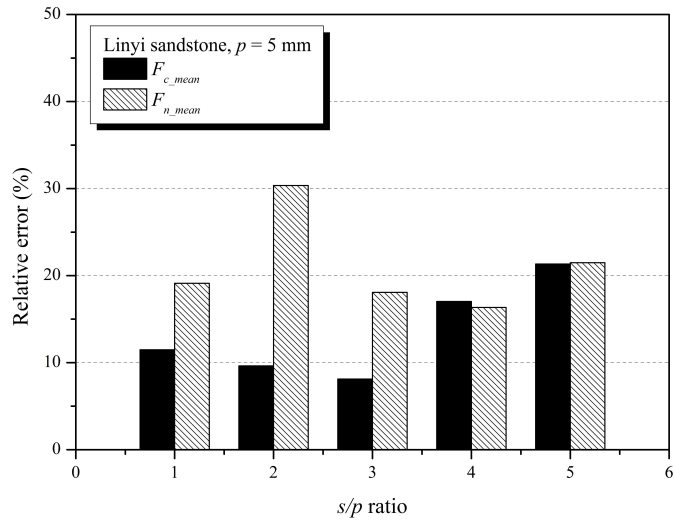
Figure 6.19 (Continued)

(A) Linyi sandstone, penetration depth = 5 mm

Figure 6.20 shows the comparison results of the cutter forces in LCM with numerical simulation according to the cutter spacing at the 5 mm of penetration depth. The numerical simulation slightly underestimates both the cutting force and the normal force compared to LCM result. The relative error of the cutting force and normal force between the LCM and numerical simulation were 13.5% (8.1 ~ 21.3%) and 21% (16.3 ~ 30.4%).



(a) Cutter forces

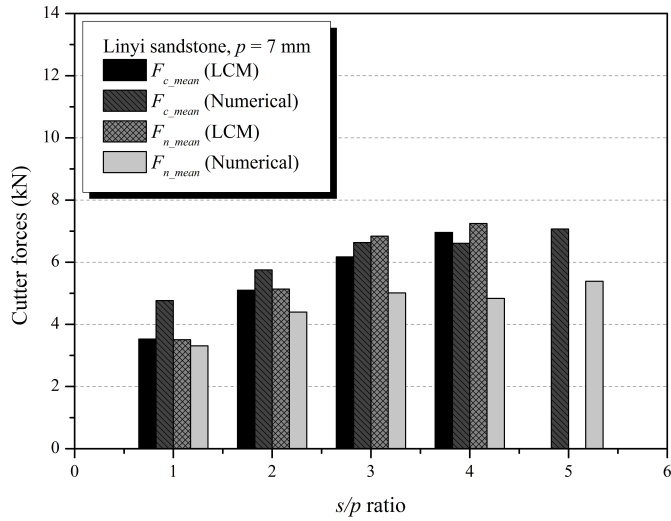


(b) Relative error

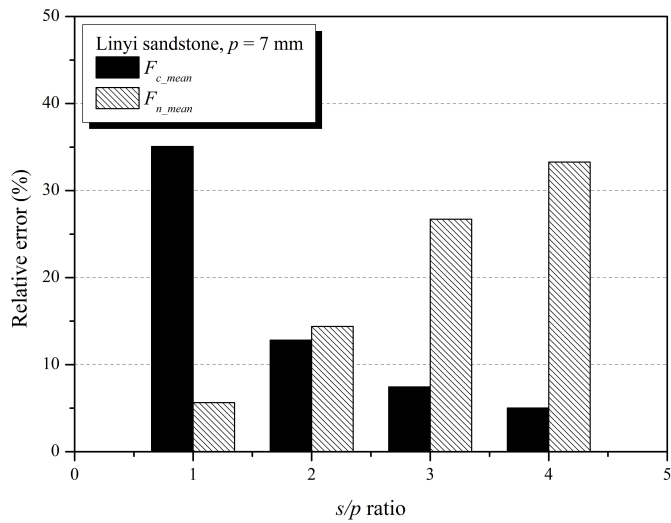
Figure 6.20 The comparison of the cutter force between the LCM and the numerical simulation (Linyi sandstone, $p = 5$ mm)

(B) Linyi sandstone, penetration depth = 7 mm

Figure 6.21 shows the comparison results of the cutter forces in LCM with numerical simulation according to the cutter spacing at the 7 mm of penetration depth. The numerical simulation slightly overestimates the cutting force and underestimates the normal force compared to LCM result. The relative error of the cutting force and normal force between the LCM and numerical simulation were 15.1% (5.0 ~ 35.0%) and 20.3% (5.0 ~ 33.3%).



(a) Cutter forces

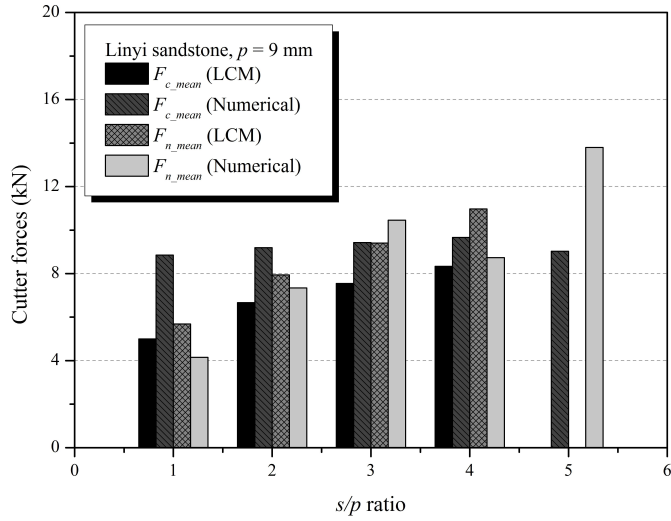


(b) Relative error

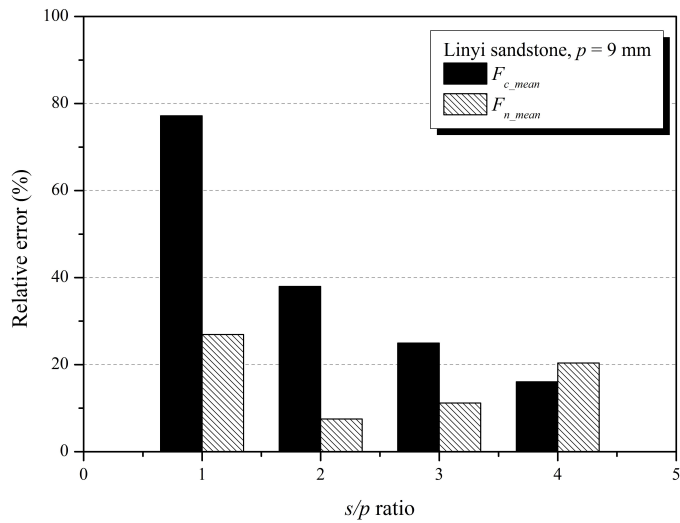
Figure 6.21 The comparison of the cutter force between the LCM and the numerical simulation (Linyi sandstone, $p = 7$ mm)

(C) Linyi sandstone, penetration depth = 9 mm

Figure 6.22 shows the comparison results of the cutter forces in LCM with numerical simulation according to the cutter spacing at the 9 mm of penetration depth. The numerical simulation significantly overestimates the cutting force. The maximum relative error of the cutting force was of the cutting force 77.2% at the 9 mm of cut spacing. The relative errors of the cutting force and normal force between the LCM and numerical simulation were 39.0% (16.0 ~ 77.2%) and 16.5% (11.1 ~ 26.9%).



(a) Cutter forces

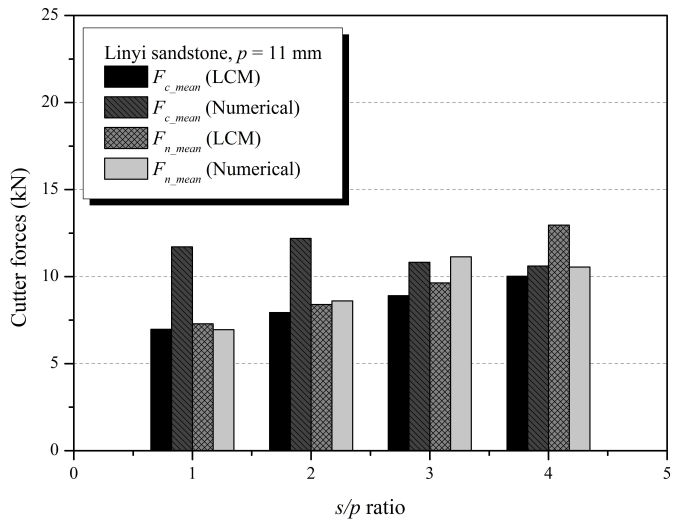


(b) Relative error

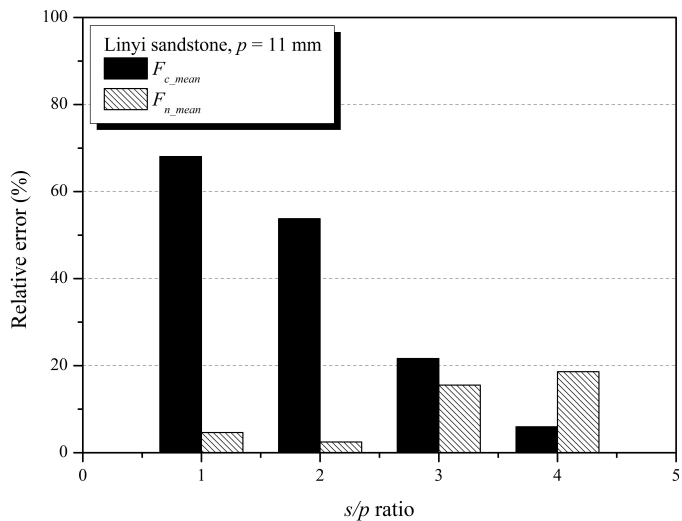
Figure 6.22 The comparison of the cutter force between the LCM and the numerical simulation (Linyi sandstone, $p = 9$ mm)

(D) Linyi sandstone, penetration depth = 11 mm

Figure 6.23 shows the comparison results of the cutter forces in LCM with numerical simulation according to the cutter spacing at the 11 mm of penetration depth. The numerical simulation significantly overestimates the cutting force at the 11 mm and 22 mm of cut spacings. The relative errors at these cut spacings were 68.0% and 53.8%, respectively. However, the normal force of numerical simulation showed good agreement with the LCM results for all cut spacings. On average, the relative error of the cutting force and normal force in the LCM and numerical simulations were 37.5% (6.0 ~ 68.0%) and 10.3% (2.5 ~ 18.6%), respectively.



(a) Cutter forces

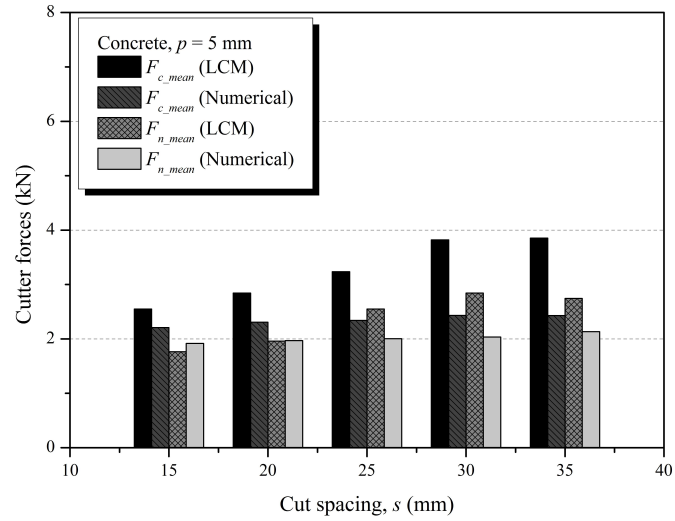


(b) Relative error

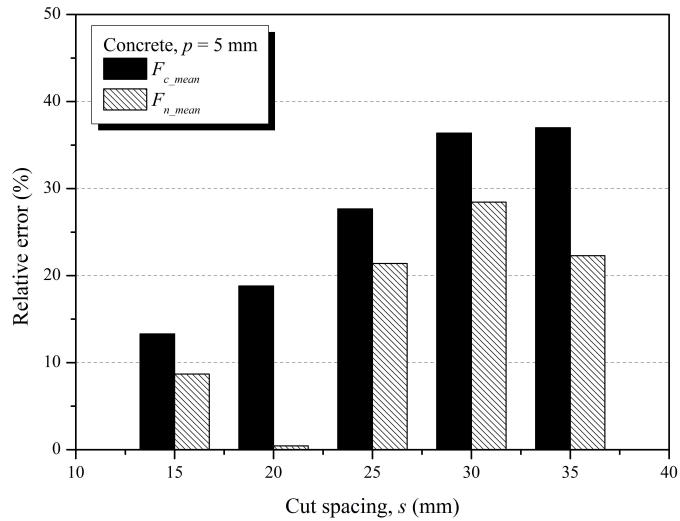
Figure 6.23 the comparison of the cutter force between the LCM and the numerical simulation (Linyi sandstone, $p = 11$ mm)

(E) Concrete, penetration depth = 5 mm

On the other hand, Figure 6.24 shows the comparison of the results of the cutter forces in the LCM and numerical simulation. The numerical results of concrete showed that both the normal force and cutting force were underestimated for all cut spacing. The relative errors of the normal force and cutter force are 12% (9.9 ~ 28.7 %) and 26.6% (13.5 ~ 36.8%), respectively, on average.



(a) Cutter forces



(b) Relative error

Figure 6.24 the comparison of the cutter force between the LCM and the numerical simulation (Concrete, $p = 5$ mm)

6.4.3 Specific energy

(A) Linyi sandstone, penetration depth = 5 mm

Figure 6.25 shows the comparison result of the specific energy obtained from the LCM and numerical simulation at 5 mm of penetration depth. As a result, it is confirmed that the optimum cut spacing in numerical simulation is 20 mm which is same with that in the LCM test. It is already shown in the analysis of the fragmentation pattern in numerical simulation. The optimum cut spacing is same with each other. However, the numerical simulation underestimates the specific energy compared with the LCM test. This is probably due to the difference in cutting force.

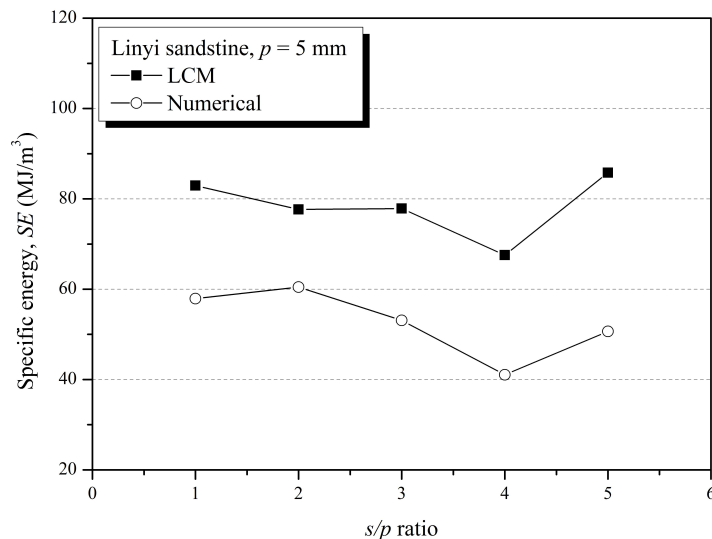


Figure 6.25 The comparison of the specific energy between the LCM and the numerical simulation (Linyi sandstone, p = 5 mm)

(B) Linyi sandstone, penetration depth = 7 mm

At 7 mm of penetration depth, as shown in figure 6.26, the optimum cut spacing in numerical simulation is 21 mm which is same with that in the LCM test. The optimum cut spacing is same with each other, and the specific energy obtained from the numerical simulation showed good agreement with the LCM test.

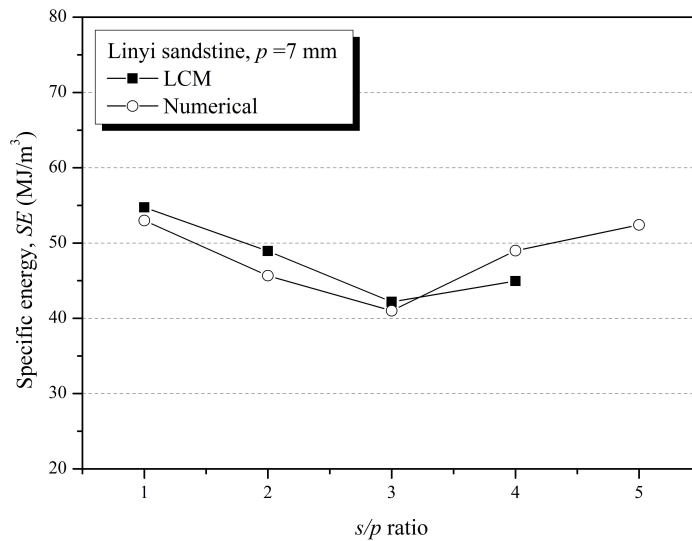


Figure 6.26 The comparison of the specific energy between the LCM and the numerical simulation (Linyi sandstone, $p = 7$ mm)

(C) Linyi sandstone, penetration depth = 9 mm

In the case of 9 mm of penetration depth, the optimum cut spacing in numerical simulation is 27 mm, and it is same with that of the LCM test (Figure 6.27). The specific energies obtained from the numerical simulation

at 9 mm of penetration depth is larger than those of the LCM test. The reason is that the cutting force in the numerical simulation is measured higher than LCM.

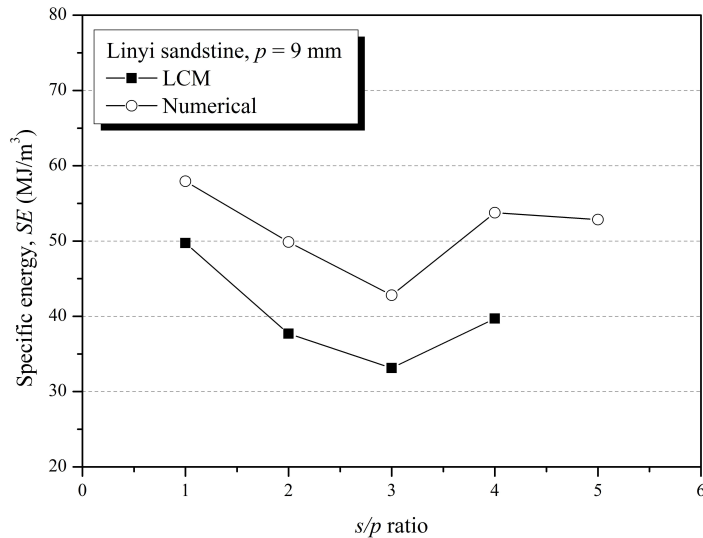


Figure 6.27 The comparison of the specific energy between the LCM and the numerical simulation (Linyi sandstone, $p = 9$ mm)

(D) Linyi sandstone, penetration depth = 11 mm

At the above penetration depths, the optimum cut spacings in the numerical simulation were the same with that of the LCM. However, at the 11 mm of penetration depth, the optimum cut spacing in the numerical simulation was 22 mm, while the optimum cut spacing was 33 mm is the LCM. As shown in figure 6.28, the optimum cut spacing is 33 mm if the optimum cutter spacing is defined as the minimum point of specific energy.

However, in the LCM, since the specific energy tends to converge after the 22 mm of cut spacing, it is not easy to determine the optimum cut spacing clearly. Therefore, the result of the optimum cut spacing obtained from the numerical simulation is reasonable. Since the cutting force is overestimated (figure 6.23), the specific energy of the numerical simulation is also higher than that of LCM.

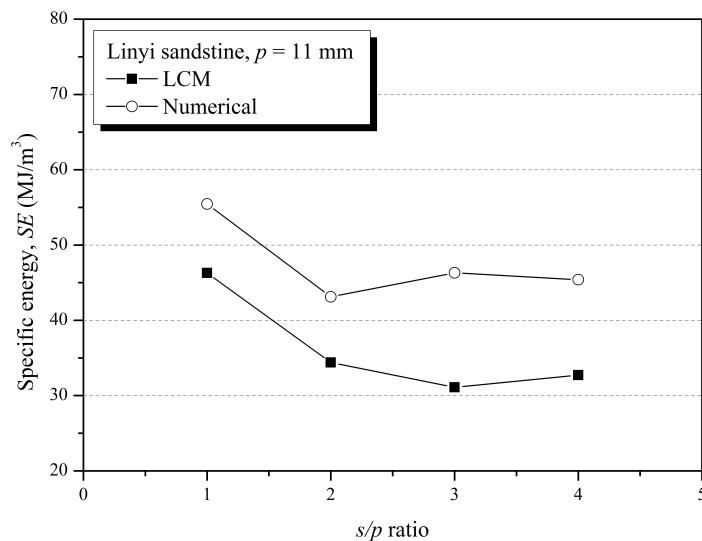


Figure 6.28 The comparison of the specific energy between the LCM and the numerical simulation (Linyi sandstone, $p = 11$ mm)

(E) Linyi sandstone, penetration depth = 13 mm

Figure 6.29 shows the results of the numerical simulation at the penetration depth of 13 mm. The optimum cut spacing was 26 mm, and the corresponded s/p ratio was 2. From the results of the numerical analysis and

the results of the LCM test, it can be possible that the optimum s/p ratio gradually decreases as the penetration depth increases.

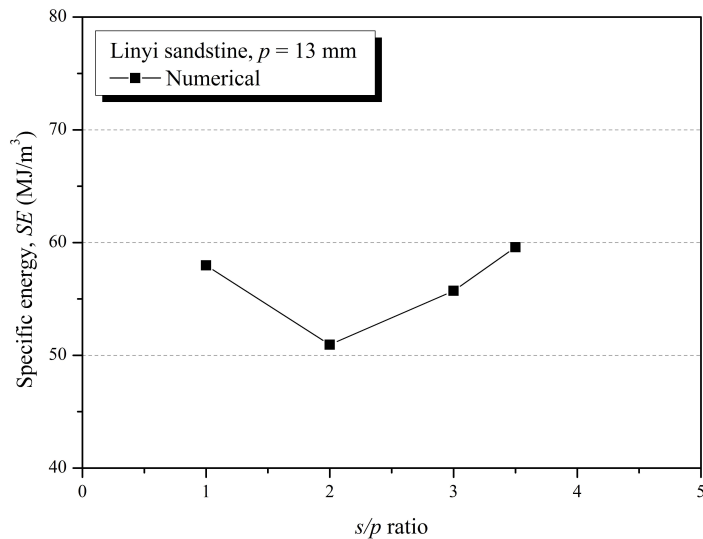


Figure 6.29 The result of the optimum cut spacing at 13 mm of penetration depth in numerical simulation (Linyi sandstone)

(F) Concrete, penetration depth = 5 mm

In the case of the Linyi sandstone, the optimum cut spacings in the numerical simulation were matched will with that of the LCM. Figure 6.30 shows the comparison results of the specific energy between the LCM and numerical simulation for the concrete at the 5 mm of penetration depth. In the LCM, optimum cut spacing was 20 mm, while it was derived as 25 mm in the numerical simulation. As the cutting force was underestimated, the specific energy of the stones was lower than the LCM test overall.

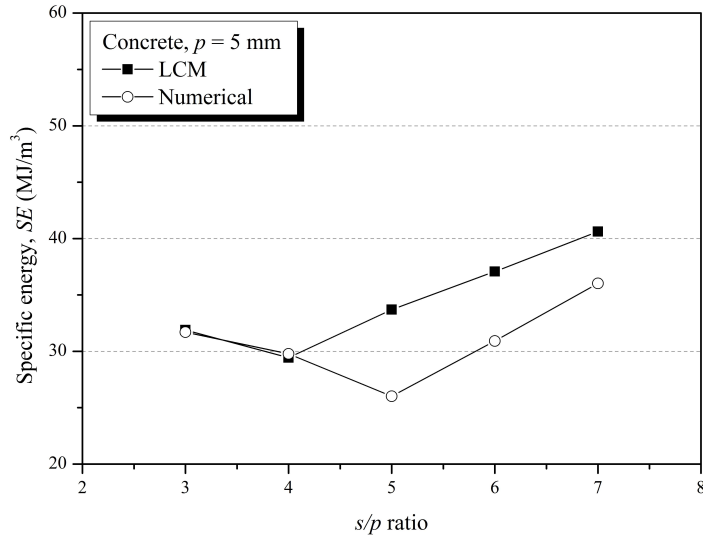


Figure 6.30 The comparison of the specific energy between the LCM and the numerical simulation (Concrete, $p = 5$ mm)

6.4.4 Different attack angles

The effect of the attack angle on the cutting forces and the specific energy was investigated in the wide range of attack angle using numerical simulation. The testing condition and numerical results were summarized in Table 6.10. The attack angles vary in the range of 25 to 65, and the penetration depth and cut spacing were fixed as 5 mm and 20 mm, respectively.

Table 6.10 The numerical and LCM results in different attack angles

Attack angle	Mean cutting force, F_{c_mean} (kN)		Mean normal force, F_{n_mean} (kN)		Specific energy (MJ/m ³)	
	LCM	Numerical	LCM	Numerical	LCM	Numerical
25	-	17.57	-	8.48	-	117.13
30	-	13.10	-	8.17	-	93.13
35	15.03	9.76	7.48	6.74	142.71	73.45
40	-	6.87	-	5.71	-	59.57
45	5.81	4.83	5.87	4.96	67.57	41.24
50	-	4.18	-	5.48	-	38.73
55	2.81	3.62	2.86	4.32	39.62	40.17
60	-	2.49	-	3.88	-	34.51
65	-	2.01	-	3.39	-	37.22

*Cutting conditions are $p = 5 \text{ mm}$, $s = 20 \text{ mm}$ and $\theta = 0$

Figures 6.31 - 6.33 show the comparison results of the mean cutting force, the mean normal force and the specific energy between the LCM and numerical simulation at the different attack angles. It is already shown in figures 4.32 and 4.33 that the mean cutting force and the mean normal force decreases with the increase of the attack angles in the range of 35 - 55°. The numerical results also indicate that the cutter forces decrease with the attack angle in the wide range. The specific energy also decreases with the attack angle with the similar trend of the LCM results.

The effect of the attack angle on the cutting force and the specific energy in the numerical simulation is similar to the LCM results, however, the quantitative results of the numerical simulation differ from the LCM results.

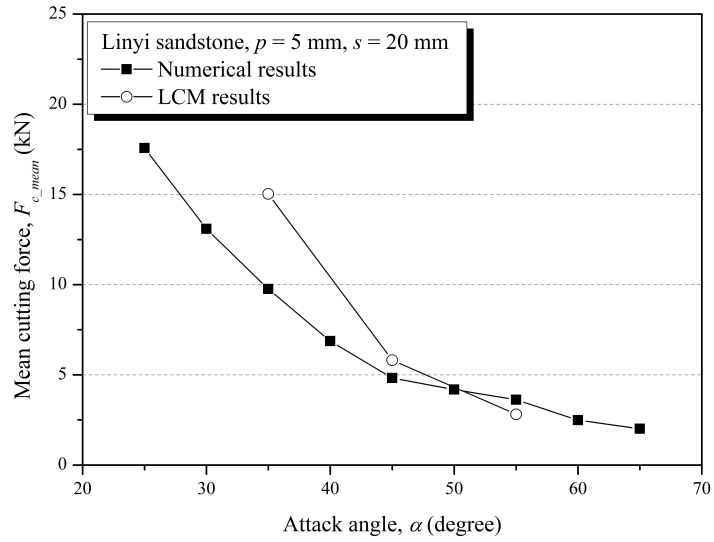


Figure 6.31 The comparison of the effect of attack angle on the mean cutting force in the LCM and the numerical simulation

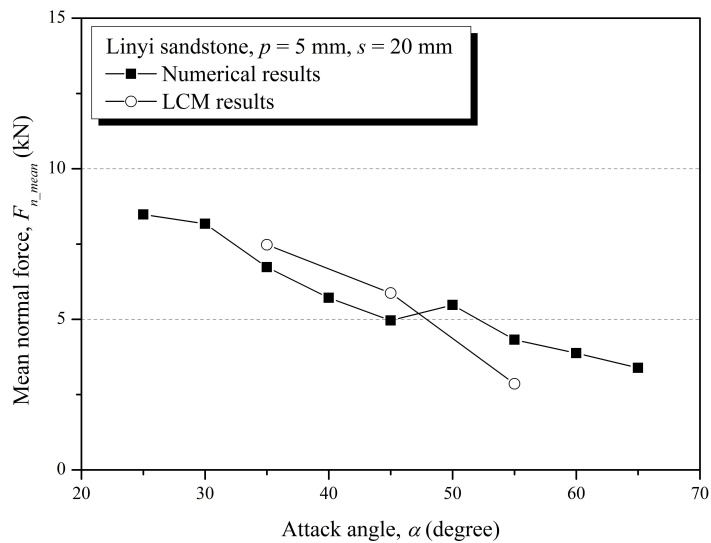


Figure 6.32 The comparison of the effect of attack angle on the mean normal force in the LCM and the numerical simulation

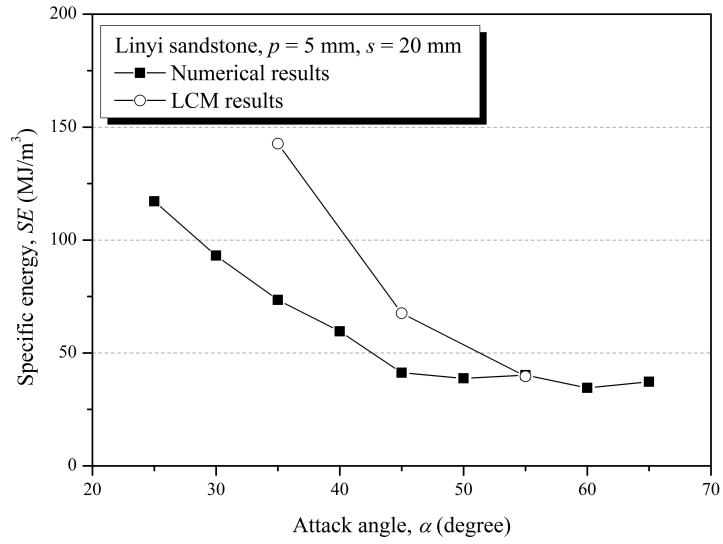


Figure 6.33 The comparison of the effect of attack angle on the specific energy in the LCM and the numerical simulation

7. Discussion

7.1 Analysis of the LCM result

7.1.1 Small scaled LCM system

This study used a small-scale LCM test system for evaluating the cutting performance of a pick cutter under various cutting conditions. As the results above, the test results show that a reasonable result analysis is possible even if a linear cutting test is performed using a small-scaled rock specimen. However, there is a limitation in that a large number of cutting lines cannot be applied in each case due to the restriction of specimen size compared to the full-scaled LCM. However, five cutting lines per each case in this study are considered sufficient to provide a consistent test result.

7.1.2 Effect of the penetration depth and cut spacing

The LCM test results show that as the penetration depth increases, the cutting force and the normal force increase and the specific energy decreases. The effect of this penetration depth is independent of other cutting conditions, in other words, it is unaffected by skew angle, attack angle, and cut spacing. It means that applying the maximum penetration depth according to the machine's specifications under any cutting conditions is optimum condition leading to efficient excavation.

The cut spacing also has a significant effect on the cutter force and the specific energy. The cut spacing determines the interconnection of the cracks

caused by the adjacent cutter and thus is the most important factor in determining the specific energy which is the parameter indicating the excavation efficiency.

On the other hand, the penetration depth and the cut spacing do not affect the ratio of various cutter forces. The ratio of the peak force to the mean force, the cutting coefficient, and the resultant force angle are not influenced by the penetration depth and cut spacing. Therefore, it is not necessary to consider the cut spacing and the penetration depth for determining these parameters.

7.1.3 Effect of the rock type

The mean cutter force of concrete was lower than that of Linyi sandstone with the same cutting conditions (Fig 7.1), which is considered to be due to the difference of strength of specimen. The result is reasonable because it is generally known that the mean cutter force required for rock cutting increased as the strength of the rock is increased.

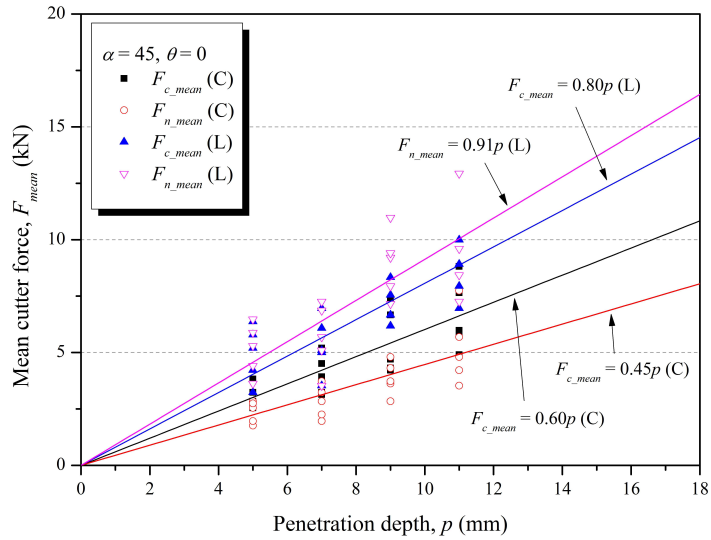


Figure 7.1 The comparison of the mean cutter force between Linyi sandstone (L) and concrete (C)

On the other hand, there is no difference between Linyi sandstone and concrete for the peak force of concrete. This means that the ratio of the peak force to the mean force is influenced by the characteristic of cutting (brittle/ductile) according to the composition of rock, brittleness of the rock, etc. rather than by the strength of the rock. In this study, this ratio was found to be in the range of 2 to 4. However, this ratio cannot be concluded as a result of this study, and it is necessary to test various rocks in the future.

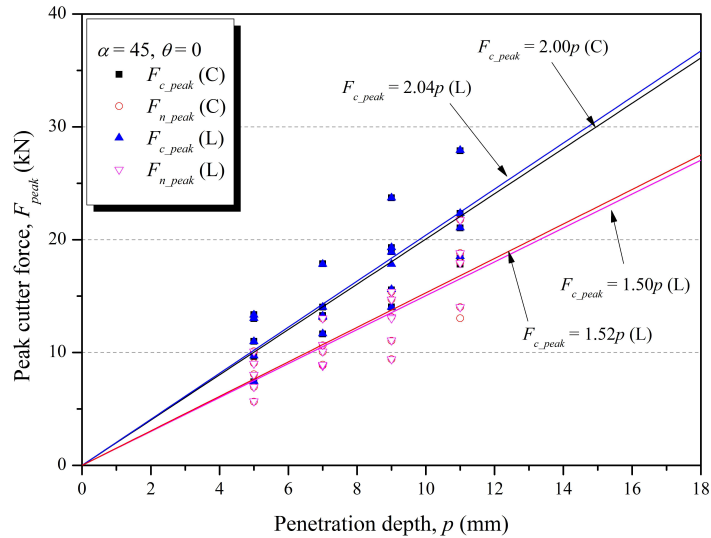


Figure 7.2 The comparison of the peak cutter force between Linyi sandstone (L) and concrete (C)

The ratio of the cutting force to the normal force is affected by the characteristic of rock (Figure 4.6 and figure 4.13). According to the physical meaning, the ratio means the friction coefficient between the two material. Therefore, the contact area between the pick cutter and rock surface (determined by the dimension of the pick cutter), the roughness of rock surface, the composition of the rock, the friction coefficient where the normal stress is not applied can be influencing parameters on the ratio. It also indicates that the ratio can be determined as the rock properties where the cutting condition and dimensions of the pick are pre-determined.

The specific energy of concrete was lower than that of Linyi sandstone with the same cutting conditions (Figure 7.3), which is considered to be due

to the difference of strength of specimen. The result is reasonable because it is generally known that the specific energy required for rock cutting increased as the strength of the rock is increased.

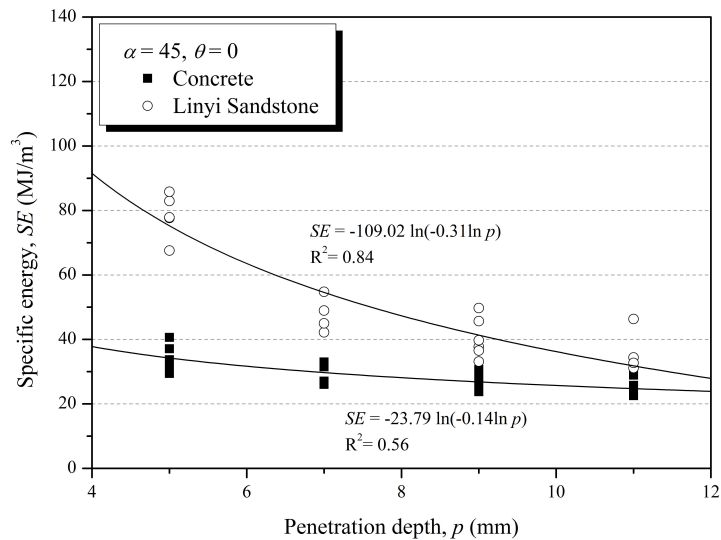


Figure 7.3 The difference of specific energy between Linyi sandstone and concrete

7.1.4 Effect of the skew angle

(A) Cutting performance and machine operation

Bilgin et al. (2006) reported that the skew angle does not significantly affect the cutting performance of the rock up to 30°. However, the results of this study show that the skew angle has a great influence on the cutter force. Especially, the normal force decreased with the skew angle, and the

cutting force of the cutter increased up to $\pm 15^\circ$ of skew angle while it decreased at ± 20 degrees of skew angle. The side force changed inversely with the change of the cutting force. Also, due to the ratio of the side force and the cutting force, bending moments are applied on the pick cutter and cutter head, so it is necessary to examine the stability of the machine's structure. Regarding the machine's stability, the test results showed that the direction of the resultant force and the skew angle agree with each other up to the skew angle is $\pm 15^\circ$. However, it deviates significantly at the $\pm 20^\circ$ of skew angle.

The specific energy was also significantly influenced by the skew angle. According to the skew angle, the specific energy was different by 1.8 times under the same cutting condition, and the minimum specific energy was observed at $\pm 20^\circ$ of the skew angle.

The results indicate that the skew angle is an important parameter to be considered for evaluating the rock cutting performance of the pick cutter. Also, the effect of the skew angle on the cutting performance is considered independent of the penetration depth and rock types. In terms of machine operation, the large skew angle (for $\pm 20^\circ$ of skew angle) is preferable for the specific energy and cutting efficiency, while the stability of the machine is decreased, the proportion of rock powder is increased, and the cutter life is reduced due to the increase of the contact area. Regarding the cutter life which is the main reason to employ the skew angle, $\pm 20^\circ$ of skew angles are not preferable cutting condition nevertheless the cutting efficiency is increased. While the $\pm 5 - 15^\circ$ of skew angles can be adopted for the mechanical stability and the cutter life although the cutting efficiency is

decreased.

(B) Cutter rotation

Bilgin et al. (2006) reported that the skew angle is applied to induce the free rotation of the cutter to generate uniform wear of the cutter. On the other hand, in the test of this study, when the skew angle was $\pm 15^\circ$, the pick cutter can freely rotate during rock cutting, while when the skew angle was $\pm 20^\circ$, it cannot freely rotate since the friction with the rock was increased due to the side force was drastically increased. It means that although the specific energy is minimized at the 20° of the skew angle, considering the cutter life in the high abrasive rock mass, it is more efficient not to apply the skew angle.

(C) Effect of the free surface on the cutting performance

In this study, the skew angle is divided into positive and negative angles according to whether the cutting tool faces the free surface of the rock as described above. However, in the above test results, there was no difference in cutting force and cutting efficiency according to the direction of the skew angle.

However, in most designs of the machine, the direction of the skew angle is not to the free surface (positive skew angle), especially, it is preferable to apply the positive skew angle to the edge of the cutting head. The negative skew angle can be found at the chain type of trenching cutter. Considering

that the cutter arrangement in the trenching cutter should take into consideration not only the cutting characteristics of the rock but also the geometry of the trench (it is necessary to apply the negative skew angle in consideration of the cut spacing and the width of the trench), the negative skew angle is considered to be a reasonable in terms of cutting performance.

7.1.5 Effect of the attack angle

The attack angles also have a significant effect on cutter force and specific energy. Especially, the ratio of normal force to cutting force is dominantly influenced by the attack angle. The smaller the attack angle, the larger the ratio of the cutting force. On the contrary, the larger the attack angle, the larger the ratio of the normal force.

At the same cutting conditions, the specific energy and the cutter forces tended to decrease with the attack angle. It is due to the contact area between the cutter and the rock. Although the specific energy and the cutter force decrease as the attack angle increases, it should be noted that the optimum cut spacing may be less than when the attack angle is small. At the same penetration depth, the width of the pick cutter in contact with the rock varies with the attack angle, and thus the crack propagation length may change.

Also, like the skew angle, the attack angle generates the bending moment in the pick cutter, and it is preferable that the direction of the resultant force and the attack angle coincide with each other regarding the structural

stability. The attack angle is considered to be optimized at around 45°, but it must be accurately determined through the cutting test because it can vary with the strength characteristics of the rock.

7.1.6 Chip size and cutting performance

(a) Chip size and specific energy

In above section, figure 5.6 shows the relationship among the specific energy, the particle size, and its distribution parameters. The previous studies reported that the mean particle size produced by rock cutting is highly correlated with the specific energy. The result from in this study also indicates that the particle size which was represented by mean particle size , the absolute size constant, and the size distribution (i.e., coarseness index and uniformity index) are highly correlated with the specific energy. Thus, the particle size produced by rock cutting directly indicate the cutting efficiency. This means that the size of the rock chip can also be used as an index of cutting efficiency, and it will be necessary to collect a database of experimental and site for more rocks and cutting conditions.

(b) Rock powder generation

As with the size of the rock chip, the ratio of rock powder produced in the rock cutting test or site excavation is an indicator of the inefficiency of the cutting. In the cutting conditions considered in this study, it was shown

that the ratio of rock powder in the cutting volume can be changed from 50% to 20% depending on the penetration depth and cut spacing.

It is not very economical to increase the ratio of rock powder, especially when mining minerals using mechanical excavation method. Therefore, it is reasonable to apply deep penetration depth regarding excavation efficiency and productivity.

7.2 Numerical simulation

SPH is a gridless (mesh free or meshless) technique for solving computational continuum dynamics problems and has several potential advantages over the grid based Lagrange processors. Especially, it is not necessary to deal with numerical troubles caused by excessive deformation of the mesh without erosion.

Based on the results above, the numerical model developed in this study can simulate the cutting process of the rock by the pick cutter comparatively realistically. Especially, the optimum cutting conditions are reasonable compared with LCM test, and it is concluded that the fragmentation of rocks under the optimum cutting conditions is also good agreement with the LCM result. However, the measurement of the cutter force is still necessary to be improved compared with the experimental results.

The most likely cause is the geometric shape of the cutter model. The pick cutter was modeled close to the real one, but it was partly simplified

in the modeling process. The particle size of SPH can also cause the difference with the experimental results. The cutting volume and the area of contact between the rock and the cutter are highly dependent on the size of the particle. It is necessary to examine the influence of the particle size on the result of the numerical simulation.

Even though the parameters of all the numerical analysis are determined as same as the experiment, the results of numerical simulation will be slightly different from the experimental results. In the numerical simulation, the rocks behave according to the predetermined equation of state, constitutive equation, conservation law and failure and yield functions. It is fundamentally impossible to explain the complicated and complex behavior of rock in cutting and chipping process with a single equation until now. Moreover, the rock model is consisted of elements of a certain size. The each element individually requires the cutting energy depending on the size of elements to be failed or to fall apart each other. While in the real cutting process, to cut the rock, only the cutting energy is required to propagate cracks in the local region to generate rock chips by the connection of cracks occur by the adjacent cutters. Thus, the required cutting energy of numerical simulation is fundamentally different from that of chipping process in actual rock cutting.

However, the change of specific energy and cutting force according to cutting conditions showed a tendency to agree with the experimental results. Therefore, the numerical simulation can provide useful information to evaluate the effect of influencing parameters on the cutting efficiency and the cutting performance of the cutting tools. Also, it can be used to

understand the relationship between the influencing parameters and design parameters (i.e., cutter forces and specific energy), not to find specific values.

On the other hand, the disadvantage of SPH technique is the limitation of the boundary condition. The infinite boundary condition is impossible in the SPH region because the transmit condition is not considered in SPH code. However, SPH is a Lagrangian based method; therefore the boundary conditions can be easily dealt with Lagrange-SPH, or Eulerian-SPH coupling models can be used in AUTODYN. Figure 7.5 shows the concept of Lagrange-SPH coupling, and figure 7.6 shows an example of the rock cutting simulation using Lagrange-SPH coupled model; the boundary of the rock is modeled with a Lagrange meshes. The advantage of the coupled model is that the computation time can be reduced compared to using only SPH; when the same number of elements are used, the calculation time of SPH is longer than that of the FEM model.

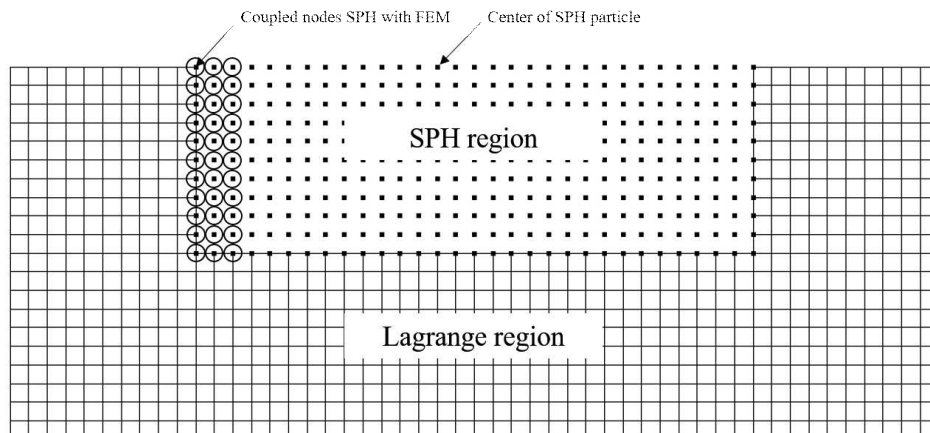


Figure 7.5 The concept of the Lagrange-SPH coupling

AUTODYN-3D v13.0 (+Beta Options) from ANSYS

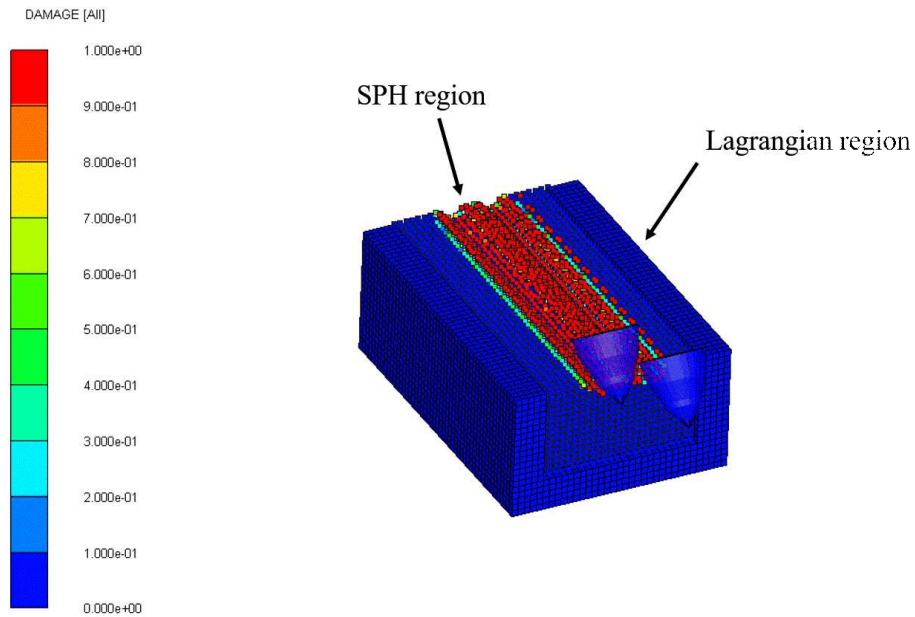


Figure 7.6 An example of rock cutting simulation using Lagrange-SPH coupled code in AUTODYN

7.3 Design case of trench cutter

In this study, the trenching cutter was designed using the results of the LCM test. The design process of trencher was programmed in the spreadsheet program. The general process of trenching cutter was shown in figure 7.7, and it is similar to that of typical mechanical excavator. Figure 7.8 shows the variables which are determined according to the rock surface and trench dimensions. The parameters were summarized in Table 7.1.

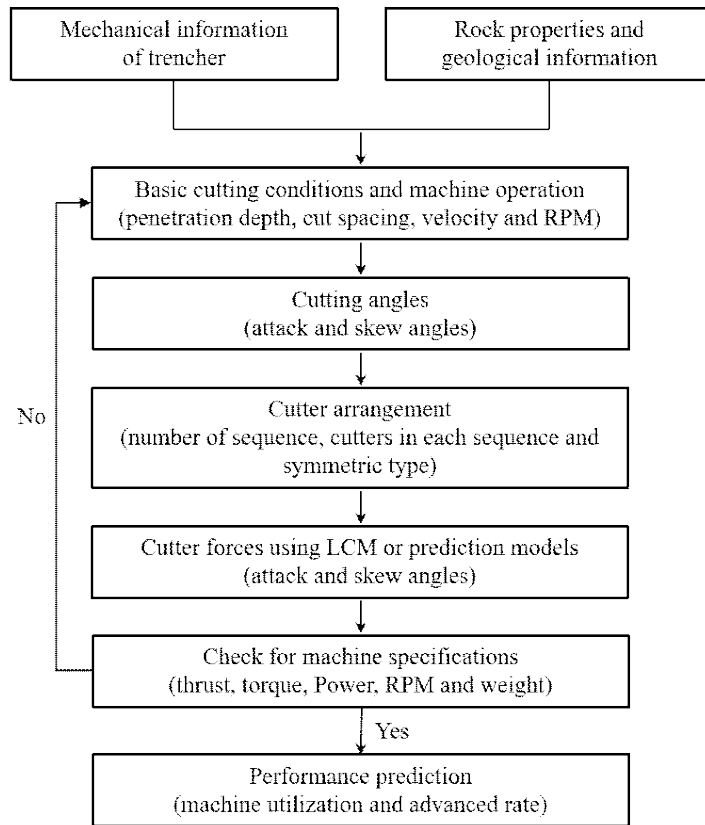


Figure 7.7 General flow chart of design for trenching cutter

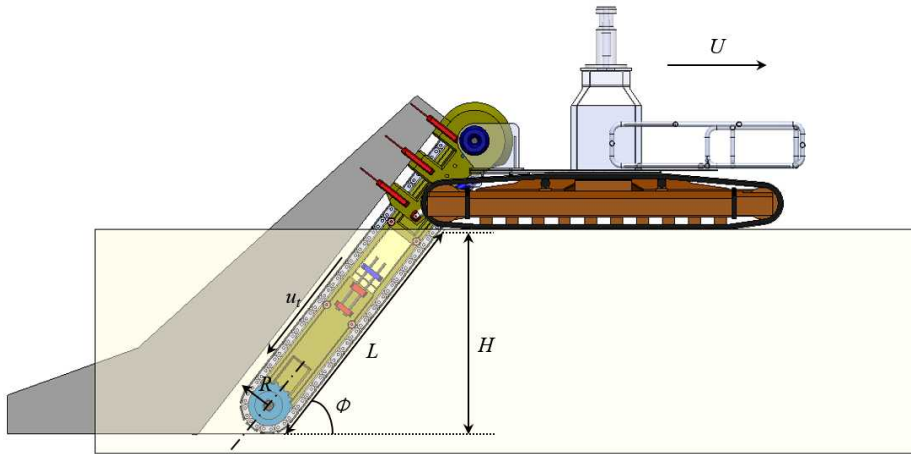


Figure 7.8 The schematic drawing and variables of trenching cutter

Table 7.1 The variables of trenching cutter used in this design

Parameters (unit)	Value
Height of trench, H (mm)	2500
Width of trench, W (mm)	600
Cutting angle, ϕ (degree)	48.0
Contact length between rock and cutter, L (mm)	3364
Target strength of rock mass, σ_c (MPa)	20

The contact length between the rock and trencher (L) is calculated by the height of trench (H) and cutting angle (ϕ). The linear velocity of the vehicle (U), the linear speed of chain (or cutting speed of pick cutter, u_i) are defined for the design. The radius of rotation (R) is calculated by summation the radius of chain sprocket and length of pick cutter. The penetration depth for the one pass of cutting is determined by the linear velocity of the vehicle, RPM , a number of the sequence of cutter arrangement. These basic parameters were inputted into the spreadsheet program for the cutter arrangement and estimation of the specification of the

machine. The geological parameters, which are related to the rock and rock-mass properties such as RQD (rock quality designation), bedding or foliation, joint sets, rock strengths and other mechanical properties of rock should be considered to design the trenching cutter. However, the rock properties were assumed and not considered in the current study.

Design sheet for Cutting-head optimization and Balancing of Trenching cutter										
Geological information			Trench Information			Mechanical information			Cutter Information	
UCS	20	MPa	Width	600	mm	Cutting speed	8.33	mm/s	Type	conical
BTS	1.8	MPa	Height	2500	mm	Length of arm	3100	mm	Tip angle	70
Specific energy	33.18		Cutting angle	48	degree	pick spacing	200	mm	Tip diameter	-
Energy transfer ratio	0.8		Length of contact	3364	mm	Lateral spacing	25	mm	Friction angle	30
			Vehicle Cutting Rate	48	m ³ /hr	No. picks	96	EA	Effective bit height	75.6 mm
						No. Plates	56			
						Max. cutters in Sequence	14			
						Periodic bit to bit	2860			
						Plates in a Set	14			
						Cutters in a Set	27			
						No. cutting sequence	4			
						penetration per rev	5.0	mm/rev		
						RPM	25			
						Sequences in contact	0.6			
						Cutters in contact	17			
						Sprocket radius	250	mm	(Assume)	
						Length of sprocket	1570.796227	mm	(Assume)	
						Length of chain	11000	mm	(Assume)	
Estimated cutting force										
	normal	cutting								
Conical	2.280	3.160								
Chisel	N/A	N/A								
Estimated Specification										
	Cutting power	Torque								
	N/A	N/A								

Figure 7.9 The spread sheet program for the design of trench cutter

The design parameters were determined from the LCM results, and the design procedure of the trenching cutter in this study is as follows:

1) *Cutter spacing*: figure 7.10 shows the concept of the cutter arrangement in trenching cutter. In pick arrangement, two type of spacing should be determined. The cutter spacing, S_c is the cutter spacing along the trench width, and it is the cut spacing in LCM test. On the other hand, the line spacing, S_L is the cutter spacing along the trench length. In this study, the line spacing was predetermined as 200 mm by the dimension of the trench. Therefore it is assumed that the line spacing did not affect the cutting performance of the pick. The cut spacing was determined as 25 mm (optimum cut spacing in LCM test), based on the Figure 4.14.

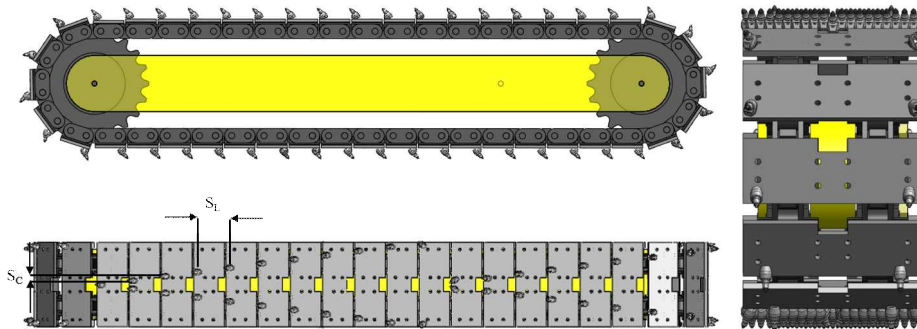


Figure 7.10 The concept of cutter spacings and cutter arrangement

2) *Attack angle and skew angles*: the basic attack angle and skew angle were determined as 45° , 0° with considering the cutting efficiency and the mechanical stability of the machine.

3) *Cutter arrangement*: the pick cutters are basically arranged symmetrically with respect to the central axis of the chain cutter. In this study, the cutters are repeatedly arranged in four cycles. Since the total number of plates is 52, one sequence is composed of 13 plates (cutter pair).

Apparent cutter spacing defined by the location of the cutter holder is gradually reduced as it is away from the center of the trench cutter chain, which is a necessary concept to match the number of cycles and cutters. The gap between the reduced cut spacing and the optimum cut spacing is compensated by using the skew angle of the pick cutter. As a result, the cutting spacing at which the actual cut is made is constant at 25 mm. The effective application range of the square obtained from the linear cutting test is $5 \sim 15^\circ$ on center area. Figure 7.8 shows the cutter arrangement of the

trench cutter.

There are cutters that overlap with other periodic cutter arrangements, the red plotted cutter in figure 7.9, for excavation of the left and right edges of the trench, which reduce the angle of attack to 40° , less than 45° of the normal cutters located in center area. Therefore, when this cutting is performed, the excavation is performed by applying less penetration depth per revolution than the normal cutters. The position of the red cutters should be located as far away from the chain as possible, taking into account the size of the cutter holder.

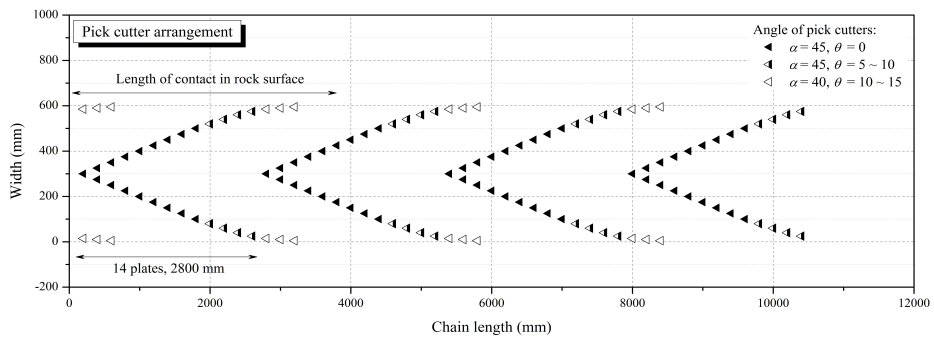


Figure 7.11 The pick arrangement on the trenching cutter (4 sequential arrangement)

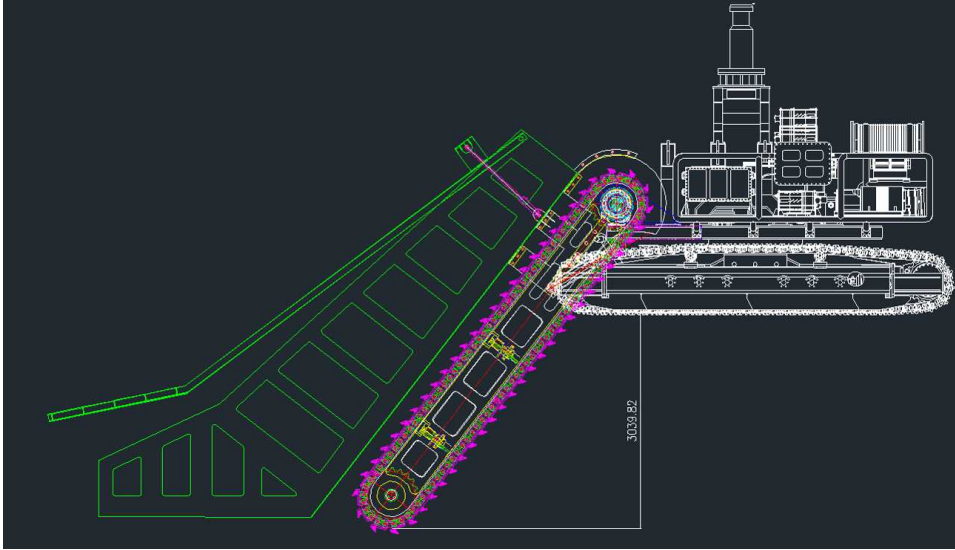


Figure 7.12 The schematic drawing of the designed trenching cutter

4) *Cutter forces*: The normal force and cutting force where the attack angle and skew angle are 45° and 0° , respectively, were estimated based on the LCM results and the figures 4.10 and figure 4.11. The cutter forces (in kN) at the 25 mm of cut spacing and different penetration depth can be calculated by following equations which are based on the LCM results for concrete. The side force was assumed as the 5% of the cutting force where the skew angle set as 0° .

$$F_{c_mean} = 0.85 \times p^{0.80} \quad (7.1)$$

$$F_{n_mean} = 0.91 \times p^{0.69} \quad (7.2)$$

For the more general cutting case (different cut spacings and penetration depths), these following equations can be used for the estimation of the

cutter forces. These equations were also obtained from the statistical analysis of the LCM results.

$$F_{c_mean}(N) = 63.55 \times p^{0.98} \times s^{0.72} \quad (7.3)$$

$$F_{n_mean}(N) = 33.49 \times p \times s^{0.81} \quad (7.4)$$

If there is no available linear cutting data, then the forces acting on the pick cutters can be estimated by the empirical and analytic prediction models. They were already summarized in table 2.2, it was not repeated here.

On the other hand, when the pick cutters with having the skew angle, the cutter forces were calculated by multiplying the correction factors in table 7.8 obtained from the LCM results. The side force was calculated by the side force coefficient which was determined from the LCM results of Linyi sandstone (figure 4.21). The correction factor for the cutter force with skew angle is summarized in Table 7.8.

Table 7.2 The correction factors for calculation of the three directional cutter forces

Skew angle	Normal force	Cutting force	Side force
0	1	1	$0.05 \times F_{c_mean}$
5	0.85	1.15	$0.15 \times F_{c_mean}$
10	0.9	1.4	$0.2 \times F_{c_mean}$
15	0.8	1.2	$0.25 \times F_{c_mean}$

5) *Total forces*: After the cutter force of the individual cutters is calculated based on the arrangement. The total cutting and normal forces acts on the trenching cutter can be calculated in consideration of the number of cutters contacting simultaneously with rock. Since the maximum length of contact between the chain cutter and the rock, the number of plates that can simultaneously contact the rock is 19.

$$F_{n_total} = \sum_1^n F_{n_mean} \quad (7.1)$$

$$F_{c_total} = \sum_1^n F_{c_mean} \quad (7.2)$$

6) Because of the trencher excavates the rock mass with having the specific cutting angle, the components of the total cutting force and the normal force should be transformed to the horizontal and vertical directions as following equations:

$$F_H = \sin(\phi) \times F_{n_total} + \cos(\phi) \times F_{c_total} \quad (7.3)$$

$$F_V = \cos(\phi) \times F_{n_total} - \sin(\phi) \times F_{c_total} \quad (7.4)$$

7) *Specifications*: based on the total force, torque and power of the trench cutter can be estimated as figures 7.11 and 7.12. Since the power capacity of the machine is 132 kW, the preferable operational conditions are given as Table 7.9. Because the penetration depth which is general operation

parameter in other mechanical excavators is determined by the *RPM* and the linear velocity of vehicle, only *RPM* and linear velocity of vehicle is the operation parameter in trencher.

$$\text{Torque, } T = R \times F_{c_total} \quad (7.5)$$

$$\text{Power, } P = \frac{2\pi \times RPM \times T}{60} \quad (7.6)$$

Table 7.3 The preferable operation condition of the trenching cutter

Vehicle speed (m/hr)	RPM range
300	10-20
250	10-25
200	10-25
150	10-30
100	10-40
50	10-50

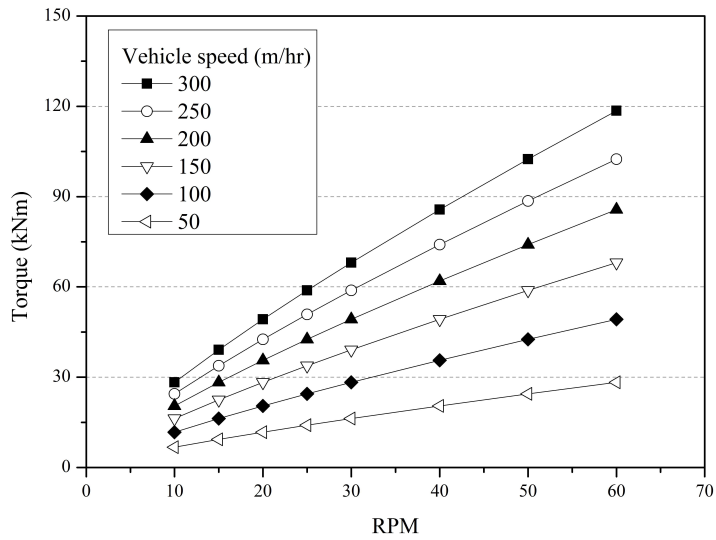


Figure 7.13 Torque requirement of the trench cutter according to different operational conditions

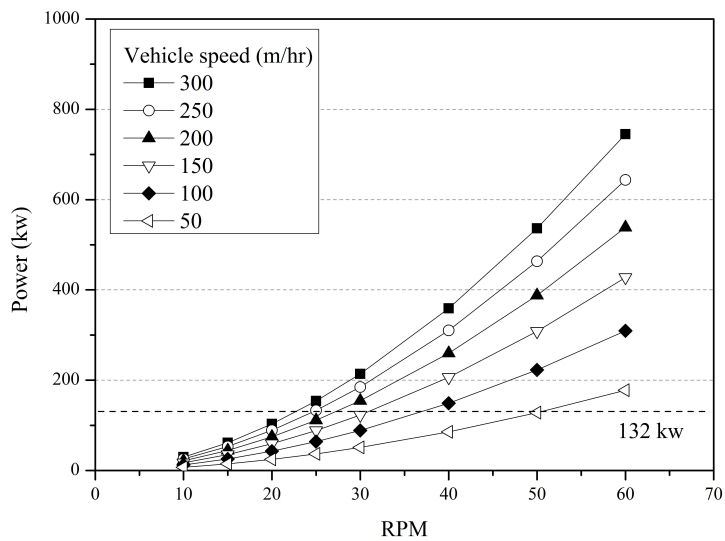


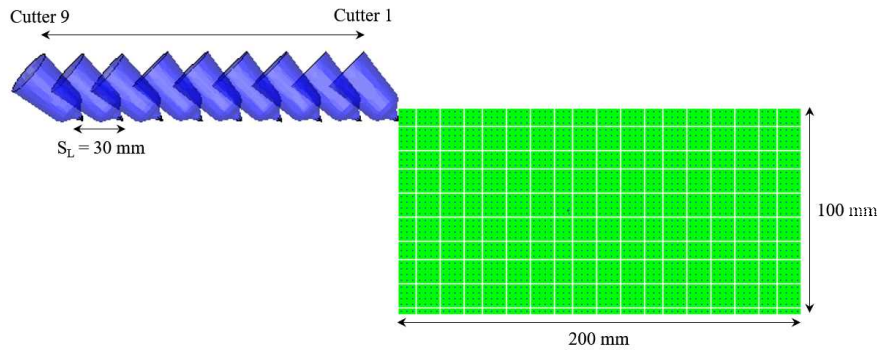
Figure 7.14 Power requirement of the trench cutter according to different operational conditions

The cutter arrangement of the trenching cutter was numerically tested. Figure 7.15 shows the numerical model to simulate the rock excavation process by the multiple cutters. Since the cutter arrangement of the trenching cutter is fully symmetrical, the numerical model simulates the half of the trenching cutter. Also, the pick cutters which are close to the center of the trenching cutter and have the same cutting angle ($\alpha = 45^\circ$, $\theta = 0^\circ$), are excluded from the analysis. The attack angle and skew angle of the No. 7 - 9 pick cutters are 40° and $10 - 15^\circ$, respectively.

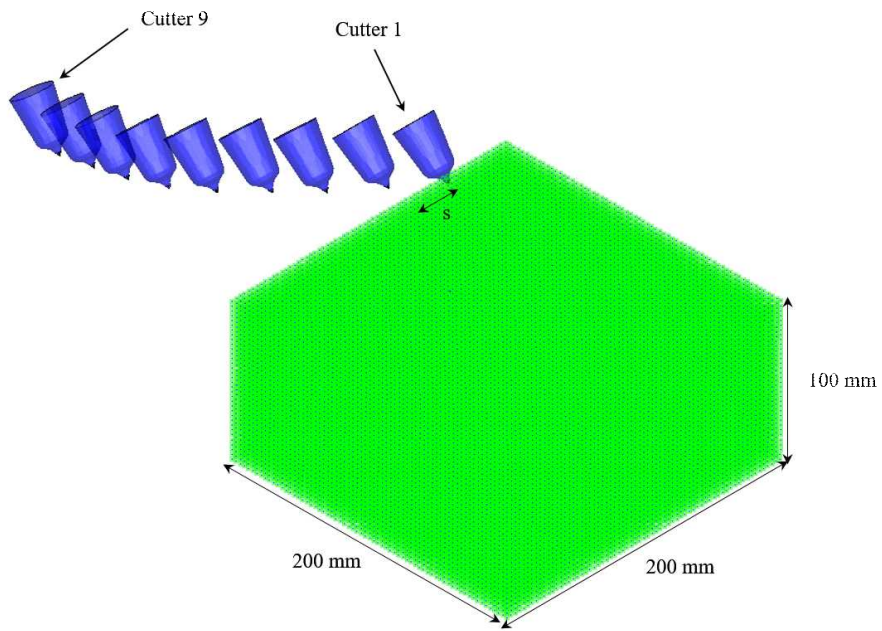
Table 7.4 The information of cutter arrangement in the simulation

Cutter No.	Position*	Cutter spacing	Attack angle	Skew angle
1	30	25	45	0
2	55	25	45	0
3	75	20	45	5
4	95	20	45	5
5	115	20	45	5
6	130	15	45	5
7	140	10	40	10
8	150	10	40	10
9	155	5	40	15

*Position of cutter is from the center of the trench cutter



(a)

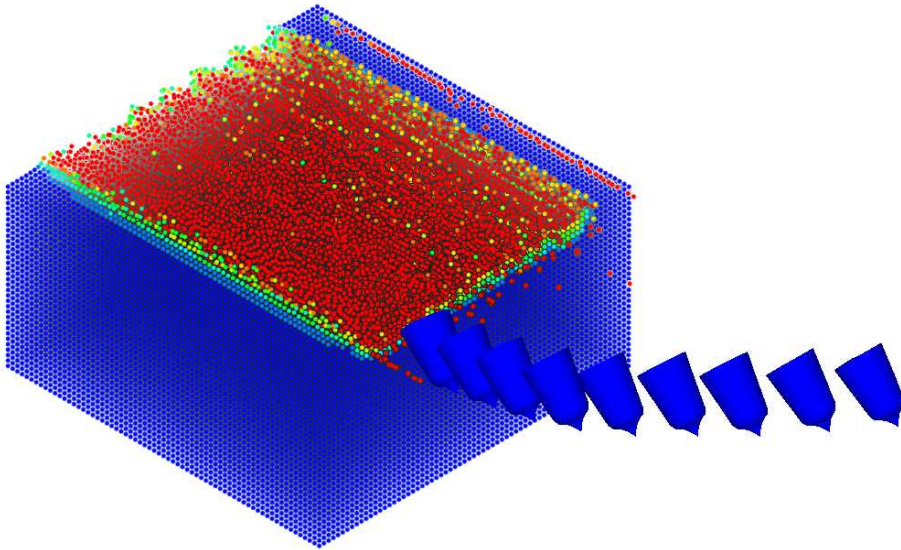


(b)

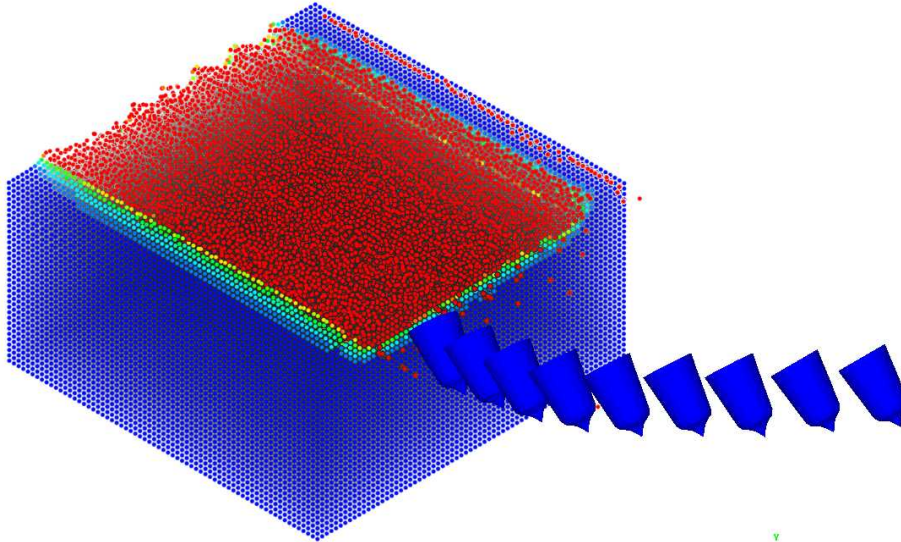
Figure 7.15 The numerical model of the rock excavation by multiple cutters (a): side view and (b) isometric view

Figure 7.16 shows the rock surface after the 1 pass of cutting by the trenching cutter. The rock surfaces of Linyi sandstone and concrete were completely excavated corresponding to the predetermined penetration depth and width of the trench. Therefore, it can be confirmed that the trenching cutter can be successfully performed the trench construction for two types of rocks using the cutter arrangement proposed in this study. The results of the cutter force were already analyzed in the previous chapter 6 and are excluded here.

Since the rock excavation equipment is very large in scale, it is very difficult to evaluate the suitability of the mechanical excavator and the suitability of the cutter arrangement by carrying out the pilot test. However, if the numerical model can accurately simulate the excavation process of the rock, it is possible to evaluate the cutting performance of the mechanical excavator and the suitability of the cutter arrangement. The numerical model proposed in this study is expected to be able to evaluate the design of machine excavation equipment.



(a) Linyi sandstone



(b) Concrete

Figure 7.16 The simulation results of the rock surfaces after the cutting by the trenching cutter

8. Conclusions

This study investigated the rock cutting mechanism of pick cutter used in trencher and roadheader, and performed linear cutting test on Linyi sandstone and concrete under various cutting conditions to compare and analyze the cutting performance of rock. In addition, image processing technique and sieve test were used to quantitatively analyze the size distribution of rock chip and the proportion of rock powder ratio of the cut rock produced in the cutting test. Finally, to overcome the limitation of the finite element method in the rock cutting simulation, the SPH technique was applied and the applicability in the rock cutting simulation was evaluated. The main conclusion of this study as follows.

1) The effect of skew angle of the pick cutter on cutting performance was investigated. The skew angle was classified into nine levels according to the magnitude of angle and direction of pick cutter. There was no significant effect of the direction of the skew angle on the cutting performance. And the skew angle has a great influence on the cutter force. The normal force decreased with the skew angle, and the cutting force of the cutter increased up to 15° of skew angle while it decreased at 20 degrees of skew angle. The side force changed inversely with the change of the cutting force. Especially, the side force drastically increased at the 20° of skew angle. The specific energy increased with the skew angle, however it was minimized at the 20° of skew angle for all penetration depths. As the results, the effect of the skew angle on the cutting performance is

considered independent to the penetration depth and rock types. The results of the specific energy showed the 20° of the skew angle is optimum skew angle. However, the ratio of the side force and the other forces, the direction of resultant force, and the ratio peak to mean force, excluding the specific energy, indicate that the limit skew angle is up to 15 degrees. Therefore, this study suggested that skew angle should be applied up to 15 degrees with considering structural stability of the machine.

2) The effect of the attack angle of the pick cutter on cutting performance was investigated. The attack angle was considered as three levels. The attack angle also has significant effect to the cutting performance. Especially, the ratio of normal force to cutting force is dominantly influenced by the attack angle. The smaller the attack angle, the larger the ratio of the cutting force. On the contrary, the larger the attack angle, the larger the ratio of the normal force.

At the same cutting conditions, the specific energy and the cutter forces tended to decrease with the attack angle. This is due to the contact area between the cutter and the rock. Although the specific energy and the cutter force decreases as the attack angle increases, it should be noted that the optimum cut spacing may be less than when the attack angle is small. It is not preferable because the decrease of the cut spacing leads to increase on the number of cutters.

The results of the specific energy showed the 55° of the skew angle is optimum attack angle. However, the direction of resultant force and the ratio peak to mean force indicate that the optimum attack angle is 45° . Therefore,

this study suggested that optimum attack angle is 45° with considering structural stability of the machine. However, in order to fully understand the effect of the attack angle, it is considered that test results for various attack angles are necessary.

3) The effect of the penetration depth and cut spacing of the pick cutter on cutting performance was investigated. The LCM test results show that as the penetration depth increases, the cutting force and the normal force increase and the specific energy decreases. Also, the optimum s/p ratio tended to decrease with increasing penetration depth, and the ratio was 4 at the penetration depth of 5 mm, while the ratio was 2 at the penetration depth of 11 mm.

The effect of the penetration depth is independent of other cutting conditions, in other words, it is unaffected by skew angle, attack angle, and cut spacing. It means that applying the maximum penetration depth according to the machine's specifications under any cutting conditions is optimum condition leading to efficient excavation.

On the other hand, the penetration depth and the cut spacing do not affect the ratio of various cutter forces. The ratio of peak force to the mean force, the cutting coefficient, and the resultant force angle are not influenced by the penetration depth and cut spacing. Therefore, it is not necessary to consider the cut spacing and the penetration depth for determining these parameters.

4) Using the image processing and the sieve analysis, the relationship

between the size of the rock chip and its distribution, the cutter force and the specific energy was investigated. The cutter force increased with the size of rock chip and the result from in this study also indicate that the coarseness index, mean particle size and the absolute size constant are highly correlated with the specific energy. Thus, the particle size and its distribution produced by rock cutting directly indicate the cutting efficiency. This means that the size of the rock chip can also be used as an index of cutting efficiency, and it will be necessary to collect a database of experimental and site for more rocks and cutting conditions

5) The proportion of the rock powder of the excavated volume is analyzed. The rock powder (diameter less than 2 mm) produced by high level of compressive stress in the crushed zone were correlated with specific energy, Also The ratio of rock powder that can occur in rock cutting was found to be more than 20% at the considered cutting conditions. The results showed that the ratio of rock powder in the cutting volume can be changed from 20% to 50% depending on the penetration depth and cut spacing. The ratio can be reduced by the increasing of the penetration depth, and the skew angle has negative effect to the generation of the rock powder. The results of this study can be used to optimize mechanical excavation efficiency and to increase the production rate of minerals in mining engineering.

6) The numerical model developed in this study can simulate the cutting process of the rock by the pick cutter comparatively realistically. Especially,

the optimum cutting conditions are reasonable compared with LCM test and it is conclude that the fragmentation of rocks under the optimum cutting conditions is also good agreement with the LCM result. Especially, it is significant that the cutting process of the rock is modeled without using the erosion technique forced for the cutting analysis in the finite element method. However, the results of numerical simulation are still necessary to be improved compared with the experimental results. Because the all of the mechanical properties (i.e., anisotropy, heterogeneity) cannot be applied in the numerical simulation.

References

- Altindag, R., 2003, Estimation of penetration rate in percussive drilling by means of coarseness index and mean particle size, *Rock Mechanics and Rock Engineering*, Vol. 36(4), pp. 323 - 332.
- Bakar, MZA., Gertsch, LS., 2013, Evaluation of saturation effects on drag pick cutting of a brittle sandstone from full scale linear cutting tests, *Tunnelling and Underground Space Technology*, Vol. 34, pp. 124-134.
- Balci, C., Bilgin, N., 2007, Correlative study of linear small and full-scale rock cutting tests to select mechanized excavation machines, *International Journal of Rock Mechanics & Mining Sciences*, Vol. 44, pp. 468-476.
- Bilgin, N., 1977, Investigation into mechanical cutting characteristics of some medium and high strength rocks”, Ph.D. thesis, University of Newcastle Upon Tyne, UK, pp. 332.
- Bilgin, N., Demircin, MA., Copur, H., Balci, C., Tuncdemir, H., Akcin, N., 2006, Dominant rock properties affecting the performance of conical picks and the comparison of some experimental and theoretical results, *International Journal of Rock Mechanics & Mining Sciences*, Vol. 4(1), pp. 139-156.
- Bilgin, N., Copur, H., Balci, C., 2014, *Mechanical Excavation in Mining and Civil Industries*, CRC press, pp. 125.
- Bruland A. Hard rock performance data and back-mapping. NTNU, Department of Building and Construction Engineering, Trondheim, Norway, 2000.
- Chang, SH., Choi, SW, Bae, GJ, Jeon, S., 2006, Performance prediction of TBM disc cutting on granitic rock by the linear cutting test. *Tunnelling and Underground Space Technology*, Vol. 21(3-4), pp. 271.

- Choi, SW., Chang, SH., Park, YT., Lee, GP., 2014a, Performance estimation of conical picks with slim design by the linear cutting test (I): depending on attack angle variation, *Journal of Korean Tunnel and Underground Space Association*, Vol 16(6), pp. 573-584.
- Choi, SW., Chang, SH., Park, YT., Lee, GP., 2014a, Performance estimation of conical picks with slim design by the linear cutting test (II): depending on skew angle variation, *Journal of Korean Tunnel and Underground Space Association*, Vol 16(6), pp. 585-597.
- Cho, JW., Jeon, S., Yu, SH., Chang, SH., 2010, Optimum spacing of TBM disc cutters: a numerical simulation using three-dimensional dynamic fracturing method. *Tunnelling and Underground Space Technology*, Vol. 25, pp. 230 - 244.
- Cho, JW., Jeon, S., Jeong, HY., Chang, SH., 2013, Evaluation of cutting efficiency during TBM cutter excavation within Korean granitic rock using linear cutting machine testing and photogrammetric measurement. *Tunnelling and Underground Space Technology*, Vol. 35, pp. 37 - 54.
- Copur, H., 2010, Linear stone cutting tests with chisel tools for identification of cutting principles and predicting performance of chain saw machines, *International Journal of Rock Mechanics & Mining Sciences*, Vol. 47, pp. 104-120.
- Copur, H., Balci, C., Bilgin, N., Tumac, D., Avunduk, E., 2012, Predicting cutting performance of chisel tools by using physical and mechanical properties of natural stones, *European Rock Mechanics Symposium (Eurock 2012, ISRM International Symposium)*, May 28-30, Stockholm, p. 14.
- Den Hartog, MH., Babuska, R., Deketh, HJ., Alvarez Grima, M., Verhoef, PNW. Verbruggen, HB., 1997, Knowledge-Based Fuzzy Model for performance prediction of a Rock-Cutting Trencher, *International Journal of Approximate Reasoning*, Vol. 16, pp. 43-66.

- Dogruoz, C., Bolukbasi, N., Rostami, J., Acar, C., 2016, An Experimental study of Cutting Performances of Worn picks, *Rock Mechanics and Rock Engineering*, Vol. 49, pp. 213-224.
- Ersoy, A., Waller, MD., 1997, Drilling detritus and the operating parameters of thermally stable PDC core bits, *International Journal of Rock Mechanics & Mining Sciences*, Vol. 34(7), pp. 1109-1123.
- Evans, I., 1962, A theory of the basic mechanics of coal ploughing, *Proceedings of the International Symposium on Mining Research*, University of Missouri, Pergamon Press, v2, pp. 761-768
- Evans, I., 1972a, Line spacing of picks for efficient cutting, *International Journal of Rock Mechanics & Mining Sciences & Geomechanics Abstracts*, Vol. 9, pp. 355-359.
- Evans, I., 1972b, Relative efficiency of picks and discs for cutting rock, MRDE Report No. 41, National Coal Board, UK, pp. 6.
- Evans, I., 1982, Optimum line spacing for cutting picks, *The Mining Engineer*, January, pp. 433-434.
- Evans, I., 1984a, A theory of the cutting force for point attack picks, *International Journal of Mining Engineering*, Vol. 2, pp. 63-71.
- Evans, I., 1984b, Basic mechanics of the point attack pick, *Colliery Guardian*, May pp. 189-193.
- Farrokh, E., Rostami, J., 2008, Correlation of tunnel convergence with TBM operational parameters and chip size in the Ghomroud tunnel, Iran, *Tunnelling and Underground Space Technology*, Vol. 23, pp. 700-710.
- Gertsch, L., Fjeld, A., Nilsen, B., Gertsch, R., 2000, Use of TBM muck as construction material. *Tunnelling and Underground Space Technology*, Vol. 15(4),

- pp. 379 - 402.
- Geng, Q., Wei, Z., Meng, H., Chen, Q., 2016, Numerical and experimental research on the rock-breaking process of tunnel boring machine normal disc cutters, *Journal of Mechanical Science and Technology*, Vol. 30(4), pp. 1733-1745.
- Geng, Q., Wei, Z., Ren, J., 2017, New rock material definition strategy for FEM simulation of the rock cutting process by TBM disc cutters, *Tunnelling and Underground Space Technology*, Vol. 65, pp. 179-186.
- Goktan, M., 1990, Effect of cutter pick rake angle on the failure pattern of high strength rocks, *Mineral Science Technology*, Vol. 11, pp. 281-285.
- Ha, D.H, 2002, A study on the technique of impact analysis against concrete target using lagrangian and smoothed particle hydrodynamics, *Journal of the Korea Institute of Military Science and Technology*, Vol(5), No. 2, pp. 207-216.
- Helmons, RLJ., Miedema, SA., Alvarez Grima, M., Van Rhee, C., 2016, Modeling fluid pressure effects when cutting saturated rock, *Engineering Geology*, Vol. 211, pp. 50-60.
- Herrenknecht, 2017, <http://www.herrenknecht.com>
- Jackson, E., Devaux, M., 2007, Performance prediction for a subsea mechanical trenching wheel, *Proceedings of the 6th International OSIGC*, pp. 527-532
- Jeong HY, Jeon SW, Cho JW, Chang SH, Bae GJ, 2010, Assessment of cutting performance of a TBM disc cutter for anisotropic rock by linear cutting test. *Journal of Korean Society for Rock Mechanics*, Vol. 21, pp. 508 - 517 (in Korean)
- Jeong, HY, Jeon, SW, Cho, JW, 2013, A numerical study on rock cutting by a TBM disc cutter using SPH code, *Journal of Korean Tunnel and Underground Space Association*, Vol. 15(3), pp. 345-356.

- Jeong, HY., Lee, SD., Jeon, SW., 2014, Current and future study on assessment of cutting performance of hard rock TBM in Korea, The 14th World Conference of the Associated research Centers for the Urban Underground Space (ACUUS 2014), Seoul.
- Jeong, HY., Cho, JW., Jeon, SW, Rostami, J., 2016, Performance assessment of hard rock TBM and rock boreability using punch penetration test, Rock Mechanics and Rock Engineering, Vol. 49 (4), pp. 1517-1532.
- Kahraman S, Develi K, Yas-ar E., 2004, Predicting the penetration rate of percussive blast hole drills using coarseness index and median particle size. CIM Bull, Vol 97, pp. 1083.
- Kahraman S, Yasar E., 2005, The effect of drilling depth on the penetration rate of percussive blasthole drills. In: Tadeusiewicz R, editor. Proceedings of the fourth international conference on mining techniques. Kraków: University of Science and Technology, pp. 149 - 159.
- Kim, TH., 2017, Shear characteristics of a rock discontinuity under various thermal, hydraulic and mechanical conditions, Ph.D. Thesis, Seoul National University, Korea.
- Lee, SJ, Choi, SW, 2013, Three dimensional numerical analysis on rock cutting behavior of disc cutter using particle flow code, Journal of Korean Society for Rock Mechanics, Vol. 23(1), pp. 54-65.
- Li H., Du, E., 2016, Simulation of rock fragmentation induced by a tunnel boring machine disk cutter, Advances in Mechanical Engineering, Vol. 8(6), pp. 1-11.
- Liu, SY., Du., CL., Cui, XX., 2009, Research on the cutting force a pick, Mining Science and Technology, Vol. 19, pp. 514-517.
- Lucy, LB., 1977, A numerical approach to testing the fission hypothesis, Astronomy Journal, No. 82, pp. 1013-1024.

- McFeat-Smith, I., Fowell, R.J., 1977. Correlation of rock properties and the cutting performance of tunnelling machines. In: Proceedings of a Conference on Rock Engineering, Newcastle Upon Tyne, England, pp. 581-602.
- Menezes, PL., Lovell, MR., Avdeev LV., Ill, CFH., 2014, Studies on the formation of discontinuous rock fragments during cutting operation, International Journal of Rock Mechanics & Mining Sciences, Vol. 71, pp. 131-142.
- Monahagan, JJ. and Gingold, RA., Shock simulation by the particle method of SPH, Journal of computational physics, Vol. 52, pp. 374-381 and 497-507.
- Nishimatsu, Y., 1972. The mechanics of the rock cutting. International Journal of Rock Mechanics and Mining Sciences, Vol (9), pp. 261-271.
- Ozdemir, L., 1995, No-dig Engineering, Trenchless Technology, Vol. 2(1), p. 18.
- Ozdemir, L., 1997, Mechanical Mining. Short course. March 19-21, Colorado Schools of Mines, Mining Engineering Department, Golden, Colorado.
- Ozdemir, L., Evans, R.J., Miller, R.J., Sharp, W., 1984, Rotary cutting machine: Research capabilities and trials, Tunnels and Tunnelling, April, pp. 35-37.
- Park, JY., Kang, H., Lee, JW., Jeong, MS., Kim, HJ., Cho, JW., Rostami, J., Kim, HD., 2016, Experimental study on lab-scale linear machine tests of rock cutting using a pick cutter (under review)
- Pfleider, EP., Blake, RL., 1953, Research on the cutting action of the diamond drill bit, Mining engineering, Vol. 5, pp. 187-195.
- Rojek, J., Onate, E., Labra, C., Kargl, H., 2011, Discrete element simulation of rock cutting, International Journal of Rock Mechanics & Mining Sciences, Vol. 48, pp. 996-1010.
- Rostami, J., Ozdemir, L., Neil, D.M., 1994, Performance prediction: A key issue in mechanical hard rock mining. Mining Engineering, Vol (11), pp. 1264-1267.

- Rostami, J., Gerstsch, R., Gertsch, L., 2002, Rock fragmentation by disc cutter a critical review and an update, In: Proceedings of the North American Rock Mechanics Symposium (NARMS) - Tunneling Association of Canada (TAC) Meeting, Toronto, Canada, pp. 9.
- Roxborough, F.F., Rispin, A., 1973, The mechanical cutting characteristics of the lower chalk. *Tunnels Tunnelling*, Vol. 5, pp. 45-67.
- Roxborough, F.F., Rispin, A., 1973, A laboratory investigation into the application of picks for mechanized tunnel boring in the lower chalk, *The Mining Engineer*, May, pp. 1-13.
- Roxborough, F.F., 1985, Research in mechanical excavation, progress and prospects, *Proceedings of Rapid Excavation and Tunnelling Conference*, Las Vegas, pp. 225-244.
- Roxborough, F.F., Liu, Z.C., 1995, Theoretical considerations on pick shape in rock and coal cutting, *Proc. of the 6th Underground Operator's Conference*, Kalgoorlie, WA, Australia, pp. 189-193.
- Ryu, SH., 2016, Performance assessment of a pneumatic-hammer reaming machine for rock excavation, Ph.D dissertation, Seoul National University, Korea.
- Sandvik, 2017, <http://construction.sandvik.com>
- Sanio, H.P., 1985. Prediction of the performance of disc cutters in anisotropic rock. *International Journal of Rock Mechanics and Mining Science & Geomechanics Abstracts*, Vol. 22 (3), pp. 153 - 161.
- Shao, W., Li, X., Sun, Y., Huang, H., 2017, Parametric study of rock cutting with SMART*CUT picks, *Tunnelling and Underground Space Technology*, Vol. 66, pp. 134-144.
- Stassi-d'Alia, F., 1967. Flow and fracture of materials according to a new limiting

- condition of yielding. *Meccanica*, Vol. 3, pp. 178 - 195.
- Snowdon, R.A., Ryley, M.D., Temporal, J., 1982. A study of disc cutting in selected British rocks. *International Journal of Rock Mechanics and Mining Science & Geomechanics Abstracts*, Vol 19 (3), pp. 107 - 121.
- Su, O., Akcin, N.A., 2011, Numerical simulation of rock cutting using the discrete element method, *International Journal of Rock Mechanics & Mining Sciences*, Vol. 48, pp. 434-442.
- Takaoka, S., Hayamizu, H., Misava, S., Kuriyagava, M., 1974, Mechanical fracture characteristics of rock with a cutter bit and disc cutter”, *Proc. of the Int. 3rd ISRM Congress*, September 1 - 7, Denver, pp. 1723 - 1729.
- Tham, C.Y., 2005. Reinforced concrete perforation and penetration simulation using AUTODYN-3D. *Finite Element Analysis Description*, Vol. 41, pp. 1401 - 1410.
- Tiryaki, B. and Dikmen, A., 2006, Effects of rock properties on specific cutting energy in linear cutting of sandstones by picks, *Rock Mechanics and Rock Engineering*. Vol. 39 (4), pp 89-120.
- Tiryaki, B., D. Gipps, I., Li, X., 2010, Laboratory comparison of Mini-Discs with Point attack picks, *Advanced Materials Research*, Vol. 126-128, pp. 189-194.
- Tuncdemir, H., Bilgin, N., Copur, H., Balci, C., 2008, Control of rock cutting efficiency by muck size, *International Journal of Rock Mechanics & Mining Sciences*, Vol. 45, pp. 278-288.
- Uga, Y., Sakoi, K., Sugiyama, S., Kondo, Y., Nishimura, K., Ono, H., 1986. Development of new tunnel boring machine with slurry transport system - penetration efficiency of disc cutters. *Kawasaki Heavy Industry Report 91*, 1 - 8 (in Japanese).
- Vermeer, 2017, <http://www.vermeer.com>

- Villumsen, FM., Fauerholdt, TG., 2008, Simulation of Metal cutting using smooth particle hydrodynamics, LS-DYNA Anwenderforum 2008, Vol. C(3), pp. 17-33.
- Woldemichael, DE., Abdul Rani, AM., Lemma, TA., Altaf, K., 2015, Numerical simulation of rock cutting using 2D AUTODYN, 3rd International Conference of Mechanical Engineering Research
- Xiao, N., Zhou, XP., Gong, QM., 2017, The modelling of rock breakage process by TBM rolling cutters using 3D FEM-SPH coupled method, Tunnelling and Underground Space Technology, Vol. 61, pp. 90-103.
- Yang, SQ. and Jing, HW, 2011, Strength failure and crack coalescence behavior of brittle sandstone samples containing a single fissure under uniaxial compression, International Journal of Fracture, Vol. 168(2), pp. 227-250.

초 록

다양한 암반기계굴착 기법들이 각종 토목·자원 개발 공사에서 적용되어 오고 있고, 발파굴착공법과 비교하여 가지는 안전성, 공사효율, 공사성 등의 장점 때문에 그 적용사례가 점차 증가하고 있는 추세이다. 특히 도심지 터널공사나 해저에서의 파이프/케이블라인 매설에는 기계굴착공법의 적용이 필수적이다. 암반을 굴착하는 기계 장비 중 픽 커터를 굴착 도구로 사용하는 TBM, 로드헤더, 트렌처, Auger 등은 터널링, 드릴링, 자원개발, 트렌치 공사 등에 광범위하게 활용 될 수 있다.

기계식 굴착장비는 장비의 설계 변경이 매우 어렵기 때문에, 대상 지반의 특성을 고려하여 장비를 설계하고 그 운용조건을 사전에 결정하는 것이 매우 중요하다. 기계굴착장비의 핵심설계변수로는 커터배열, 추력, 토크, 회전속도 등이 있고, 이 설계 변수들은 굴착도구인 픽 커터의 절삭조건 (압입깊이, 커터간격, 절삭각도 등)과 암반의 물성이 절삭력, 절삭효율, 장비의 안정성에 미치는 영향을 종합적으로 고려하여 최적화하여야 한다.

본 연구에서는 픽 커터의 여러 절삭조건들이 절삭성능과 절삭효율에 미치는 영향을 분석하기 위하여 소규모 선형절삭시험 장비를 제작하고 다양한 절삭조건 하에서 선형절삭시험을 수행하였다. 픽 커터의 절삭조건 (압입깊이, 커터간격, Skew angle, Attack angle)과 여러 가지 설계변수간의 상관관계를 정량적으로 분석하고 절삭효율과 장비의 안정성 측면을 모두 고려하여 최적의 절삭조건을 제안하였다.

또한 암석의 절삭과정에서 발생하는 암편의 크기와 그 분포를 체시험과 이미지 프로세싱 기법을 이용하여 정량적으로 분석하였다. 암편의 크기분포는 굴착효율과 밀접한 상관관계를 보였으며, 암편의 크기가 클수

록, 미세분진의 비율이 낮을수록 굴착효율이 높은 절삭조건인 것으로 나타났다.

픽 커터에 의한 암석의 절삭과정을 AUTODYN-3D를 이용하여 수치 해석적으로 모사하고, 굴착효율을 평가하였다. 특히 암석절삭해석에서 기존의 그리드기반의 FEM이 가지는 한계점을 극복하기 위하여 SPH기법의 적용성을 평가하고 다수의 커터에 의한 암석의 절삭과정을 모사하는 해석 모델을 제안하였다. SPH기법을 사용한 수치해석모델은 선형절삭시험결과와 비교하여 볼 때 암석의 절삭과정을 현실적으로 모사할 수 있었고, 이를 통해 SPH기법의 적용성을 확인할 수 있었다.

픽 커터를 사용한 트렌칭 커터의 설계과정을 제안하였다. 본 연구에서 얻은 선형절삭 시험결과와 수치해석 결과를 종합하여 트렌칭 커터의 설계를 수행하였고, 트렌칭 커터의 최적운용조건을 제안하였다.

본 연구의 시험결과, 수치해석기법, 설계자료들은 트렌칭 커터의 설계 및 픽 커터를 사용한 다양한 기계굴착장비의 설계에 활용될 수 있을 것으로 기대된다.

주요어: 픽 커터, 소규모 선형절삭시험, 절삭효율, 설계변수, 기계굴착 장비, SPH, 암편크기분포

학번: 2010-31017